DESIGN AND PERFORMANCE ANALYSIS OF A SINGLE-DRIVE AXIALLY-CONTROLLED MINIATURIZED BEARINGLESS MOTOR

Guilherme Cavalcante Rubio

Dissertação de Mestrado apresentada ao Programa de Pós-graduação em Engenharia Elétrica, COPPE, da Universidade Federal do Rio de Janeiro, como parte dos requisitos necessários à obtenção do título de Mestre em Engenharia Elétrica.

Orientadores: Luís Guilherme Barbosa Rolim
Akira Chiba

Rio de Janeiro
Março de 2018

DESIGN AND PERFORMANCE ANALYSIS OF A SINGLE-DRIVE AXIALLY-CONTROLLED MINIATURIZED BEARINGLESS MOTOR

Guilherme Cavalcante Rubio

DISSERTAÇÃO SUBMETIDA AO CORPO DOCENTE DO INSTITUTO ALBERTO LUIZ COIMBRA DE PÓS-GRADUAÇÃO E PESQUISA DE ENGENHARIA (COPPE) DA UNIVERSIDADE FEDERAL DO RIO DE JANEIRO COMO PARTE DOS REQUISITOS NECESSÁRIOS PARA A OBTENÇÃO DO GRAU DE MESTRE EM CIÊNCIAS EM ENGENHARIA ELÉTRICA.

Examinada por:

_____

Prof. Luís Guilherme Barbosa Rolim, Dr.-Ing.

_____

Prof. Edson Hirokazu Watanabe, D. Eng.

_____

Prof. Daniel Henrique Nogueira Dias, D.Sc.

RIO DE JANEIRO, RJ - BRASIL
MARÇO DE 2018

Rubio, Guilherme Cavalcante

Design And Performance Analysis of a Single-Drive Axially-Controlled Miniaturized Bearingless Motor/ Guilherme Cavalcante Rubio. – Rio de Janeiro: UFRJ/COPPE, 2018.

IX, 93p.: il.; 29,7 cm.

Orientadores: Luís Guilherme Barbosa Rolim

Akira Chiba

Dissertação (mestrado) – UFRJ/ COPPE/ Programa de Engenharia Elétrica, 2018.

Referências Bibliográficas: p. 91-93.

1. Análise por elementos finitos. 2. Levitação magnética. 3. Mancais magnéticos. I. Rolim, Luís Guilherme Barbosa *et al*. II. Universidade Federal do Rio de Janeiro, COPPE, Programa de Engenharia Elétrica. III. Título.

Acknowledgements

This project was developed in partnership with Chiba Laboratory of Tokyo Institute of Technology, using their technologies and resources, with financial support from the Japanese Ministry of Education, Culture, Sports, Science and Technology (MEXT).

I am grateful for this opportunity and for the shared knowledge, with hopes of strengthening the bonds between both countries, aiming towards technology development and the welfare of world population.

I would like to thank professor Akira Chiba and professor Hiroya Sugimoto for kindly sharing their experience. Their work on bearingless motors is both impressive and inspiring. I thank the colleagues from Chiba Laboratory for their comments during lab seminars and for their friendship, specially Theeraphong Srichiangsa, who gave me some hints on the JMAG software. I thank Ei Tokioka from Chiba Lab and the staff from Tokyo Institute of Technology for helping me with the procedures for enrollment and daily life on campus.

Special thanks to my advisor at UFRJ, professor Luis Guilherme Rolim, for being very understanding and one of my inspirations for following the research path. I thank professor Edson Watanabe, the former Japanese scholarship students and the staff at the Japanese embassy in Rio de Janeiro for promoting diplomatic relations and academic exchange between Japan and Brazil. I thank Márcia de Oliveira and the staff in Programa de Engenharia Elétrica for helping me with the procedures within UFRJ.

I am grateful for having studied in UFRJ and for having met so many amazing friends, professors and staff. With our collective efforts we can always go farther.

I thank my family, especially my mother Loide Cavalcante, for supporting my projects and establishing the foundation where I built my life. I thank my girlfriend, Saori Shinohara, for her continuous support.

To all the friends that I met in Brazil and in Japan, my gratitude for making life happier and for your friendship.

Resumo da Dissertação apresentada à COPPE/UFRJ como parte dos requisitos necessários para a obtenção do grau de Mestre em Ciências (M.Sc.)

DESENVOLVIMENTO DE UM MOTOR MINIATURIZADO COM SUSPENSÃO MAGNÉTICA AXIAL INTEGRADA

Guilherme Cavalcante Rubio

Março/2018

Orientadores: Luís Guilherme Barbosa Rolim
Akira Chiba
Programa: Engenharia Elétrica

Sistemas como bombas de sangue e equipamentos situados em estações espaciais ou grandes torres requerem máquinas elétricas com operação confiável e altamente duráveis. Contato mecânico entre partes estáticas e rotativas é uma das principais causas de falhas em máquinas elétricas.

A fim de eliminar completamente o contato mecânico, mancais magnéticos se tornaram uma alternativa aos tradicionais mancais mecânicos. Através do uso de ímãs permanentes e eletroímãs, tornou-se possível levitar as partes rotativas do motor, resolvendo o problema do desgaste e elevando a durabilidade, ao custo de aumentar a complexidade operacional do sistema. Neste tipo de máquina, a miniaturização se torna mais desafiadora. Estruturas para controle de posição são incluídas e um posicionamento altamente preciso é necessário. Cada fração de milímetro pode levar o rotor a tocar o estator.

Adaptando a estrutura mecânica e os parâmetros eletromagnéticos de um motor com mancal magnético integrado, foi possível otimizar a distribuição de densidade de fluxo e aumentar o torque de um motor síncrono de ímãs permanentes miniaturizado, com posição altamente estável. Esta dissertação mostra o método empregado e os passos para atingir a versão final do modelo, bem como os resultados de análise por elementos finitos.

Abstract of Dissertation presented to COPPE/UFRJ as a partial fulfillment of the requirements for the degree of Master of Science (M.Sc.)

DESIGN AND PERFORMANCE ANALYSIS OF A SINGLE-DRIVE AXIALLY-CONTROLLED MINIATURIZED BEARINGLESS MOTOR

Guilherme Cavalcante Rubio

March/2018

Advisors: Luís Guilherme Barbosa Rolim
Akira Chiba

Department: Electrical Engineering

Some systems like blood pumps and equipment positioned in space stations or high towers require electrical machines with highly reliable operation and extended durability. Mechanical contact between rotating and static parts are a major cause of failure in electrical machines.

To eliminate mechanical contact completely, magnetic bearings rose as an alternative to the usual mechanical ones. Through use of permanent magnets and electromagnets, it became possible to levitate the rotating parts, addressing the wearing and durability problems, at the expense of an increase in complexity of operation. In this kind of machine, miniaturization becomes more challenging. Position control structures are included and highly stable positioning is required. Each fraction of millimeter can lead the rotor shaft to contact with the stator.

By adapting the mechanical structure and electromagnetic parameters of a bearingless motor, it was possible to optimize flux density distribution and increase torque in a miniaturized permanent magnet synchronous motor, while keeping position stability high. This dissertation presents the method employed and the intermediate steps taken towards the final version, as well the finite element analysis results.

Summary

1.Introduction

1.1. Background and objectives

Rotating electrical machines play a crucial role in the development of human society. Be it for transportation, temperature control, construction activities, domestic appliances and even life support systems, people are always surrounded by those machines. Some of those applications require uninterrupted and reliable operation.

The friction between bearings and rotor shaft causes deterioration of the bearing material, releasing residues and contaminating fluids pumped by the motor. This should be avoided as much as possible in high purity chemical processes and blood pumps. Wearing of rotating parts is also a reason for constant preventive maintenance[1], especially in high speed applications. Sometimes maintenance is dangerous, costly or even impossible, like in space stations, high towers or underwater facilities. Highly durable bearings become a must in these applications. To increase reliability and reduce mechanical losses due to friction, magnetic bearings can be employed instead of regular mechanical bearings, eliminating mechanical contact during operation.

A magnetic bearing consists of a system that keeps the rotor in the intended position by means of magnetic suspension. By manipulating magnetic field intensity in opposite sides of the rotor structure, it is possible to create a differential force, capable of compensating disturbances and stabilizing the rotor position in all axes.

Since there are no mechanical bearings constraining the rotor displacement, it gains five degrees of freedom (5DOF). By five degrees of freedom it means that movements along the x and y radial positions, the z axial position and the tilting around x and y axes are possible. All degrees of freedom can be actively controlled by using electromagnets, but each one adds an extra layer of complexity to the model and to the control strategy.

Along with the benefits of magnetic bearings comes the design complexity of fabricating machines that contain embedded suspension systems. Along with torque control, the motor must also operate in a stable position. This requires that position sensors, magnets for passive stabilization and electromagnets for active stabilization must be included in the design.

While the employment of permanent magnets can put constraints on some degrees of freedom, according to what is known as a consequence of Earnshaw's theorem[2], it

is not possible to stabilize all DOF by static means, using permanent magnets. Even though a complete passive stabilization is not feasible without employing diamagnetic materials, like superconductors, it is possible to simplify the suspension system by passively stabilizing some axes using permanent magnets, reducing the number of controlled variables.

Many developers took different approaches for controlling 5DOF. The blood pump machine designed by OSA et al.[3],[4] has an axial gap motor with two stators for providing torque, radial, axial and tilting control with enhanced vibration control. The model proposed by KURITA et al.[5] consists of a self-bearing motor on the radial plane with an outer layer of coils designed to control axial position and rotor tilting. It is a complicated model that does not rely on passive stabilization.

Simpler solutions were adopted by ASAMA et al.[6], OOSHIMA and TAKEUCHI[7], and SCHUCK[8], that utilize active control only on radial position, while passively stabilizing the axial direction.

The work published by KUROKI et al.[9] shows the experimental results for a magnetic bearing that has active control only on axial position while radial position is passively stabilized. This strategy is similar to the one employed in other publications[10]-[15], with the difference that the later ones are single-drive motors, that integrate the magnetic axial suspension control system with the motor drive, allowing the use of just one inverter for controlling both rotor torque and shaft positioning.

The outer rotor permanent magnet machine presented by YAMADA et al.[16] has separate suspension coils for radial position stabilization on axes x and y, while axial position is stabilized by permanent magnets. Another external rotor machine was proposed by TAKEMOTO et al.[17], in which four radial axes were actively controlled with separate suspension and torque coils. An outer rotor type motor was also designed by REICHERT et al.[18],[19],[20] for bioreactor tanks. It is a permanent magnet machine in which axial positioning and tilting around x and y axes are passively stabilized, while the radial position is actively controlled.

This work focuses on designing a miniaturized permanent magnet three-phase single-drive bearingless inner rotor type motor with passive radial (x-y) stabilization and active 1DOF control of axial (z) position. There are no restrictions for the back electromotive force, except that it should be low enough to operate with usual DC source levels for inverters. The proposed motor is targeted for general applications that require

miniaturized design with reliable operation and high durability, such as fans, blood pumps and small generators for mobile applications. The first test application will be as a cooling fan with radial air gap. A machine smaller than a thumb is being targeted, with diameter and height at the order of a few centimeters. This motor must have good torque density and must present small oscillations in the passively controlled radial direction. SUGIMOTO et al.[11] proposed the concept of centering index for evaluating the oscillation of passively stabilized position and gathered information about other 1DOF axially suspended motors, like shown in Figure 1.1. We are pursuing models with high torque density and centering index, with at least 0.3Nm/ℓ torque density and centering index higher than 30.

The reduced size of the model implies the need for very precise fabrication and small oscillations of shaft positioning. The present document details the process of designing the target machine. It consists of dimensioning, modelling, Finite Element Analysis (FEA), performance evaluation and parameter optimization of the proposed design.

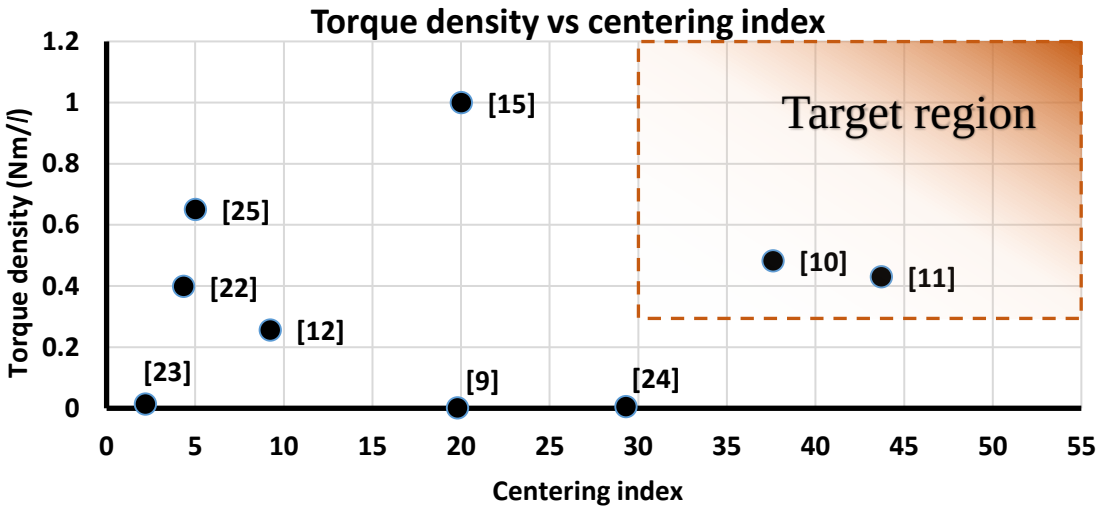

Figure 1.1 Torque density vs centering index for 1DOF axially controlled motors [11]

1.2. Document structure

In chapter 2 the base model used for creating this machine is presented along with its levitation principle and brief explanations of concepts used during the design process, such as radial stiffness, tilting torques, critical frequencies and force-current factor.

Chapter 3 describes the changes made to the model, explaining why they were adopted, while reviewing some of the intermediate versions before achieving the final model.

Chapter 4 describes the design process of the passive radial magnetic bearings. Those bearings affect greatly the motor performance. Three proposals are analyzed in this chapter.

Chapter 5 describes the performance of the final version already combined with the passive bearings. One of the bearing models is chosen as the best solution for this application. Changes made to the model are summarized at the end of the chapter.

Chapter 6 makes closing comments about the achieved results and discuss possible future enhancements that can be evaluated after testing the first experimental prototype.

2.Base model and bearingless motor design concepts

This chapter presents the structure and operation principles of a single-drive axially positioned bearingless motor, along with the parameters that should be considered for the design of a new prototype.

2.1. Base model overview

Figure 2.1 shows a model for the inner rotor type single-drive bearingless machine presented by SUGIMOTO et al.[14].

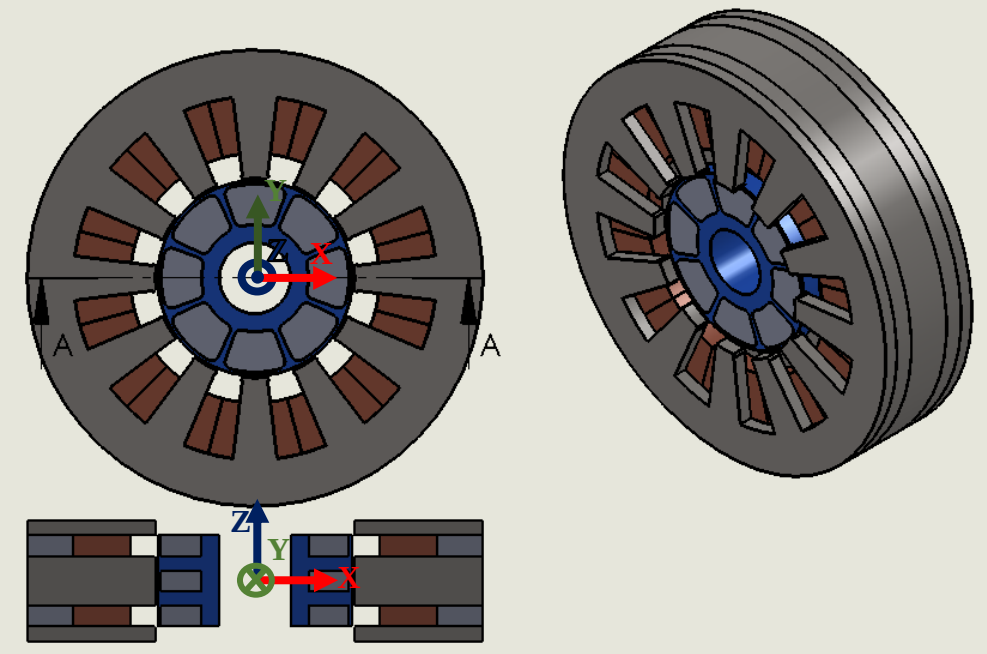

Figure 2.1 Model overview of the traditional topology on [14]

2.2. Stator details

The stator is composed by five layers, as seen in Figure 2.2. The outer and central layers are composed of 35H360, laminated steel. The intermediate layers are S45C, carbon steel for structure. There are 12 stator teeth with angular shape and small corners at the tip to give the coils mechanical support, like shown in Figure 2.3.

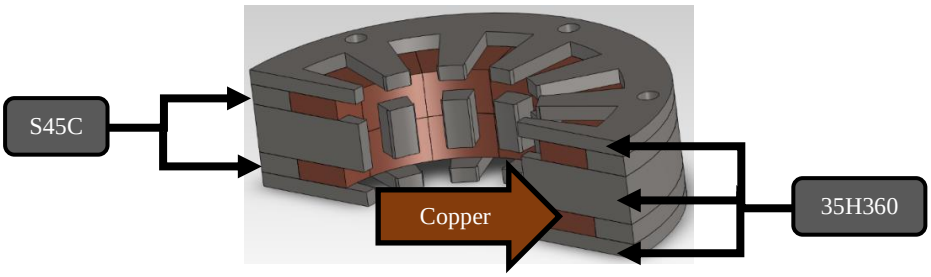

Figure 2.2 Stator cut

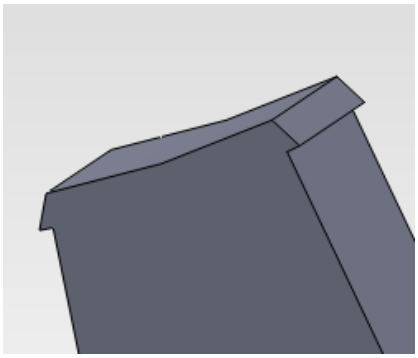

Figure 2.3 Stator tooth detail

2.3. Rotor details

The rotor is composed by three layers of eight poles segmented permanent magnets held by a non-magnetic case. The magnetic material is Neodymiun Iron Boron (NdFeB), N40SH. The central layer is used for torque generation while the outer layers are responsible for magnetic suspension forces. The outer layers have opposite polarizing directions, like shown in Figure 2.4, implying self-cancelling generated torques. This condition makes the central part the only torque contributing one.

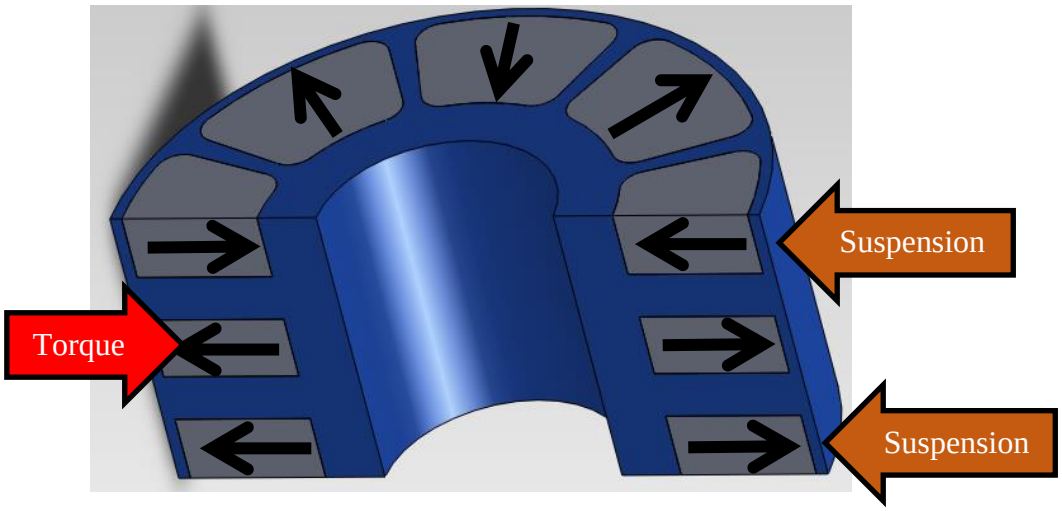

Figure 2.4 Rotor cut and PM polarization

2.4. Slot fill factor

Slot fill factor, s_{ff}, is defined as the ratio of the slot area occupied by conductors to the area available inside the slot, as given by:

$$s_{ff} = \frac{n\,\pi\,(d/2)^2}{s_a},$$

where n is the number of turns per coil, s_a is the slot area and d is the conductor diameter.

A value of $s_{ff} < 40\%$ is desired for making the coil assembling easier. During the design process of a new prototype, this should be kept in mind when increasing the stator core's thickness or the number of conductors per coil. Figure 2.5 and Figure 2.6 show a vertical cut on XZ plane and an horizontal cut in XY plane. The 40% s_{ff} limitation must be observed for both sections.

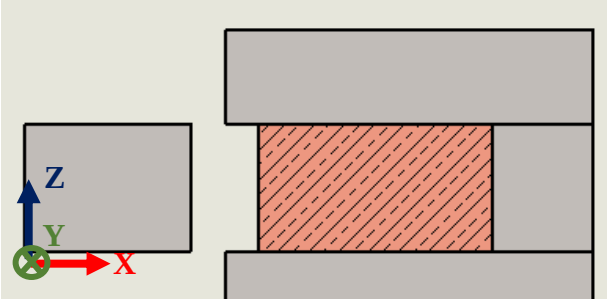

Figure 2.5 Vertical coil section (XZ cut)

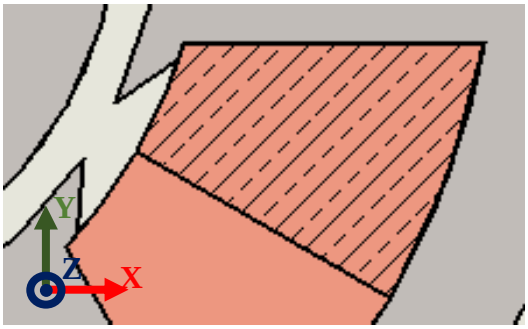

Figure 2.6 Horizontal coil section (XY cut)

2.5. Suspension force principles

Like said in chapter 1, there are five degrees of freedom for the rotor position on a magnetic bearing or bearingless machine: *x* and *y* position in the radial plane, *z* axial position and rotation along the *x* and *y* axes. In this work, radial position and rotor tilting along *x* and *y* axes are passively stabilized by permanent magnets while the axial

position is actively controlled. A single inverter is used for both axial stabilization and motor driving. Therefore, this is called a single-drive bearingless motor.

Figure 2.7 shows the magnetic flux paths inside a motor section that intersects the rotational axis (*z*-axis). Suppose a pair of dynamic coordinates *dq* with *d*-axis aligned with the rotor pole central position. Red lines show the field induced by the stator currents in *d*-axis, while the dotted yellow lines show the flux path of the rotor permanent magnets, also called bias flux. If the *d*-axis current is positive, the induced flux causes a flux strengthening in the upper side of the air gap and a flux weakening in the lower side of the air gap. This difference in flux magnitude generates a force along the positive direction of the *z*-axis. In case the *d*-axis current is negative, flux weakening occurs in the upper side of the air gap and flux strengthening occurs in the lower side, generating a force along the negative direction of the *z*-axis.

In summary, a positive *d*-axis stator current induces a positive *z* force, while a negative current induces a negative *z* force. By controlling the *d*-axis current it is possible to adjust the axial position of the rotor shaft, while the torque magnitude is controlled by the *q*-axis current, normal to the *d*-axis and to the rotor pole reference.

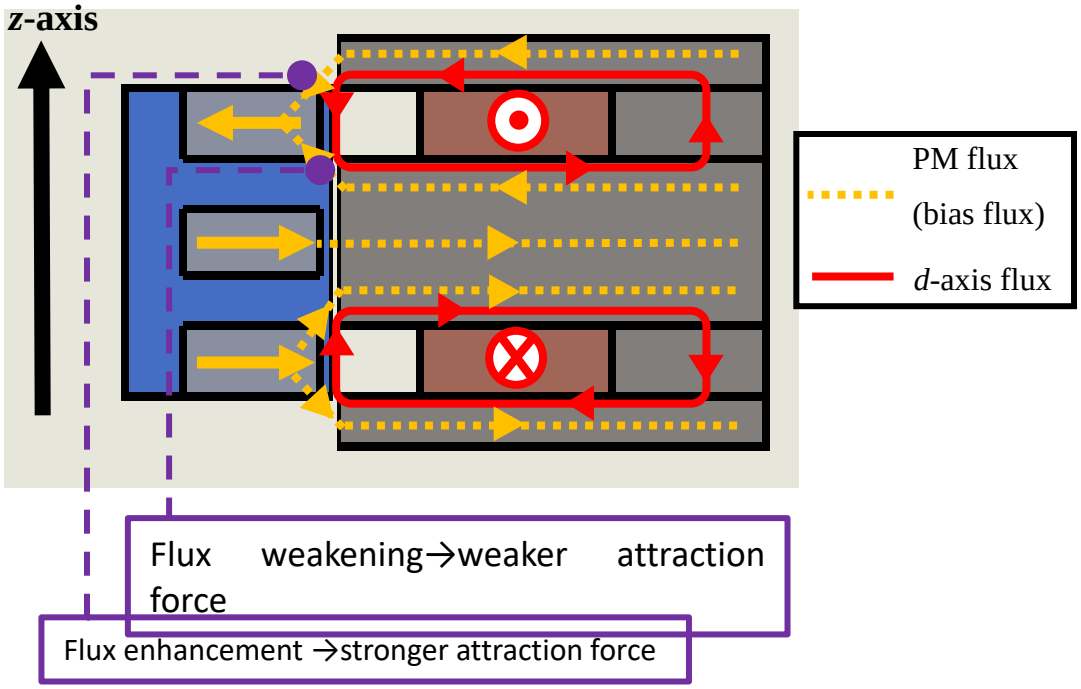

Figure 2.7 Magnetic flux path

The radial attraction forces between the rotor permanent magnets and the stator core are unstable. Moving the rotor axis away from the central position causes an increase in radial force magnitude. To compensate those forces, a passive method is

applied. Permanent magnet bearings are attached to the rotor shaft and to the stator as shown in Figure 2.8.

The passive bearings are attached in two points along the shaft axis to prevent rotor tilting. They are comprised of four permanent magnet rings, polarized as shown in Figure 2.8. The magnetic polarization creates repulsive forces between the inner and the outer rings like shown in Figure 2.9. Similar to the radial forces between stator and rotor, the closer the rings are to each other, the stronger the forces become. But in opposition to the rotor radial forces, the inner rings of the passive bearings are subject to stable forces that push them towards the center position. By choosing appropriately dimensioned bearings, it is possible to compensate the rotor's unstable radial forces.

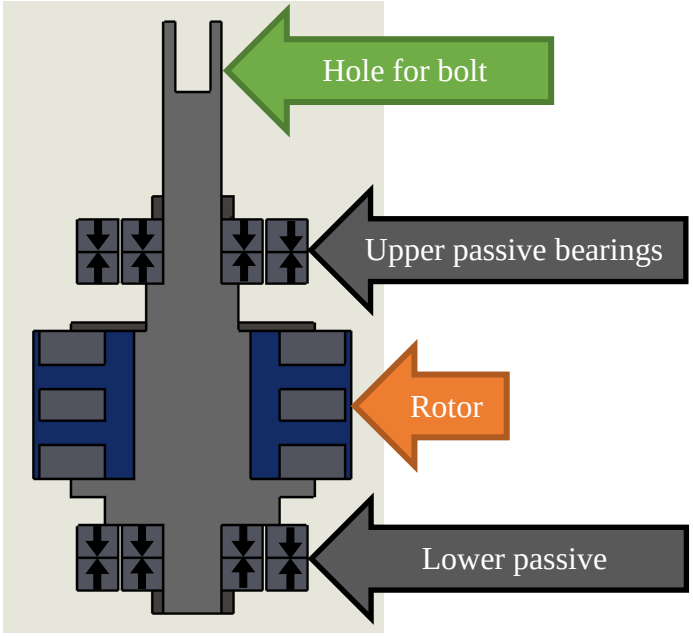

Figure 2.8 Rotor shaft cut

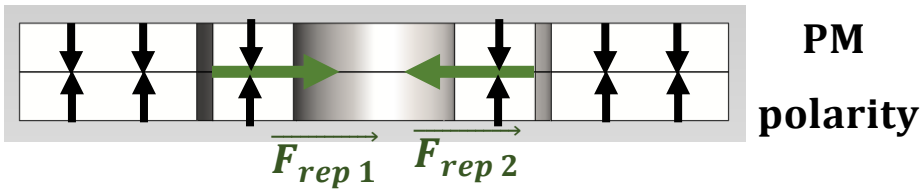

Figure 2.9 Repulsive forces on a radial passive magnetic bearing

2.6. Radial forces and passive stabilization

To analyze the stability of the rotor radial position, we define $K_r = \frac{\partial F_r}{\partial r}$, where K_r is the radial stiffness and $\frac{\partial F_r}{\partial r}$ is the derivative of the radial force in terms of radial displacement r. If K_r is negative, then F_r is a restorative force and the radial position is stable. If K_r is positive, then the radial position is unstable.

For small displacements, the radial force is a linear function of r and $\frac{\partial F_r}{\partial r}$ is a constant. In this linear region it is possible to separate K_r in other two linear components: K_{rr}, the rotor's radial stiffness and K_{rb}, the magnetic bearing's radial stiffness. Resultant radial stiffness is given by:

$$K_r = K_{rr} + K_{rb}$$

Even though a negative K_r ensures that the radial position is stable, it is also necessary to analyze if the stiffness can damp position oscillations. More negative K_r imply more stable radial positioning. Deciding how steep the F_r curve should be depends on the weight of the rotating parts, since for different mass, different oscillation occurs.

The centering index C_i is a concept introduced by SUGIMOTO et al.[8] as an attempt of finding an easier parameter to evaluate radial stabilization, even among motors with different rotor weights. It is defined by:

$$C_i = \left|\frac{g}{w/K_r}\right| = \left|\frac{gK_r}{w}\right|,$$

where g is the air gap size in mm, w is the rotor weight in N and K_r is the rotor resultant radial stiffness in N/mm. Estimated centering index is what determines if an estimated radial stiffness is acceptable or not.

2.7. Tilting stiffness

The tilting stiffness is a concept similar to the radial stiffness. It relates the torque around *x* or *y* axis to an angular displacement around the same axis. It is given by:

$$K_\theta = \frac{\partial T_\theta}{\partial \theta},$$

where K_θ is the tilting stiffness, and $\frac{\partial T_\theta}{\partial \theta}$ is the derivative of tilting torque at an angle θ between the rotor axis and the *z*-axis.

Usually it is not established a design specification for K_θ, but it must have a negative value to assure stability.

2.8. Critical frequency

The critical frequency or critical speed is the rotor mechanical speed value at which oscillations achieve the maximum value. It depends on both the stiffness coefficient and mass, so the rotor must be designed keeping this in mind. The rated speed must be smaller or higher, but never too close to critical speed values.

The mechanical frequency f_r in Hz where radial oscillations are maximum is given by:

$$f_r = \frac{1}{2\pi}\sqrt{\frac{|K_r|}{m}},$$

Where K_r is the resultant radial stiffness in N/m and m is the rotor mass in kg.

There is also a critical speed value where tilting oscillation is maximum. The tilting critical mechanical frequency f_θ in Hz is given by

$$f_\theta = \frac{1}{2\pi}\sqrt{\frac{|K_\theta|}{J}},$$

where K_θ is the tilting stiffness in Nm/rad and J is the rotor inertia in kg m².

2.9. Unstable axial forces and active stabilization

Passive radial stabilization comes with a cost. Adding radial passive bearings increase the destabilizing forces acting on the rotor axial direction. In the neutral position those forces are null, but a displacement in the axial direction generates repulsive force components that try to push farther the magnetic rings. We define the passive bearing axial stiffness as:

$$K_{zb} = \frac{\partial F_z}{\partial z},$$

where $\frac{\partial F_z}{\partial z}$ is the variation of axial forces due to a displacement of the permanent magnet along the *z*-axis. For small displacements the axial force is also a first-degree function, so K_{zp} is a constant. From FEA it is possible to see that an increase in K_{rp} implies an even bigger increase in K_{zp}. To stabilize the axial positioning, an active method based on the principle described in 2.5 is applied.

The differential force generated by flux enhancement has a limitation. Ferromagnetic materials do not allow the flux density to rise above the saturation point, implying also a ceiling for both torque and suspension forces. There are also restrictions on the number of coils due to the limited slot area available and the conductor's current capacity. When choosing a passive magnetic bearing for radial positioning, it is necessary to keep in mind the increase of unstable axial forces. The axial force needed to lift the rotor from the touchdown position must be achievable considering saturation and current limitations. The ratio from suspension force to i_d current component is known as force-current factor. A higher factor implies a more efficient position control with smaller currents and less saturation risk.

3.Earlier motor versions and design process

This chapter describes the design process and results of Finite Element Analysis for the inner rotor type model designed after the base model[14]. The design progress is shown along the intermediate versions that came before the accepted model. The software JMAG from the JSOL Corporation was used for FEA.

The new model is intended to be used on highly reliable applications for equipment positioned in spots with high cost maintenance and limited space. The machine is supposed to fit in small frames with diameters smaller than a thumb, so we use the dimensions of OSA et al.[3] as a reference. Since this is a motor with 1DOF control and radial gap, the axial length can be smaller than the one achieved by the reference[3]. Stack length is set to 17mm, including the passive radial bearings, and target outer diameter is set to 21mm. Mechanical speed is set to 18000rpm. Slot fill factor should be smaller than 40% to have enough space to accommodate the windings. Considering those restrictions, we try to raise the torque density as much as possible while also keeping a good centering index value, according to the reference data gathered by SUGIMOTO et al.[11].

The way in that the element mesh is generated greatly affects the analysis results. A mesh with a small number of elements will present a lack of details and probably deviate considerably from actual experimental results. On the other hand, meshes that have an exaggerated number of elements for calculation will raise exponentially the amount of time elapsed on simulations. Bearingless motors require 3D analysis for accurate description of forces and torques in all axes. Therefore, the number of elements is way higher than that of 2D simulations.

Careful selection of the method for mesh generation is also critical for obtaining accurate results. Since the 3D model is a rotating body, the analysis mesh needs to be adapted at each step. The mesh can either be regenerated from scratch or a sliding mesh can be created. This sliding mesh creates a volume that moves along the motion condition set for simulation. This volume is created as a cylinder rotating in the air gap region, so models that have static parts aligned with the air gap along the axial direction cannot be simulated.

3.1. First version

The simulation model of the first version is shown in Figure 3.1. The number of stator teeth was reduced from twelve to six and the number of rotor poles from eight to four. Stator axial length was set to 17mm, still not considering the radial bearings, and outer diameter to 21mm. The form factor became very different from the base model, that had a disc shape. At first the slot fill factor was not taken into consideration.

As a first try, the number of turns per coil was set to 39 and coil resistance as 0.55Ω. Phases are distributed like shown in Figure 3.2, with a phase sequence UVW. The U coil magnetic flux is aligned with the *y*-axis. Phase RMS current is set to1.57A, resulting in a current density per conductor of 12.5A/mm² for conductors with 0.04mm diameter.

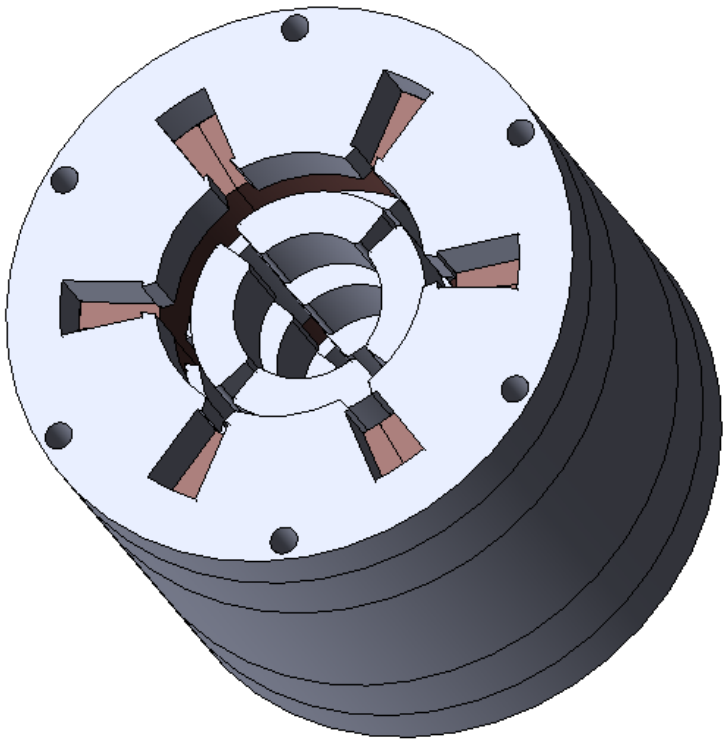

Figure 3.1 First version of the inner rotor type motor

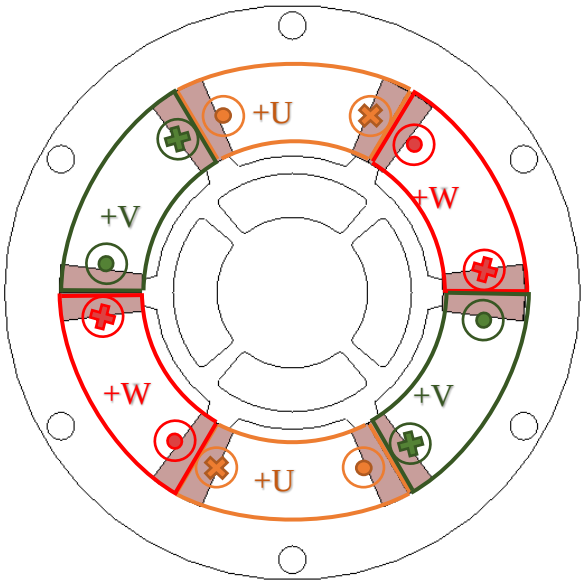

Figure 3.2 Phase distribution

Figure 3.3 shows the torque calculation results for the simulation along an electrical cycle (1.67ms). Calculated average torque is 4.32mNm. The actual torque density cannot be calculated for this model because radial bearings were still no included in the design. The ratio of the average torque to the stator volume, without bearings, is equal to 0.73Nm/ℓ.

Slot areas on this model are too small compared to the stator teeth. Slot fill factor was not considered when choosing the number of turns per tooth. The current density 12.5A/mm² may be harmful to the conductor's isolation if proper heat dispersion is not provided to the coils. Densities below 12A/mm² are desirable for air-cooled bearingless motors and 8A/mm² for non-cooled systems.

Figure 3.4 shows the generated mesh for the torque analysis, 127990 elements were generated. Maximum size of elements was set to 0.5mm on all parts and 0.3mm on stator and rotor teeth faces.

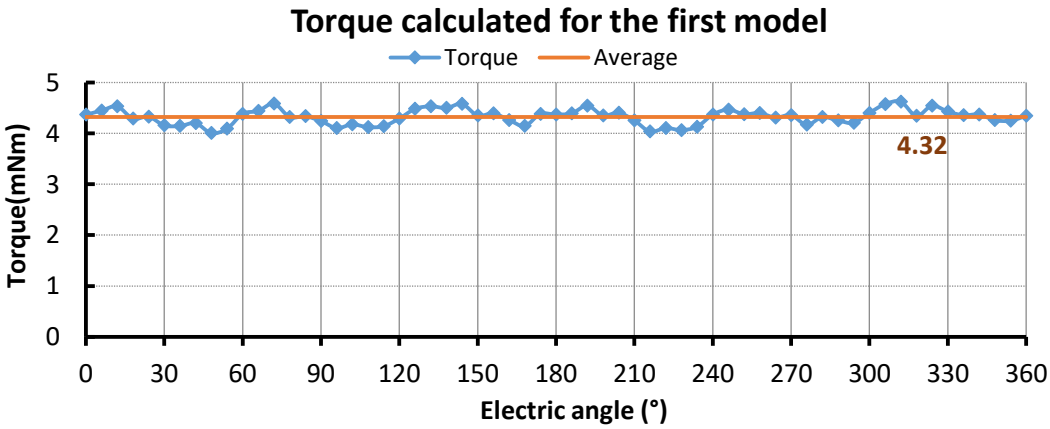

Figure 3.3 Torque result for the first version of the motor

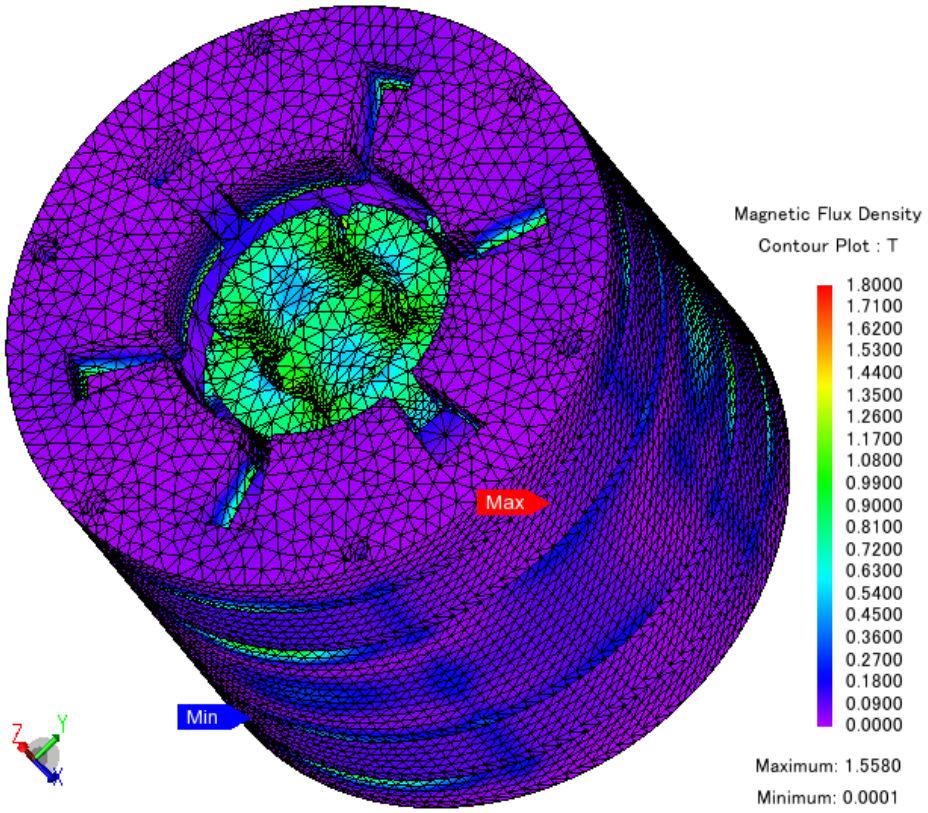

Figure 3.4 Flux density distribution and generated mesh

Figure 3.5 shows the flux density distribution in the horizontal cut. No saturation is observed.

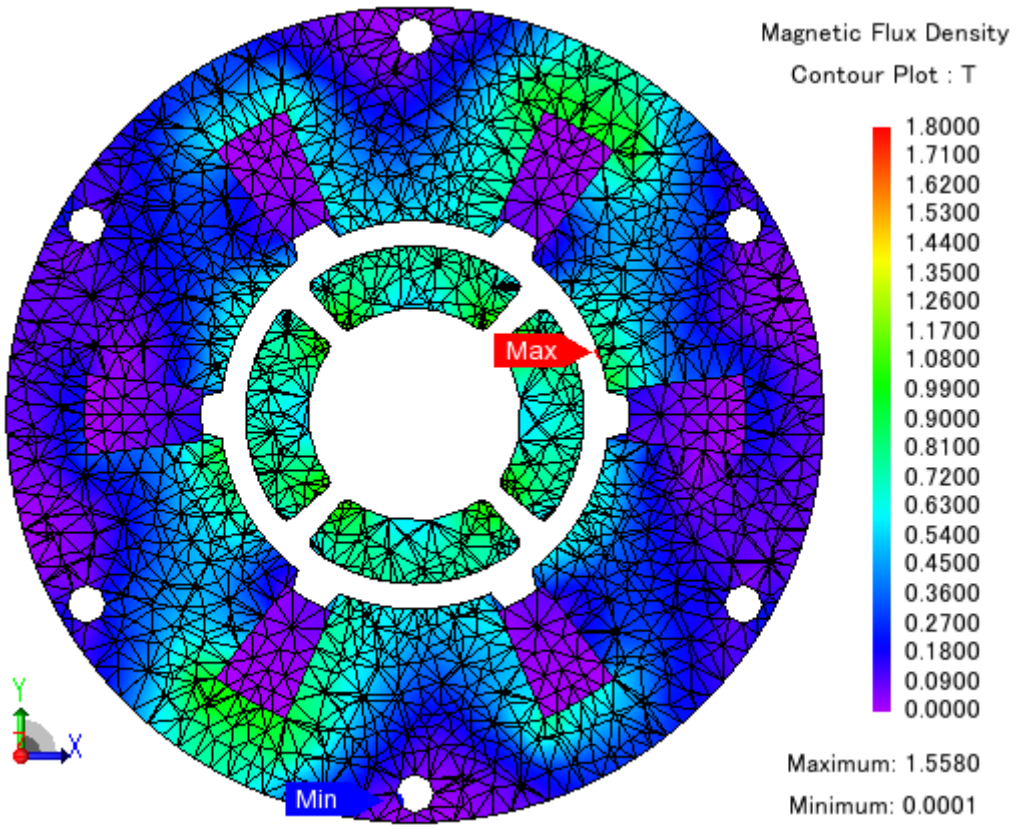

Figure 3.5 Flux density distribution at the horizontal cut in xy plane

3.2. Second version

The model was edited, now taking into consideration the slot fill factor. Due to the need for more space to accommodate the coils, the stator poles became thinner. To simplify the structure and numeric calculations, the holes for bolt fixation were removed. Being small cylindrical surfaces, they were raising the complexity of the element mesh generation. Figure 3.6 shows the 3D model used for the second version.

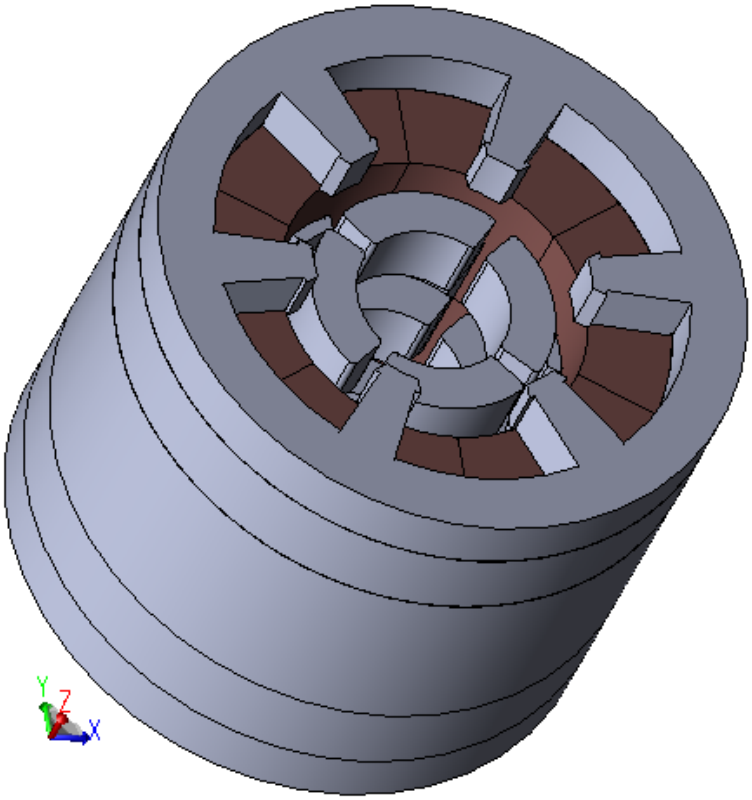

Figure 3.6 Second version of inner rotor type

Now the available area was taken into consideration. The number of turns per tooth was chosen to keep the slot fill factor below 40%. In this version, it was dropped to 26, resulting in a slot fill factor of 38.76% for the 8.43mm² slot area shown in Figure 3.7. The poles with U phase coils were now aligned with the *x*-axis, so the phase distribution becomes like what is shown in Figure 3.8.

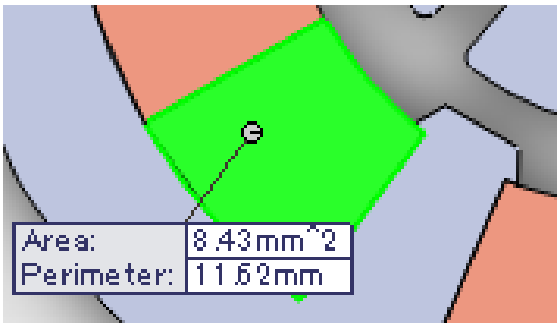

Figure 3.7 Horizontal slot area

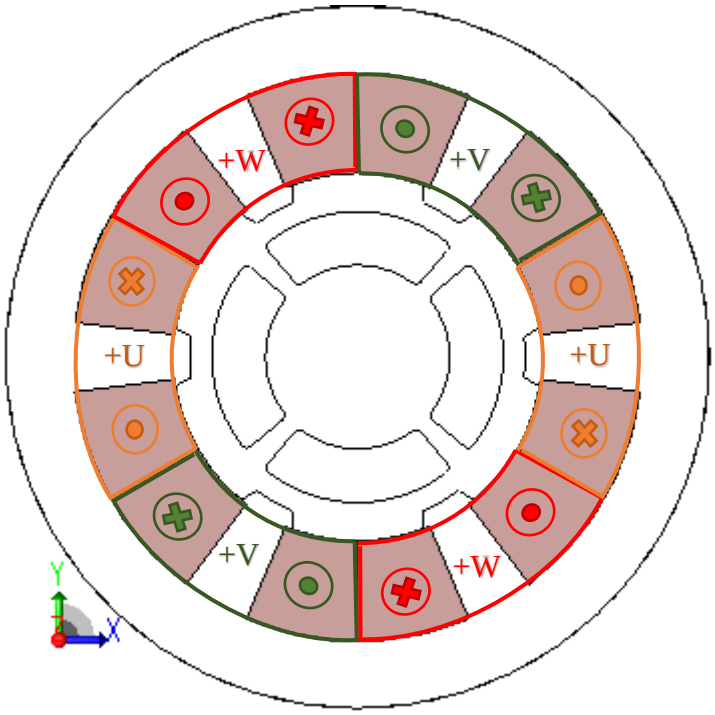

Figure 3.8 Phase distribution for the second version

This time, the element size constraints were changed. Face elements size was kept as 0.3mm, while the general parts element size was raised to 1mm, to reduce the time spent on calculations. Mesh grid is shown in Figure 3.9.

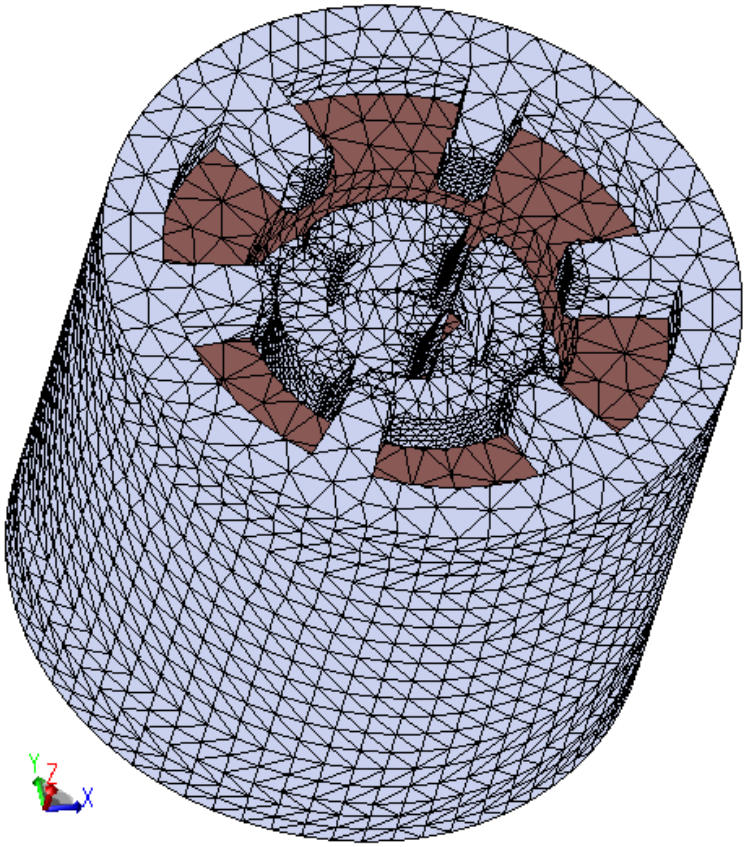

Figure 3.9 Elements mesh for the second version

Figure 3.10 and Figure 3.11 show flux density distribution for torque calculation with the same current as version 1, 1.57A RMS.

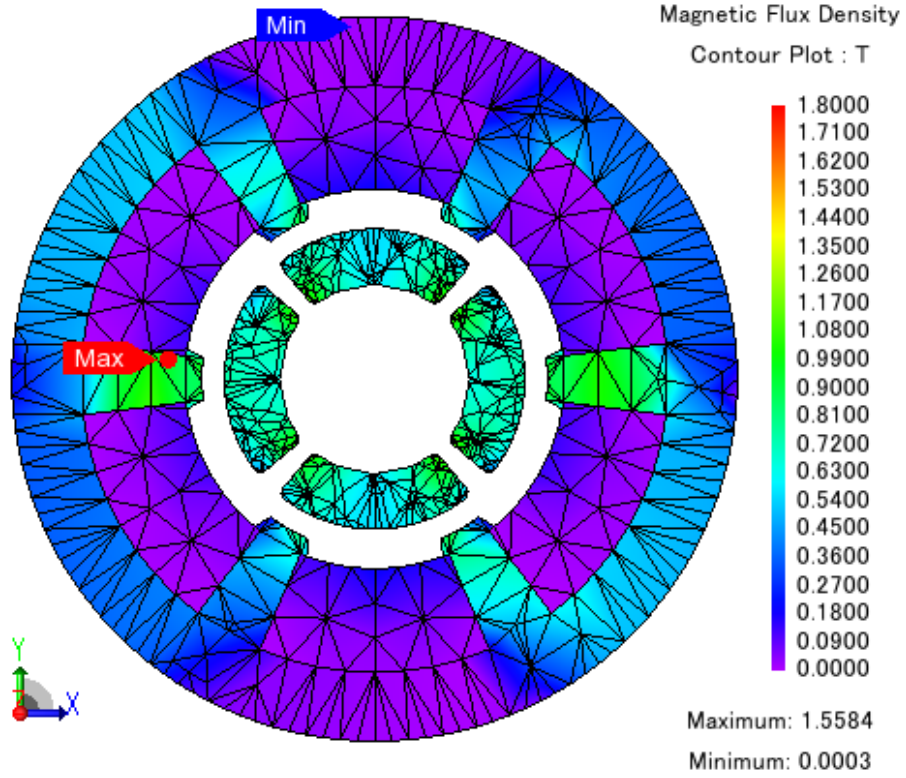

Figure 3.10 Flux density distribution on xy cross-section

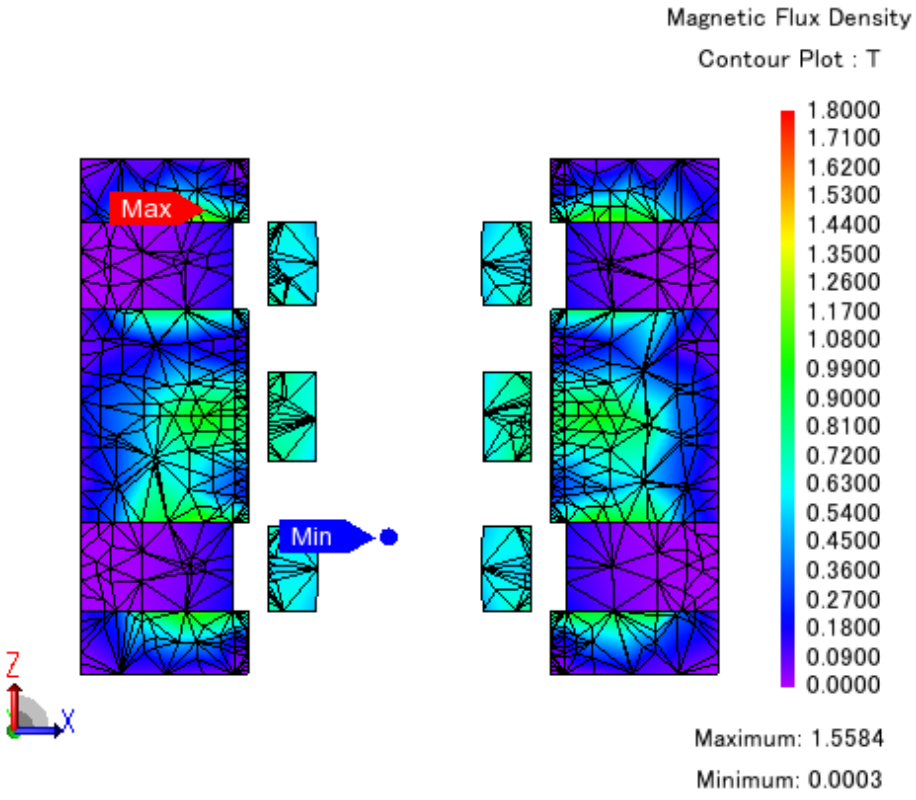

Figure 3.11 Flux density distribution on xz cross-section

Figure 3.12 shows the calculated torque for the second model. The average value obtained was 2.17mNm. It is important to notice that the plotted results have a lot of random oscillation. Suspecting that this may be noise originated from the calculation methods, a second simulation was done.

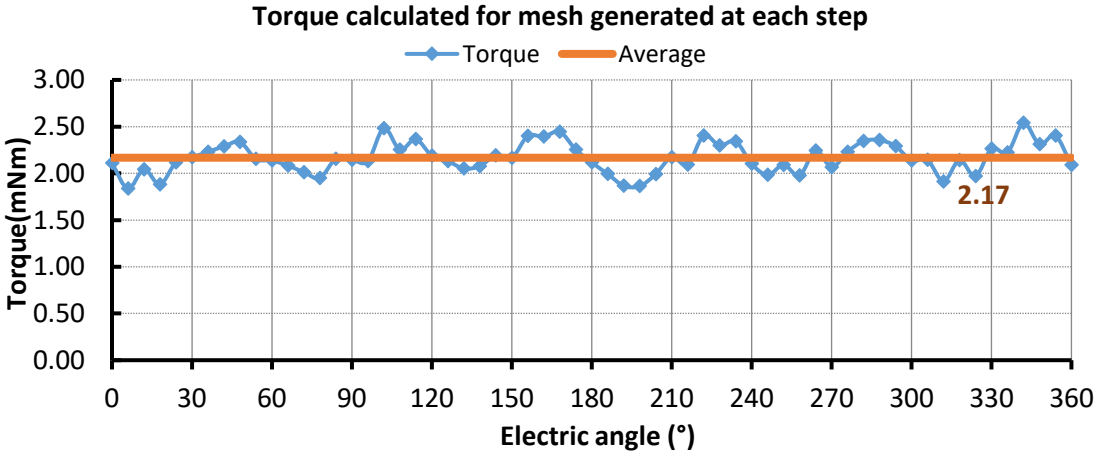

Figure 3.12 Torque calculated for the second version generating a new mesh for each step

The graph from Figure 3.13 shows results for the same simulation from Figure 3.12 after changing the mesh generation method. In the previous calculations, a new mesh was calculated at each step of the simulation, what may have caused the observed random behavior. It was changed to a slide mesh generation method, resulting in a periodic signal. The average torque calculated became 2.19mNm.

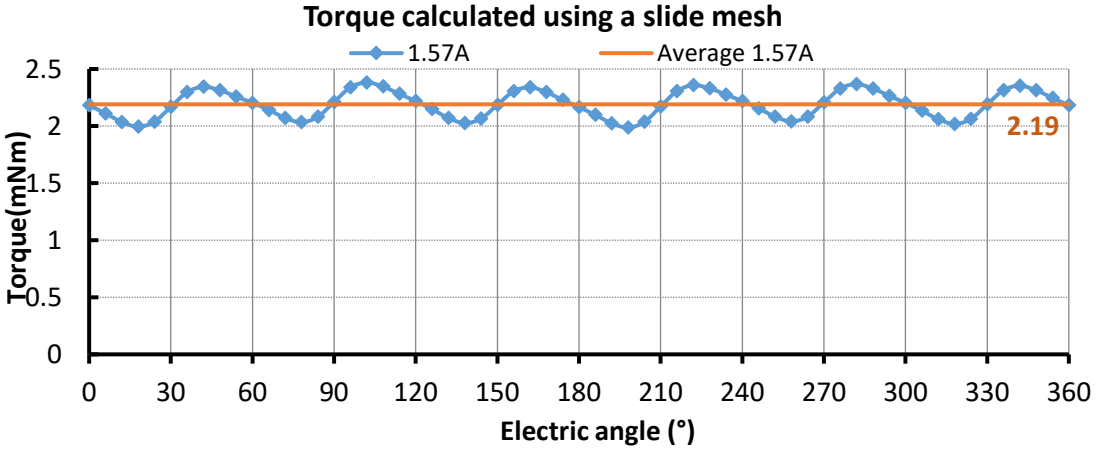

Figure 3.13 Torque calculated for the second version using a slide mesh

The slide mesh method has an advantage over the mesh generated at each step. It creates a detailed mesh for the air gap that follows the motion set in the simulation. The mesh shown in Figure 3.14 was generated with 5 radial divisions and 192 circumferential divisions. In addition to the better results, it also shows data calculated

in the air gap region. When the “generate mesh at each step” method is chosen, air gap information is not shown if the simulation has any kind of motion.

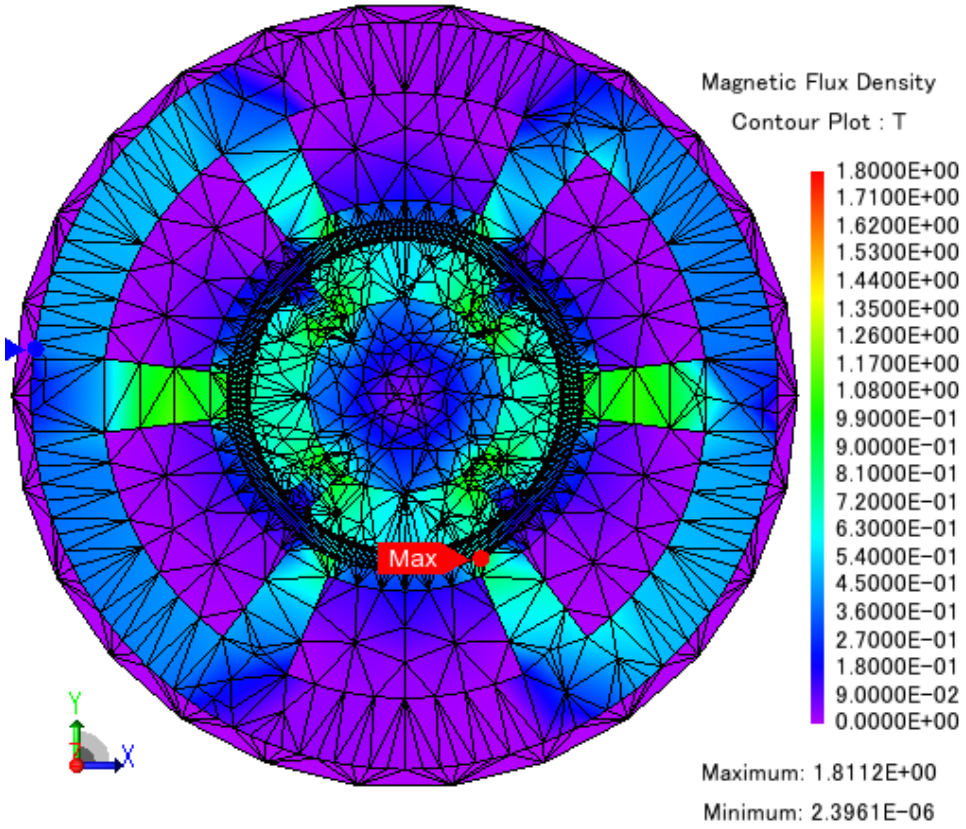

Figure 3.14 Flux density distribution for the second version with slide mesh generation

The 1.57A current set in the simulation must be reduced, if possible. The 0.4mm diameter conductors used in the coils can operate with a maximum current of 1A RMS to guarantee current density below 8A/mm² without any kind of cooling system. By exceeding this value, the conductor isolation is endangered, and a cooling system must be applied.

Figure 3.15 shows a comparison between the torque calculated for the 1.57A current set in the first tentative and the torque for the desirable 1A current. For 1A RMS, current density becomes 7.97A/mm² and the average torque drops to 1.39mNm. Torque density drops to 0.24Nm/ℓ.

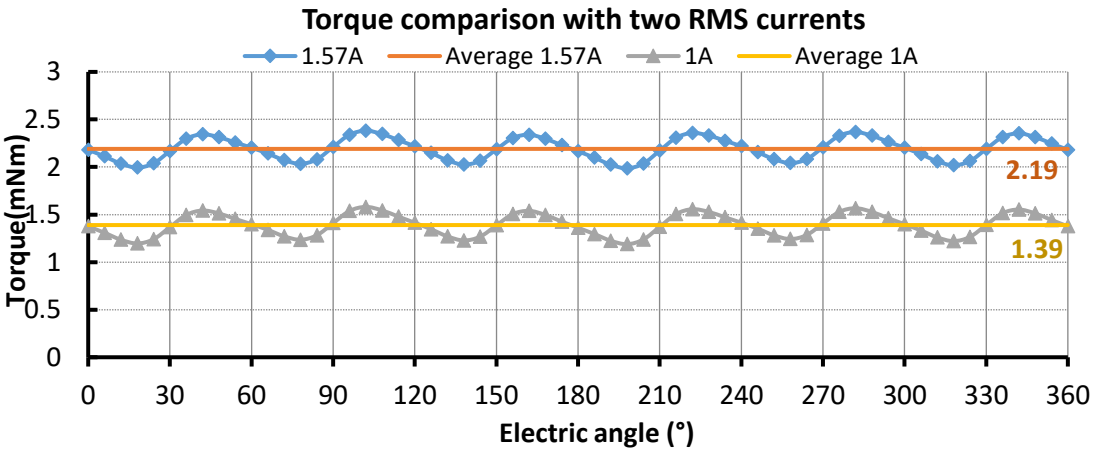

Figure 3.15 Calculated torque comparison between 1.57A RMS and 1A RMS

A RMS current value above 1A is not desirable, but the 0.20Nm/ℓ torque density on 1A current condition was too low. This model had an axial length of 17mm, a little smaller than the stack length specification. Considering that passive magnetic bearings must also fit inside this height and that torque density needs improvement, on the next steps, axial length is reduced while trying to raise the average torque.

3.3. Third version

The third version of the inner rotor type motor is almost identical to the second one. The thickness of the rotor permanent magnets was increased with the objective of raising the average torque level. The third 3D model can be seen in Figure 3.16.

Figure 3.17 shows the torque calculated for the third version and its average value, compared to the previous version's torque for a 1A RMS current. The average torque for the new model was 1.71mNm.

According to Figure 3.18, the flux density distribution is not uniform along the yoke and the stator teeth. The flux density in the yoke is lower than the flux density in the stator teeth, indicating that the yoke can be reduced without risking a saturation of the core. Figure 3.19 shows that along the *z* dimension, there are also low density spots. Reducing the axial length while keeping everything else constant may not result in saturation risk for rated operation.

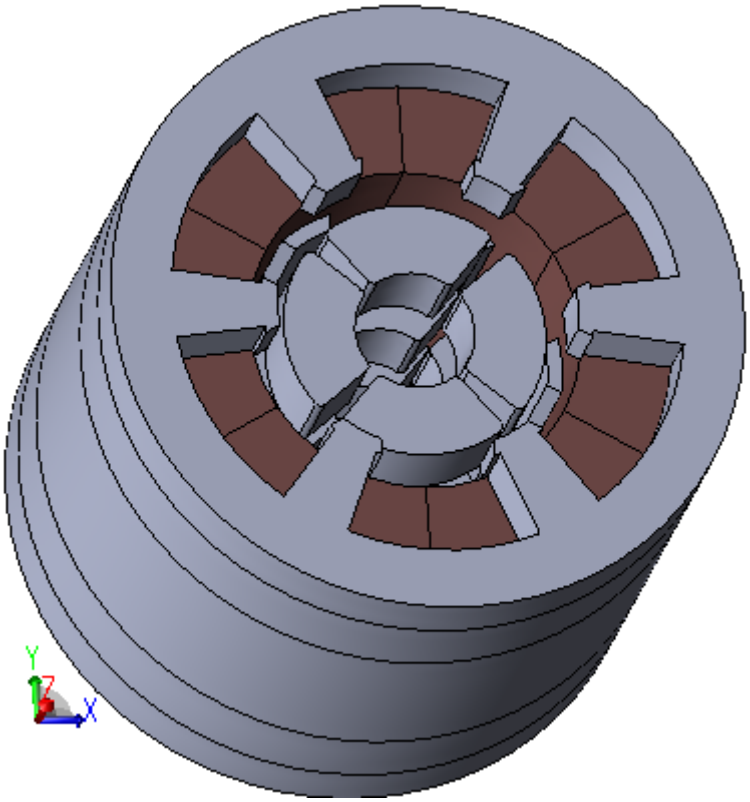

Figure 3.16 3D model of the third version

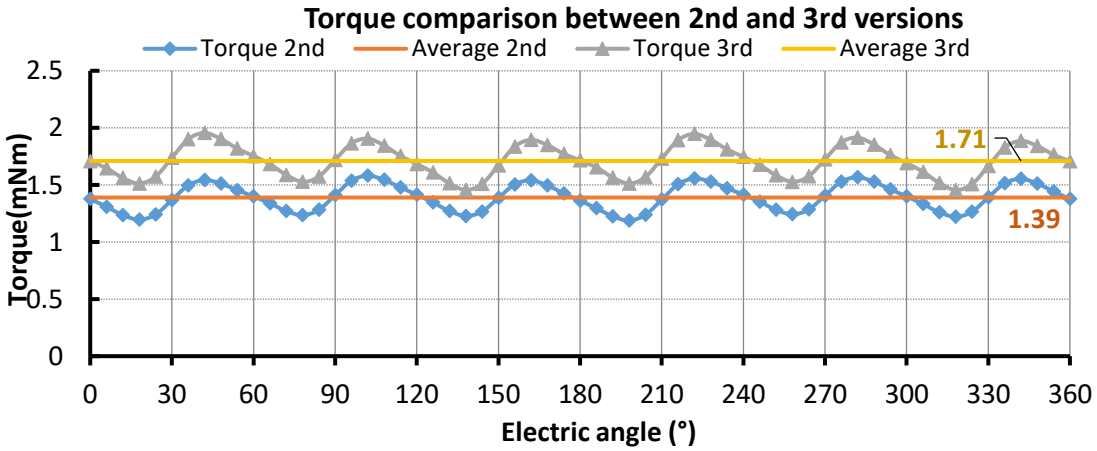

Figure 3.17 Torque calculation for the third version

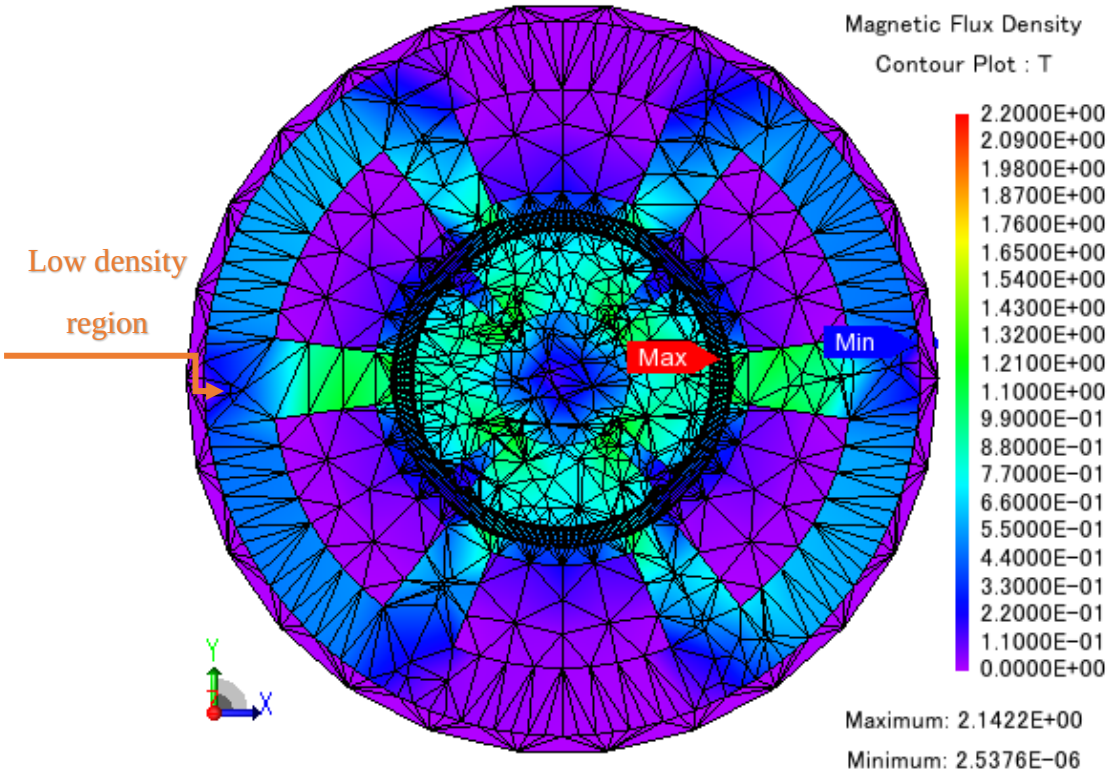

Figure 3.18 Flux density distribution on the third model XY cut

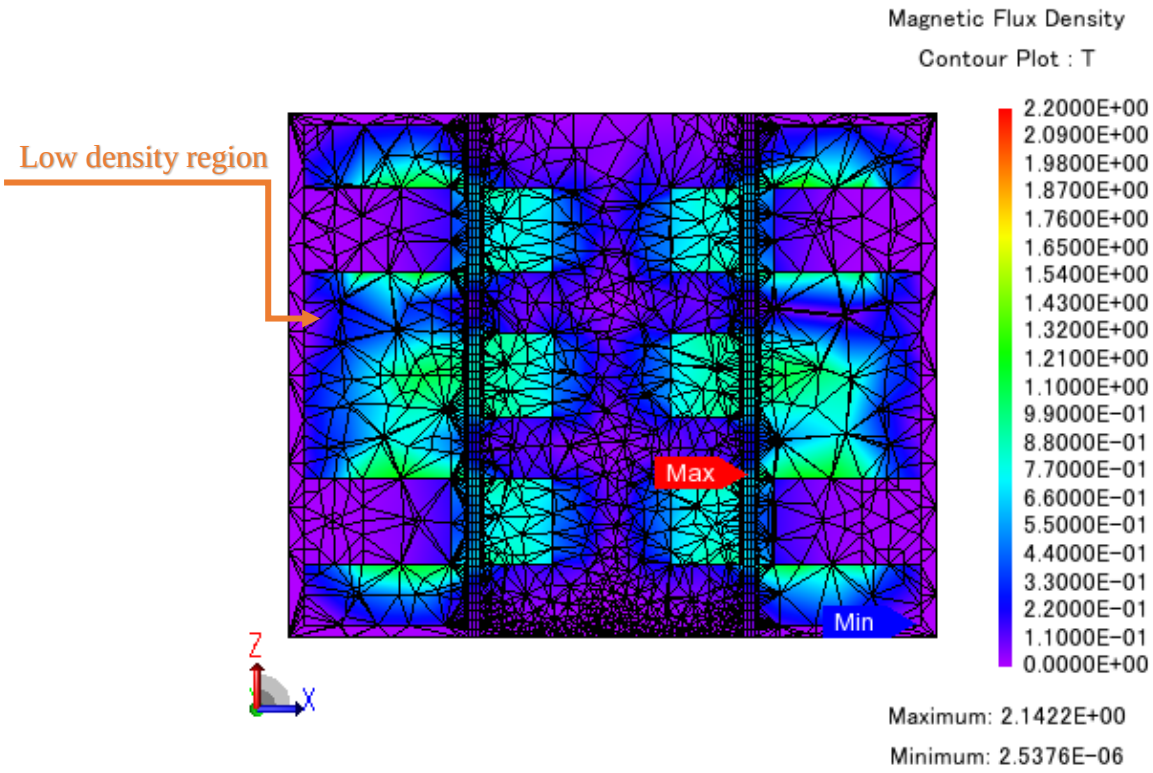

Figure 3.19 Flux density distribution on the third model XZ cut

3.4. Fourth version

In the fourth version, the stator teeth shape was modified, including shoes at the tips. The stator shoes increase the air gap area without modifying the stator teeth width and the slot area. The fourth 3D model is shown in Figure 3.20.

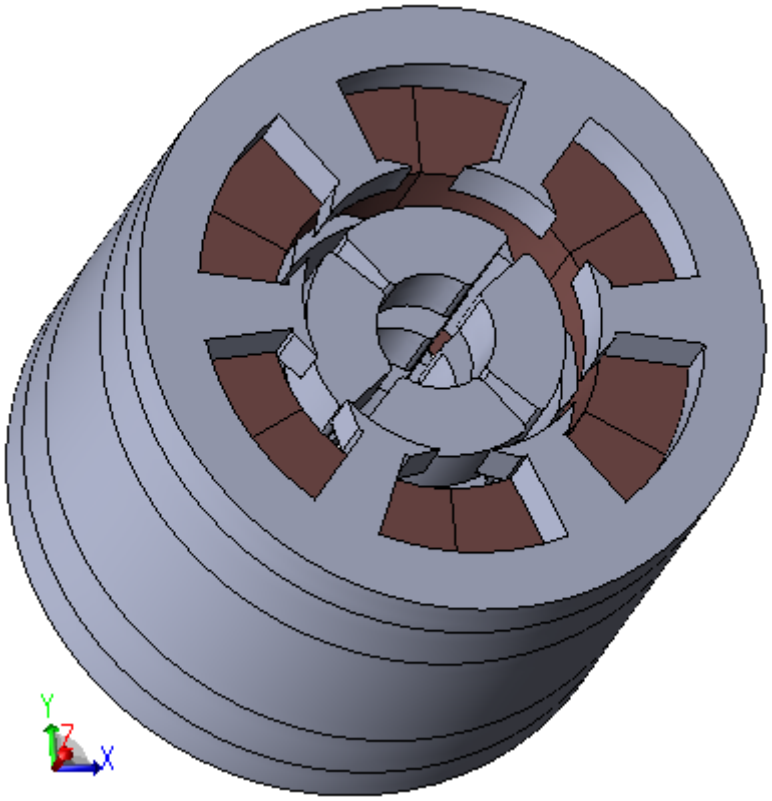

Figure 3.20 Fourth version of the inner rotor type motor

Average torque was changed from 1.71mNm to 2.10mNm for 1A RMS. The inclusion of the stator shoes caused a 23% increase in average torque and an increase in torque oscillation. A comparison of this result and the previous one is shown in Figure 3.21. The addition of shoes also caused a phase shift in the generated torque. Probably this shift will not cause any undesirable effects.

The teeth shoes capture more flux lines, increasing the overall torque density. Through Figure 3.22 and Figure 3.23 it is possible to see that density is higher near the pole tips, since the magnetic field crosses a smaller normal area than the tooth base. The shoe corners are highly saturated, but this does not offer an obstacle, since the stator teeth are unsaturated.

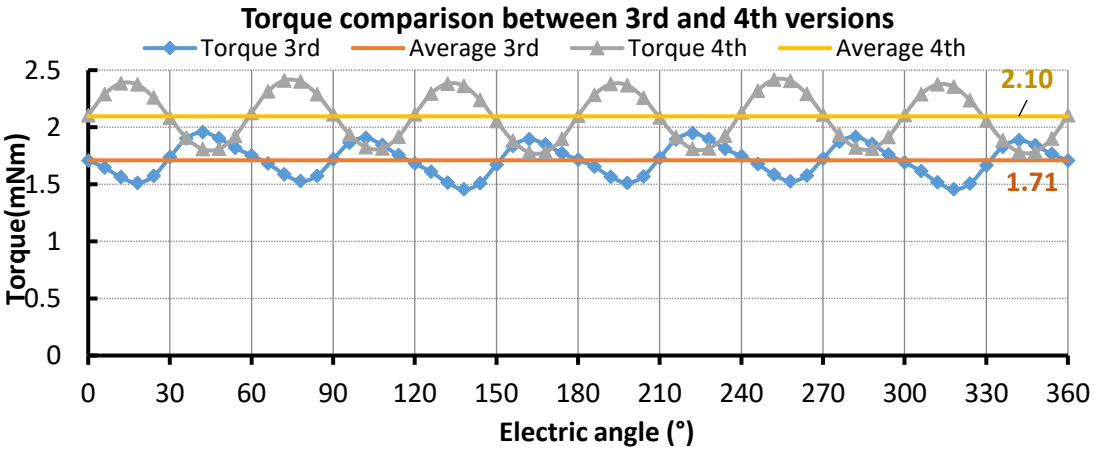

Figure 3.21 Torque comparison between fourth version and third version

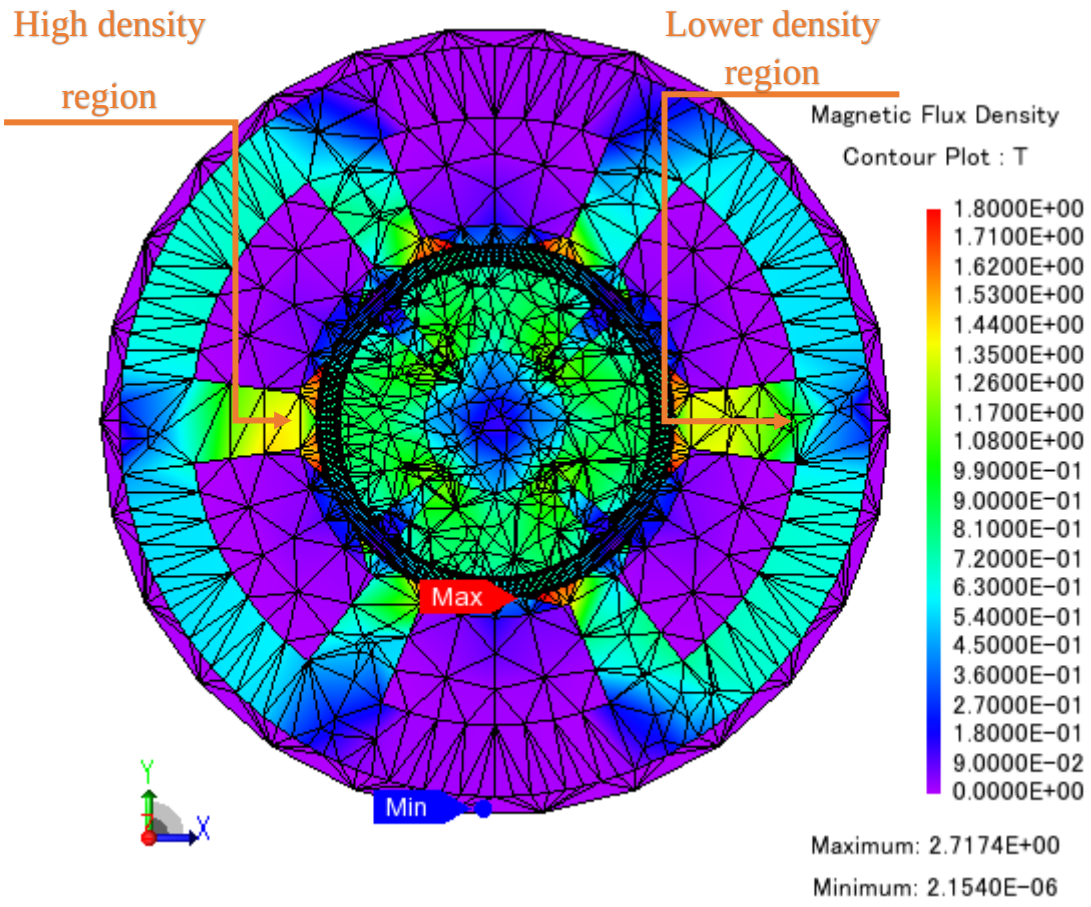

Figure 3.22 Flux density distribution on the XY plane

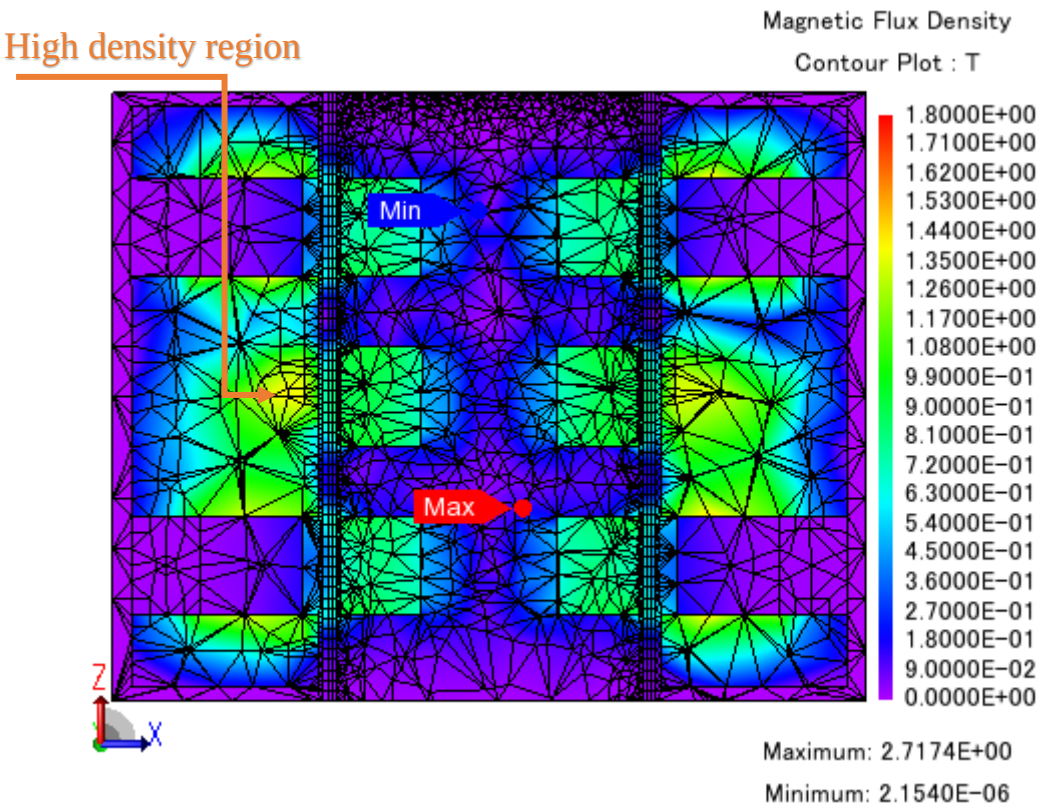

Figure 3.23 Flux density distribution on the XZ plane

3.5. Fifth version

A problem was perceived on the design of the fourth version. The rotor shaft must have a hole for fixing it to the rotating frame using a bolt, like shown in Figure 2.8. After increasing the permanent magnet length, the hole diameter became 4mm. To fit a bolt, at least 5mm is required. In the fifth version, the shaft diameter was corrected to 5mm. Since this implies a reduction in the average torque, the air gap length was also reduced from 0.65mm to 0.5mm. The rotor PM length was reduced from 2.35mm to 2mm.

The stack length was reduced from 17mm to 14.8mm, allowing more space for the radial bearings that were not designed yet. The permanent magnet heights were kept constant while the stator layers were reduced. A comparison is provided in Figure 3.24. Figure 3.25 shows the 3D model of version five.

Torque calculation results for 1A RMS phase current are shown in Figure 3.26. The average calculated values were changed from 2.10mNm to 2.22mNm for 1A. Results indicate that shortening the air gap has a bigger influence over the average torque than changes on the permanent magnet width.

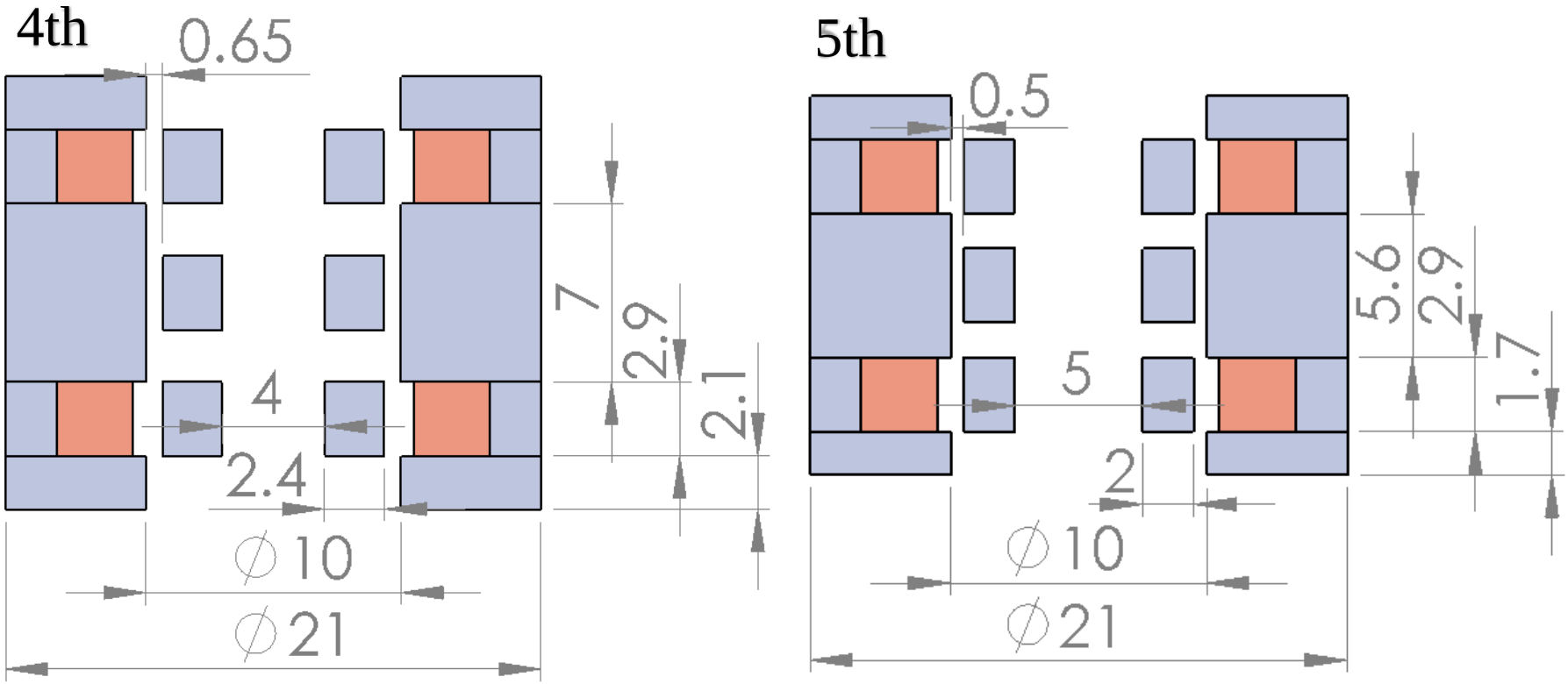

Figure 3.24 On the left, version 4 section cut. On the right, version 5 section cut

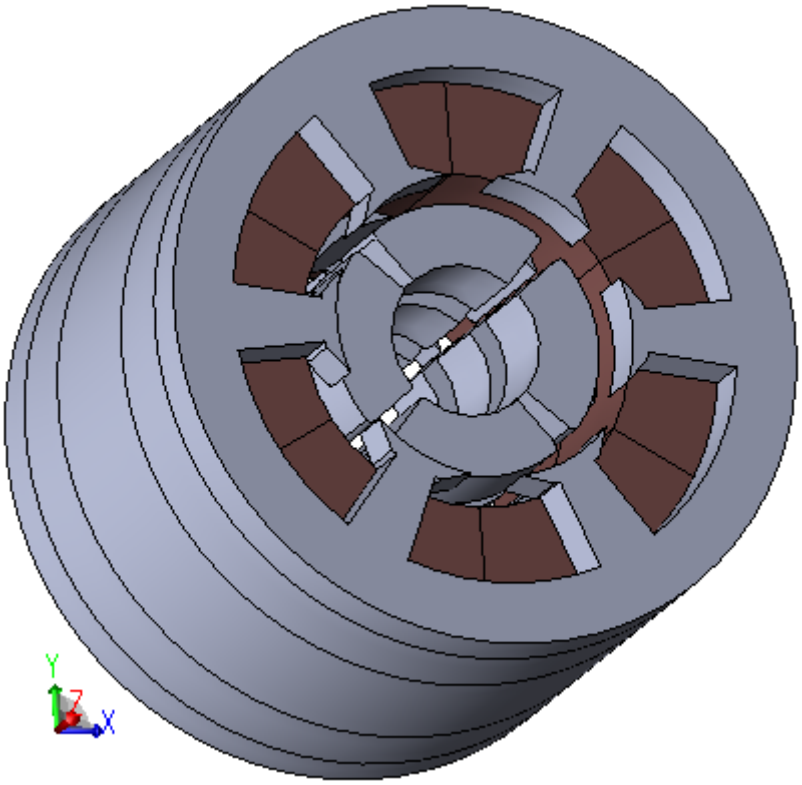

Figure 3.25 3D model of the fifth version

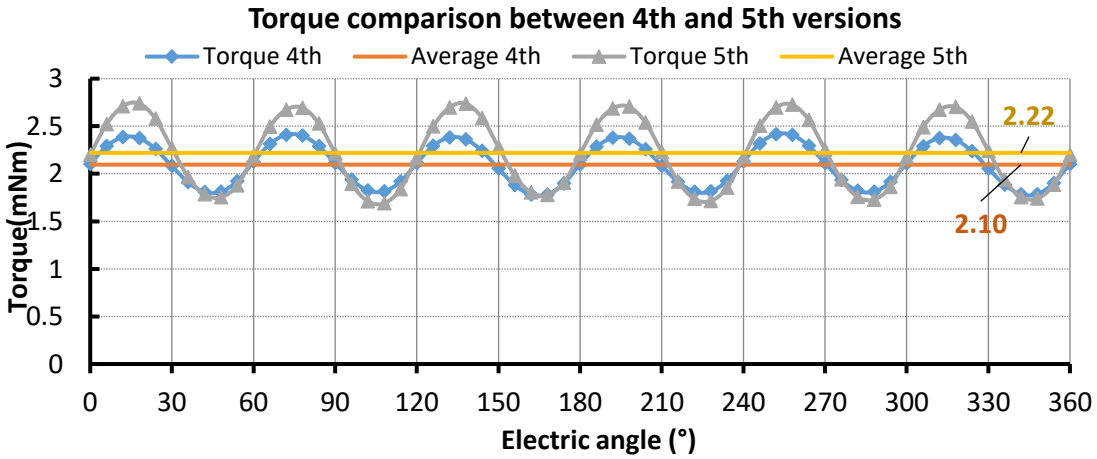

Figure 3.26 Calculated torque for the fifth version

The flux density distribution shown in Figure 3.27 and Figure 3.28 indicates that the stator shape can be optimized to improve flux density distribution

Reducing the air gap size implies that this case needs to be fabricated with a higher precision. This will improve attraction forces between rotor and stator. The severity of this effect was not yet considered in this step.

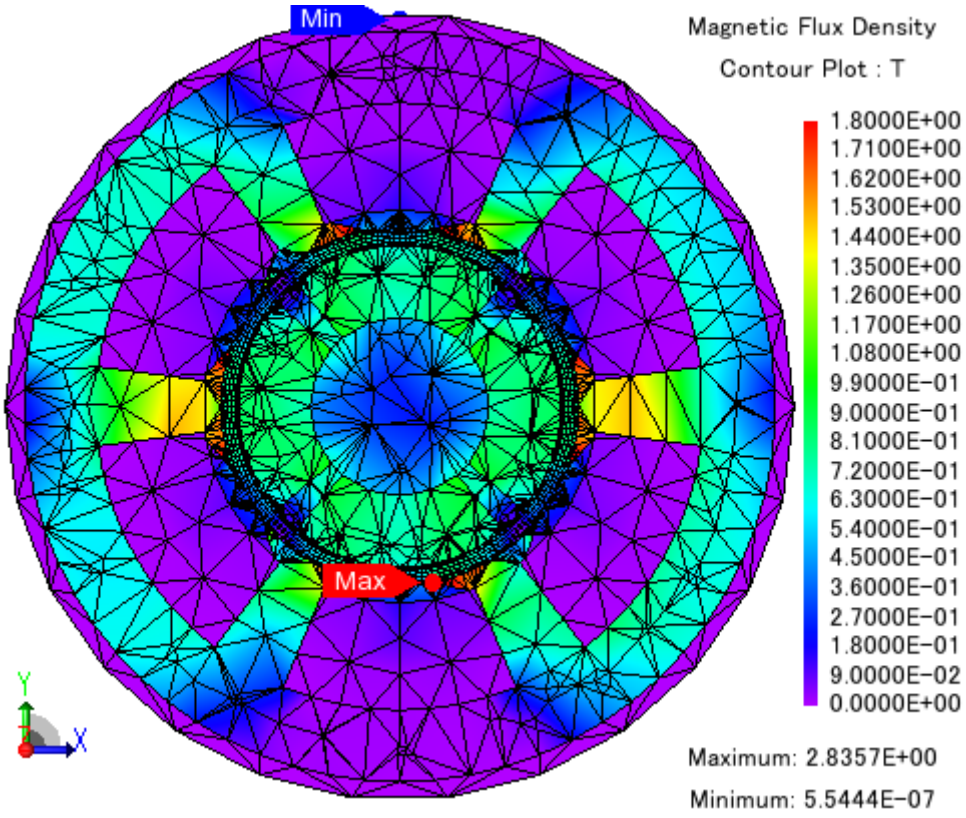

Figure 3.27 Flux density distribution on the XY plane in the fifth version

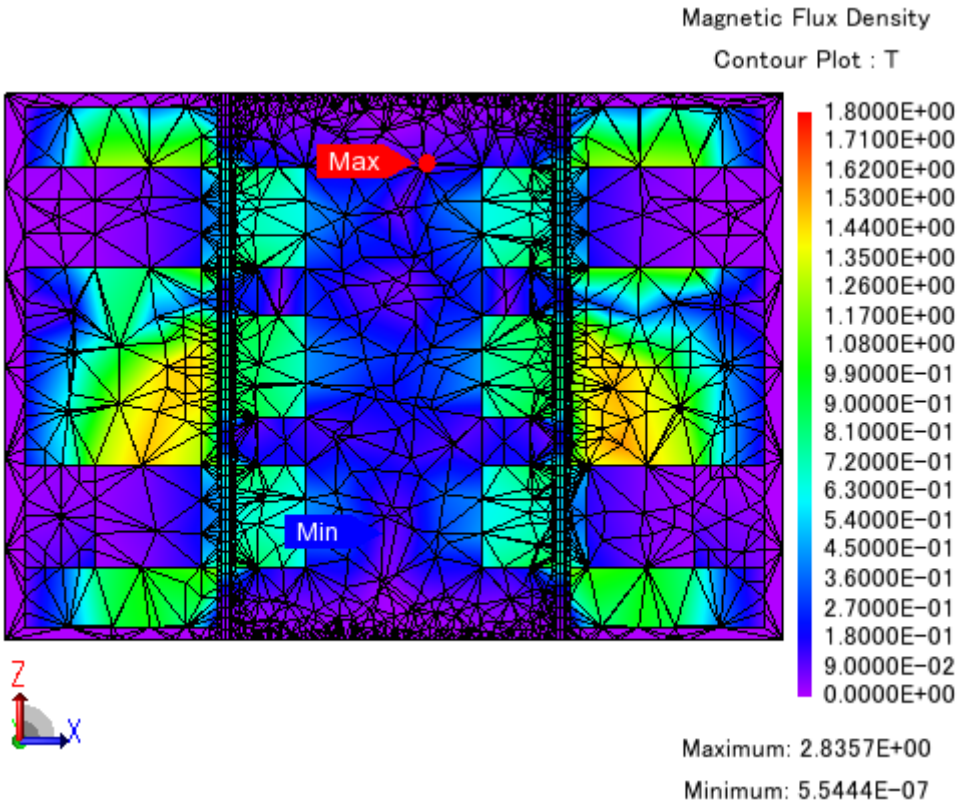

Figure 3.28 Flux density distribution on the XZ plane in the fifth version

3.6. Sixth version

In the sixth version, the stator was remodeled in an attempt to optimize the flux density distribution. This version was also the starting point for the analysis of radial passive bearing dimensioning.

The stator teeth were changed from an angular shape to a straight shape, like shown in Figure 3.29, to make the available area constant along the teeth, expecting flux density distribution to become more uniform. The stator slot is slightly increased without increasing the risk of saturation. Flux density in the stator yoke is also bigger, distribution became more uniform along the magnetic field path. This value of flux density inside the stator tooth is a little high. Even though for rated operation this density is acceptable, it presents risk of saturation when actively controlling the axial position.

The axial length was once again reduced to get the most compact rotor as possible. Now the permanent magnet height was also reduced, consequently the slot fill factor on the vertical *XZ* plane became more critical. The number of turns per coil had to be adjusted again. Figure 3.30 shows cross-sections of the sixth version. For the 6.9mm² area, the number of turns per coil was chosen as 20 for a slot fill factor of 36%.

Dimensions comparison between sixth and fifth version are shown in Figure 3.31.

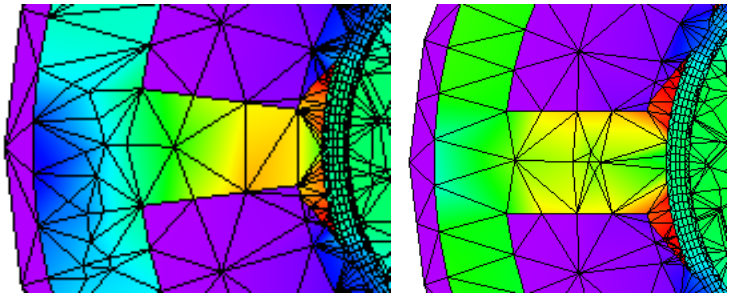

Figure 3.29 Stator teeth comparison: To the left, previous angular shape. To the right, the straight shape from the sixth version

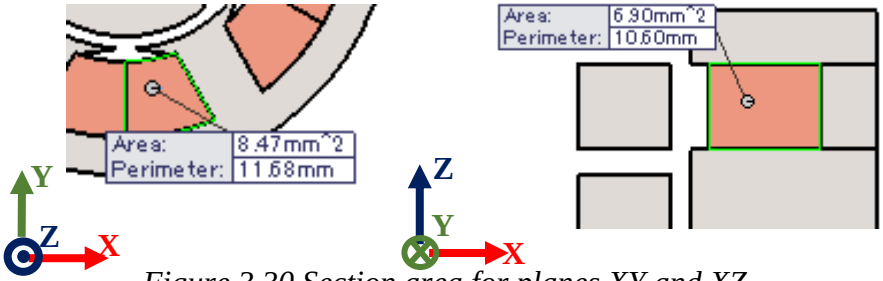

Figure 3.30 Section area for planes XY and XZ

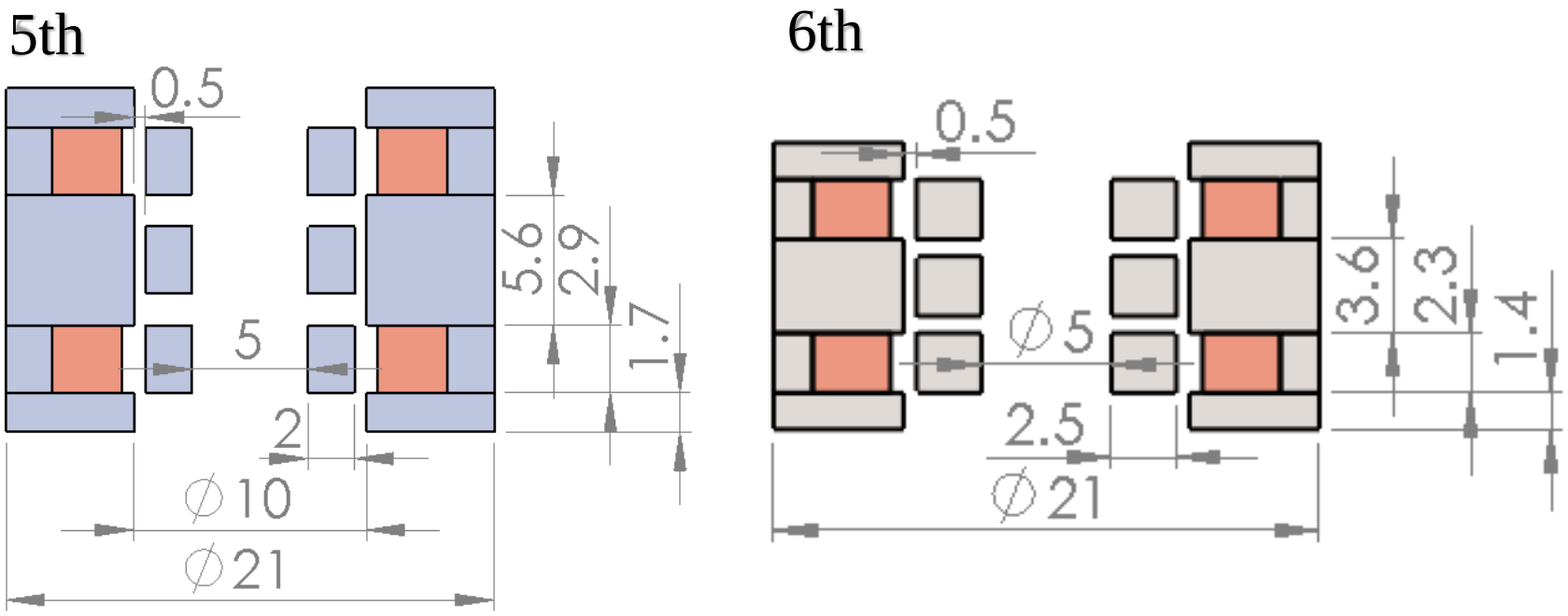

Figure 3.31 Dimensions comparison between 5th and 6th versions

The 3D model is shown in Figure 3.32.

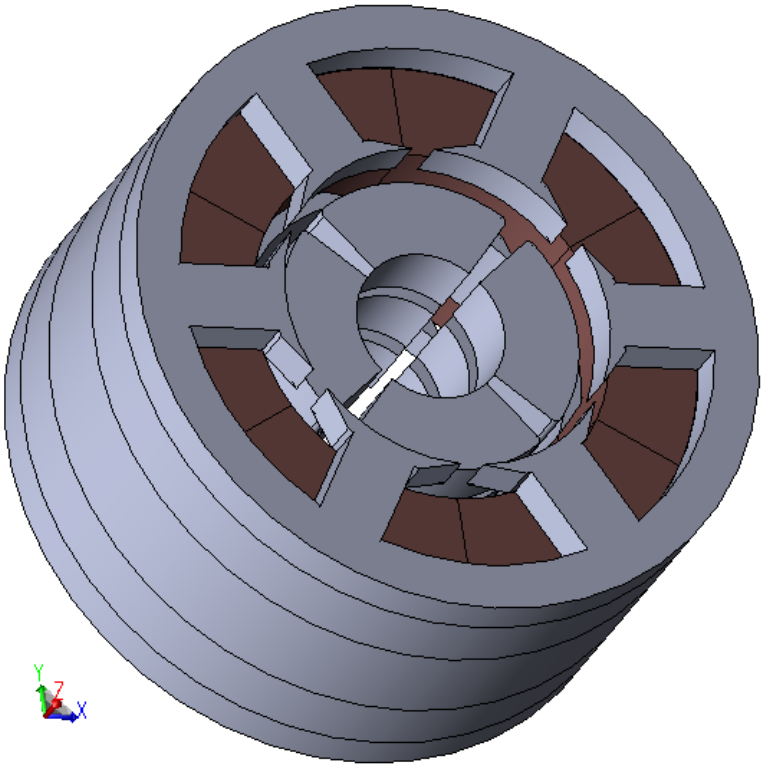

Figure 3.32 3D model of the sixth version

It was already expected that the average torque would be reduced due to the PM height difference. A smaller number of turns also results in a smaller average torque. Figure 3.33 shows the calculated torque for the sixth version. Due to reduction of air gap area and the change in number of turns per coil from 25 to 20, the average torque was sharply decreased from 2.22mNm to 1.33mNm. Some adjustments are needed in order to reach higher torques.

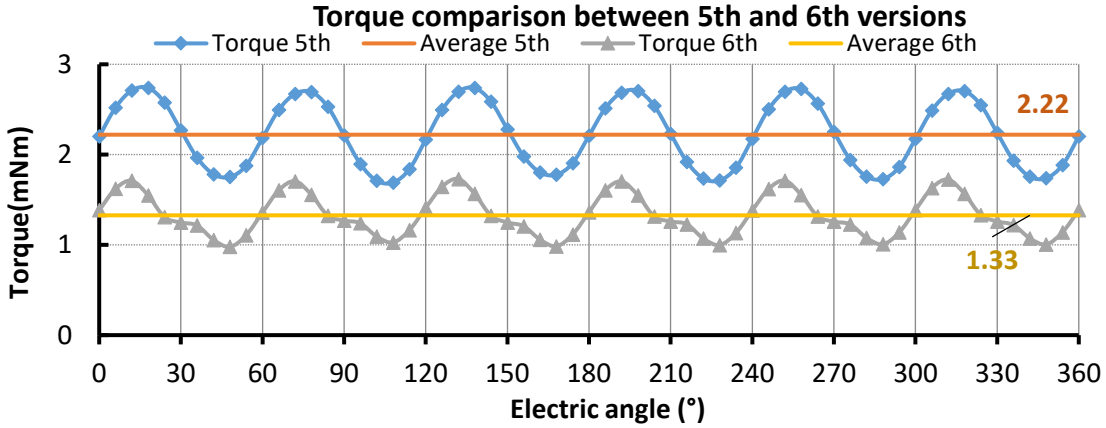

Figure 3.33 Calculated torque for the sixth version

Figure 3.34 shows flux density contour plot on maximum rotor displacements along the *x*-axis. By displacing the relative rotor position, while keeping currents equal to zero, it is possible to calculate the effect of the displacement component of radial forces. Ranging from -0.2mm to 0.2mm, forces are calculated through FEA. The result is plotted in Figure 3.35 and by first degree fitting we obtain the radial stiffness K_{rr}:

$$K_{rr} = \frac{\partial F_x}{\partial x} = 9.77\text{N/mm}$$

The severity of this radial stiffness is not yet known, since the rotor is not associated with the passive bearings yet.

In a similar manner, we can calculate the unstable axial forces contribution by interaction between rotor and stator. Figure 3.36 shows the flux density contour plot on maximum simulated axial displacement positions: z=-0.2mm and z=0.2mm.

Calculated forces are shown in Figure 3.37, it is possible to calculate the rotor axial stiffness, K_{zr}, as:

$$K_{zr} = \frac{\partial F_z}{\partial z} = 8.06\text{N/mm}$$

It is important to notice that there exists a big offset force due to the permanent magnet geometry. This is not a concern, since this offset can be eliminated by carefully adjusting the passive bearings.

Figure 3.38 shows the axial forces on the *z* axis, due to I_d current components. The rotor was kept in the central position while changing only the current. I_d current was varied from -20A to 20A. Through first degree fitting of the force-current curve, we obtain the force-current factor:

$$K_{zi} = \frac{\partial F_z}{\partial i} = 0.246\text{N/mm}$$

It is important to notice that the current induced force has an offset value due to the rotor axial force while in central position. After compensating this force, the force-current curve becomes the one shown in Figure 3.39. There is saturation after 10A. This implies that if forces above 2N are required for suspending the motor, high currents may be required. Through 3D modeling software, levitated mass is estimated as 16g, weight is calculated as 0.16N, reducing 0.6A the required current.

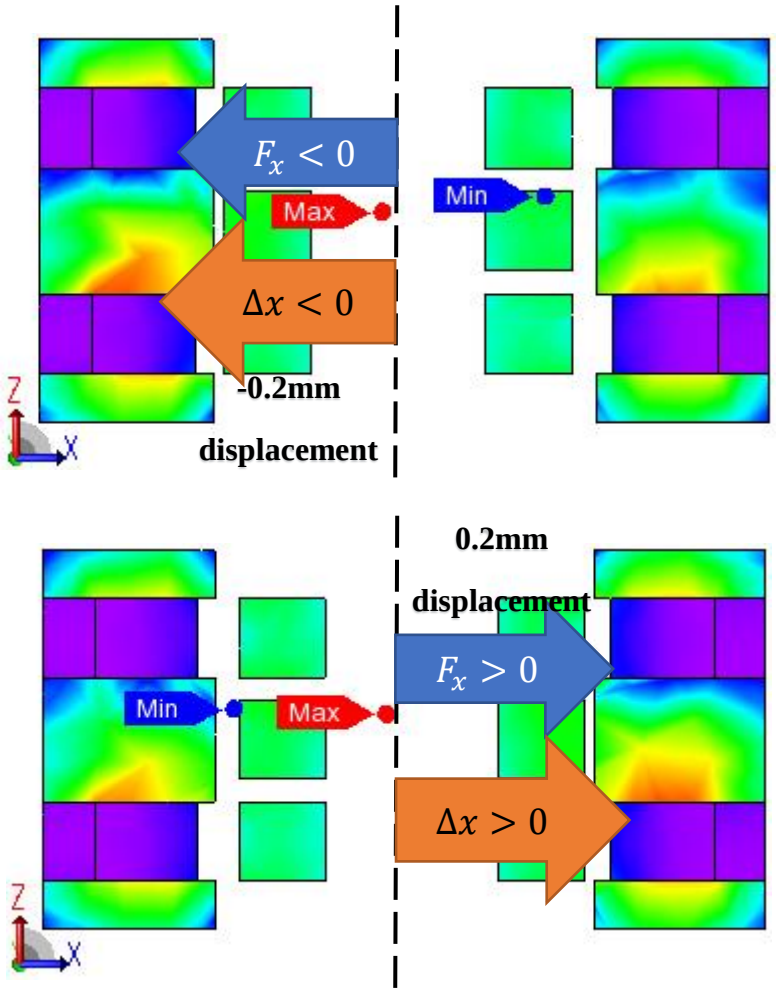

Figure 3.34 Range of radial displacement for radial stiffness calculation

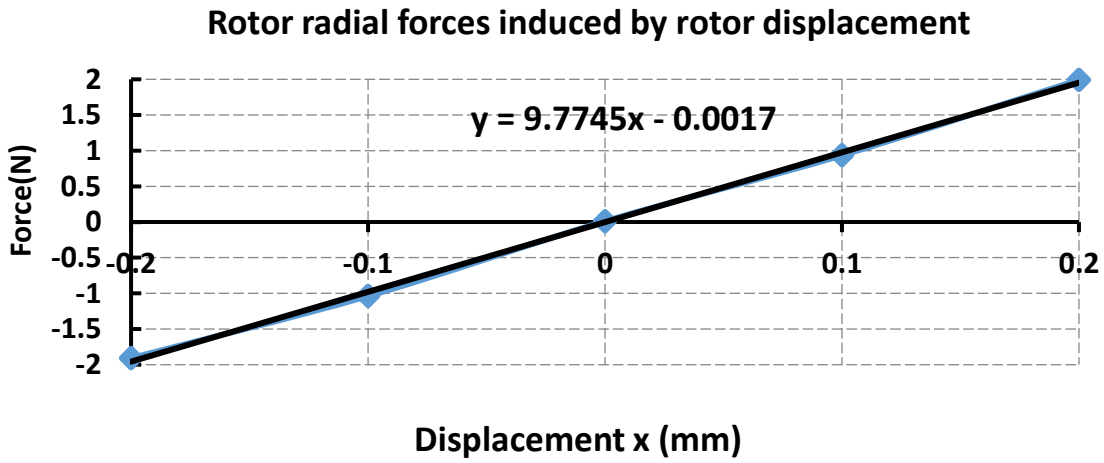

Figure 3.35 Rotor radial forces for version 6

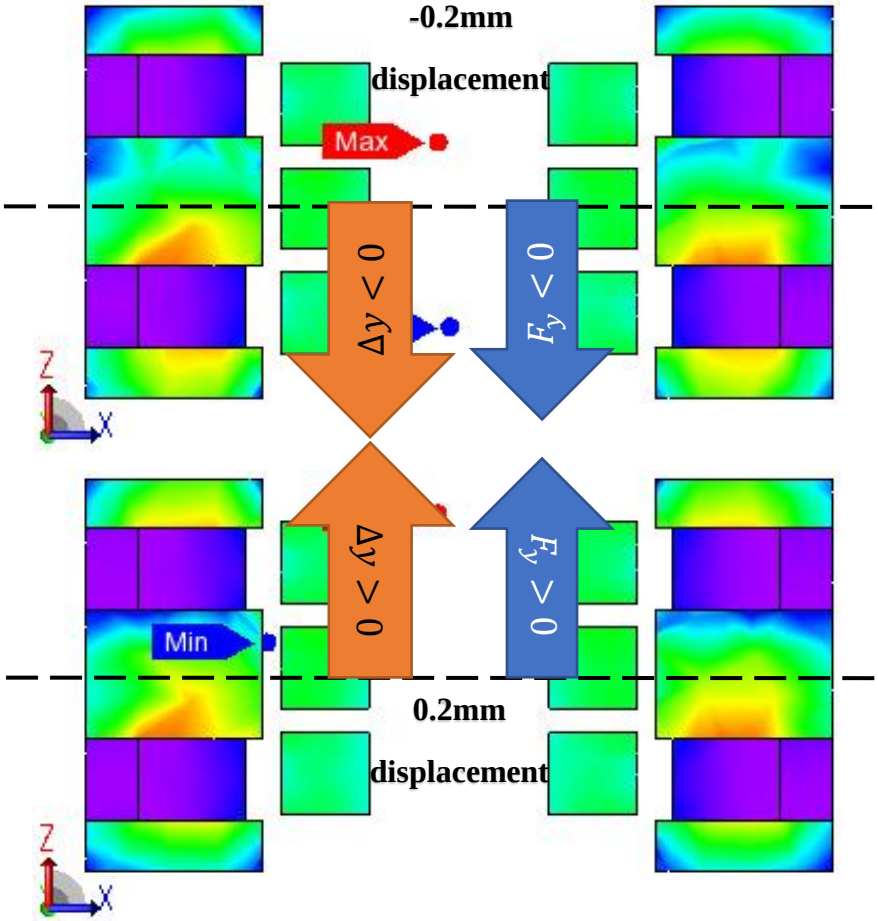

Figure 3.36 Rotor axial displacement

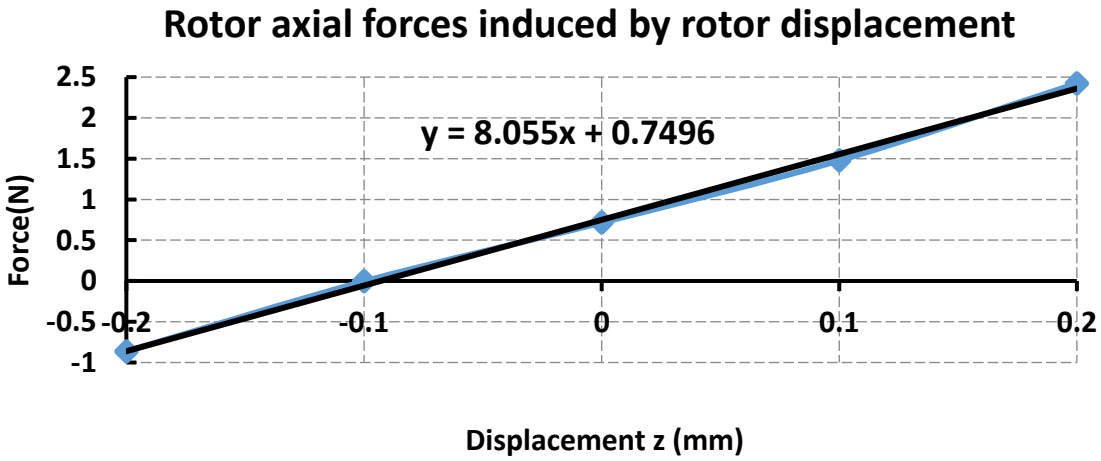

Figure 3.37 Axial forces along the z-axis due to rotor displacements

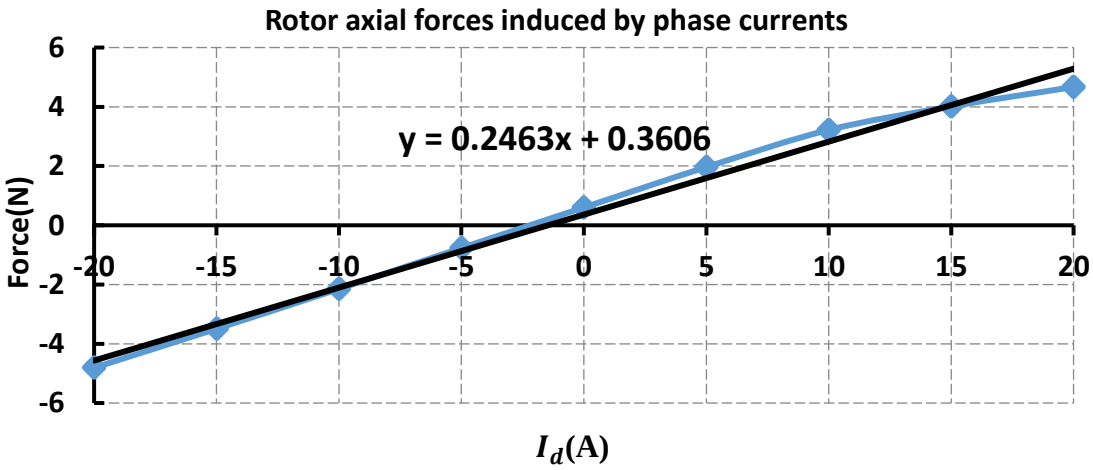

Figure 3.38 Axial forces when current is induced and rotor is centralized

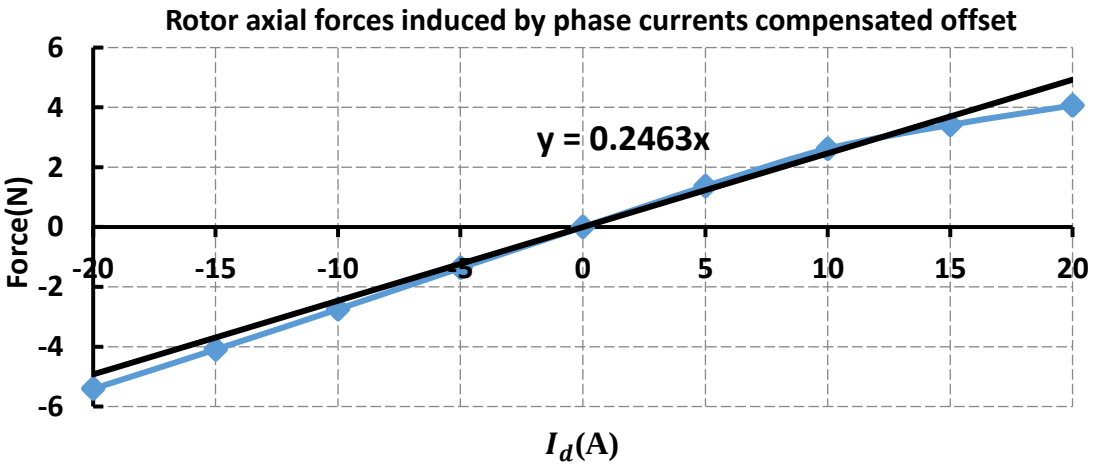

Figure 3.39 Axial forces induced by I_d current

3.7. Seventh version

The seventh version was the most compact one. The stack length was resized to 10.2mm, leaving reasonable clearance inside the 17mm target for inclusion of passive bearings. The stator teeth were enlarged while the stator yoke width was reduced. The stator slot area was reduced while keeping the same number of turns per coil from version 6. The slot fill factor became 38%. Figure 3.40 shows the dimensions of the seventh version. The height denoted as *h* was varied to analyze its influence over torque value.

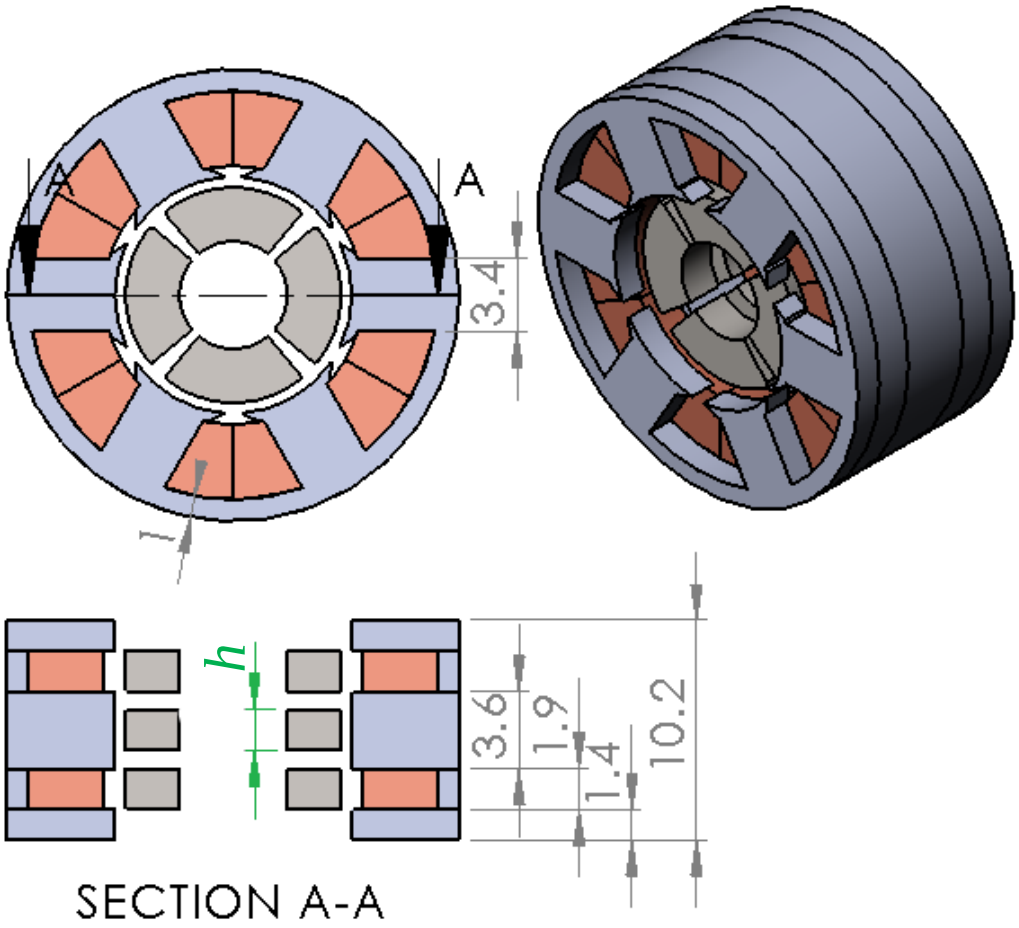

Figure 3.40 Seventh version

This time, torque was calculated with two different types of meshes, one with pole face elements size limited to 0.3mm and another one limited to 0.2mm. Figure 3.41 shows the face elements used for the FEA using 0.3mm limitation . For 0.3mm size, the total number of elements becomes 287339. If the size is limited to 0.2mm, the number of elements rises to 331157, implying the simulation will take a greater number of calculations.

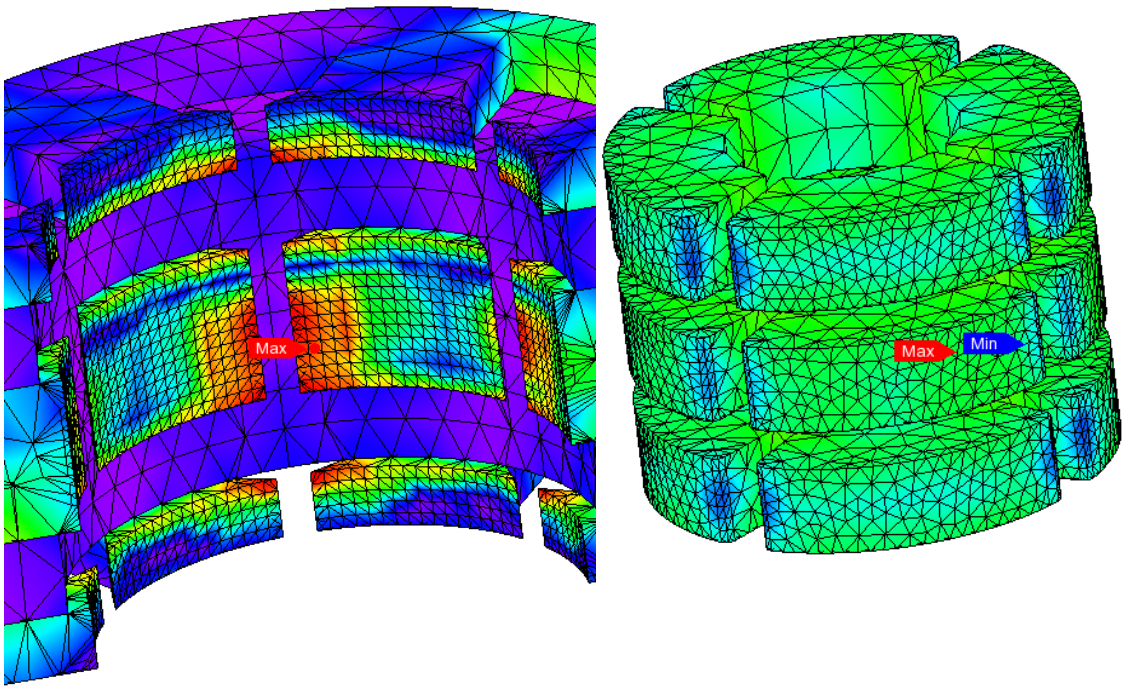

Figure 3.41 To the left: Stator face elements. To the right: Rotor face elements

3.7.1. Torque calculation

Torque analysis results for $h = 1.9mm$ are shown in Figure 3.42. From the results obtained, two things must be noticed. The first is that the average torques, 1.49mNm and 1.22mNm, for the 0.3mm and 0.2mm face elements mesh, respectively, are below the target. The second one is that the result for the less detailed mesh is 18% bigger than the more detailed mesh. This may lead to the intuitive conclusion that the highest detailed mesh should have the greatest number of elements as possible and the less detailed mesh is not dependable.

In an attempt to increase the average torque and to confirm the relation between calculated torque and level of details, version 7 was optimized by testing different values for height *h*. Increase in permanent magnet height enlarges the air gap area and is supposed to raise torque. Calculations were made for both kinds of meshes.

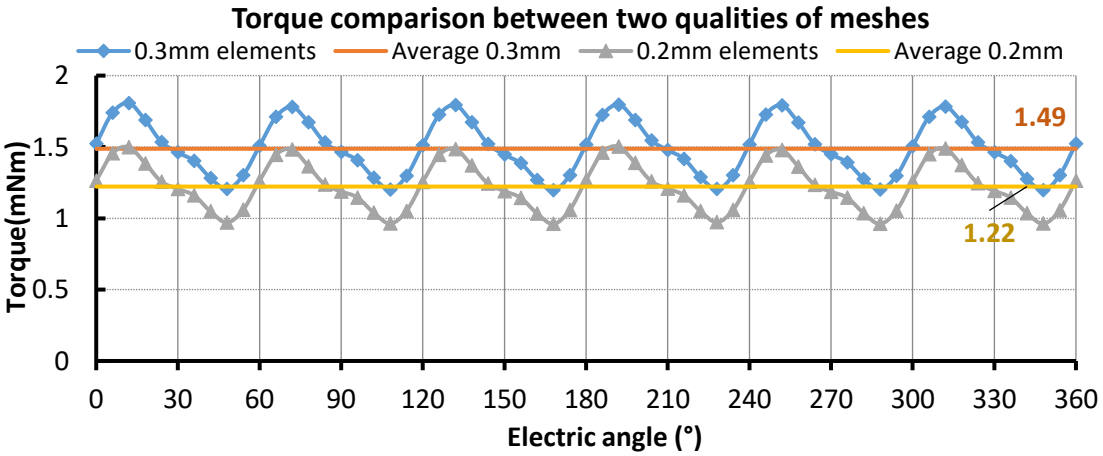

Figure 3.42 Torque calculations for the seventh version

Figure 3.43 and Figure 3.44 show torque values for a range of *h* values from 1.9mm to 2.9mm. Figure 3.44 shows that those results also have significant oscillation, but slightly smaller than results obtained for the 0.3mm limit. By analyzing the discrepancy between calculated torques and their respective tendency line, a tolerance margin can be estimated.

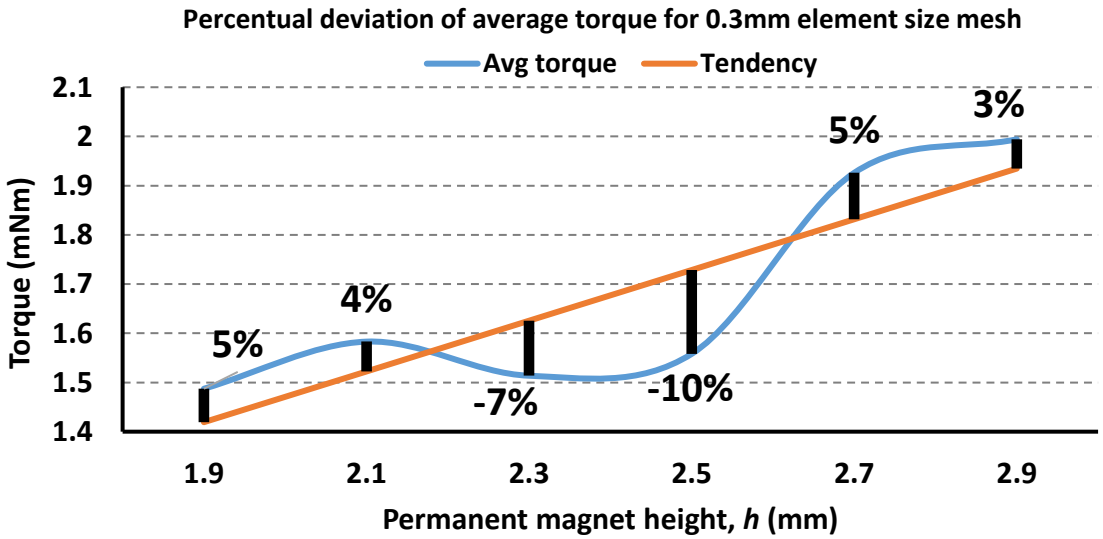

Figure 3.43 Calculated torque for a mesh with less detailed faces

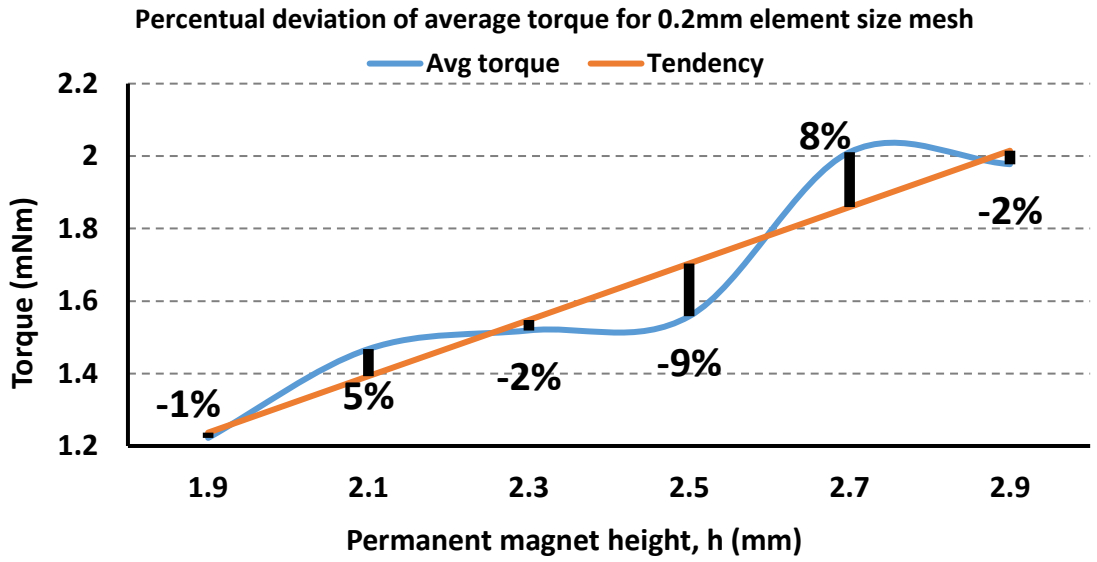

Figure 3.44 Calculated torque for a mesh with more face details

Considering that calculated percentages of discrepancy between tendency lines and values estimated through FEA are less or equal to 10%, we conclude that the actual torque should be inside an uncertainty margin of 20% from the tendency line.

Even though the plots from Figure 3.43 and Figure 3.44 are not monotonic crescent, the curves have a rising tendency. Following both results, the 2.9mm height PM is selected, because it has the highest torque tendency value, near 2mNm.

3.7.2. Radial stiffness

This section presents radial forces calculated for each *h* value ranging from 1.9mm to 2.9mm. The radial force plot is shown in Figure 3.45. Radial stiffness values calculated through basic first-degree fitting are shown in Figure 3.46. Values range from 8.8N/mm to 11.5N/mm. The calculated relation between PM height and radial stiffness was not linear. There was a big difference for the 2.5mm PM.

It is not possible to know if this increased value of radial stiffness will be acceptable or not. To evaluate this, first we need to design the passive bearing rings that are going to stabilize the rotor radial position.

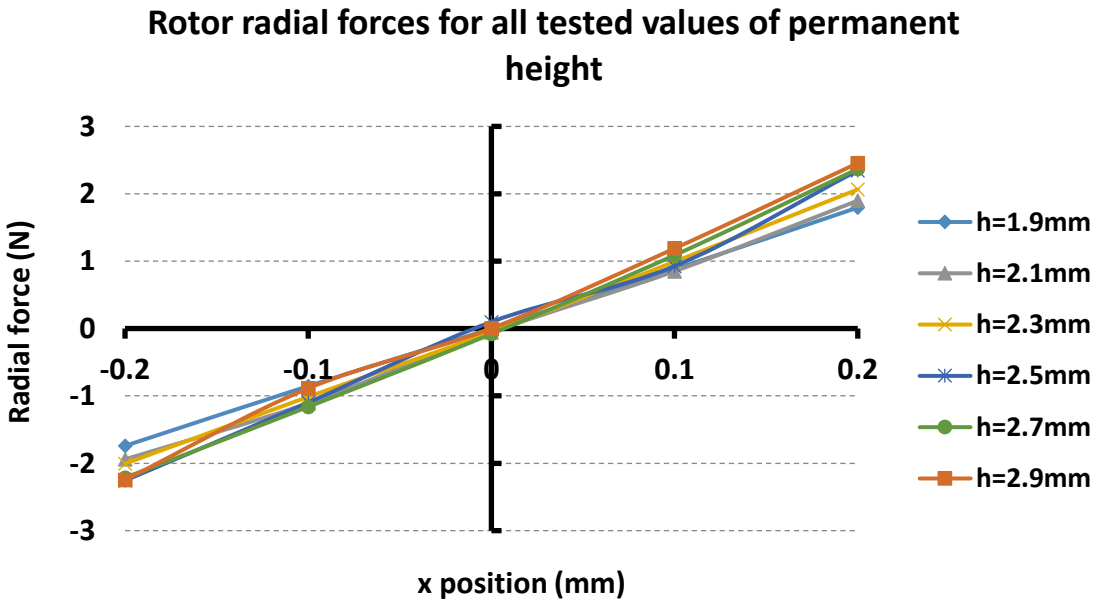

Figure 3.45 Rotor radial forces for all tested permanent heights, h

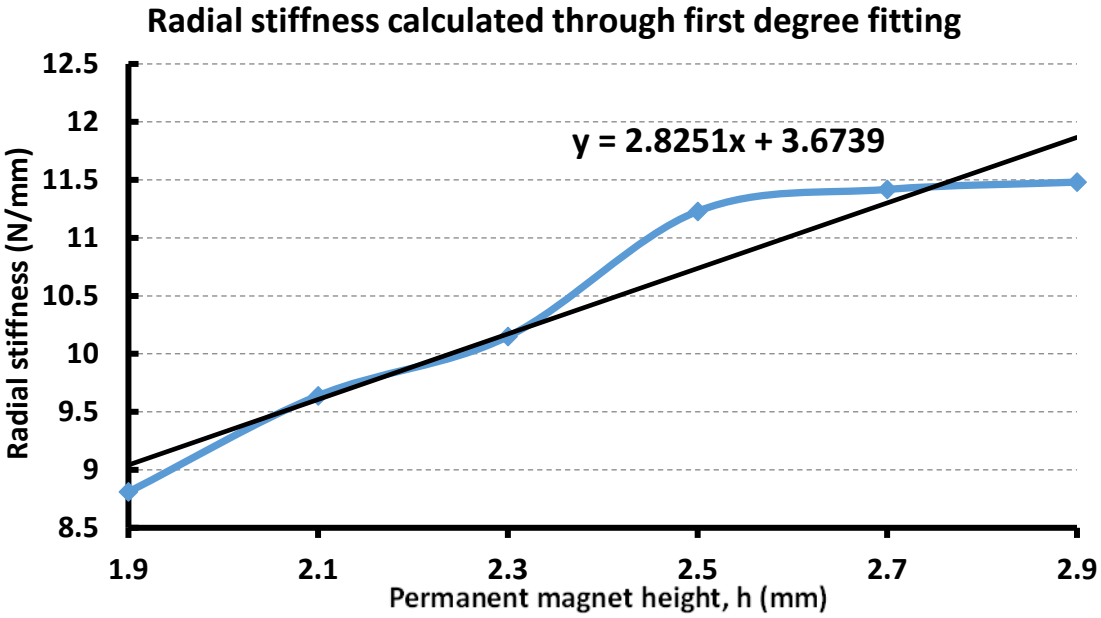

Figure 3.46 Radial stiffness for many heights of PM in version 7

3.7.3. Axial stiffness

As seen in Figure 3.47, the angular coefficient for the axial forces versus displacement curves was kept practically constant. On the other hand, an increase in the permanent magnet height gave the axial forces an offset. In principle, this nullifies the linear aspect of the axial position forces control, but since the unstable axial forces from the passive radial bearings are usually dominant on single drive axially controlled

bearingless motors, it is possible to compensate this offset by setting a very slight displacement in the relative axial position of the passive bearings. Figure 3.48 shows the offset values for all analyzed cases of PM height. For the interval considered, it can be approximated by a fourth degree curve.

The maximum currents that must be supplied by the control system can only be calculated after selecting the passive bearings.

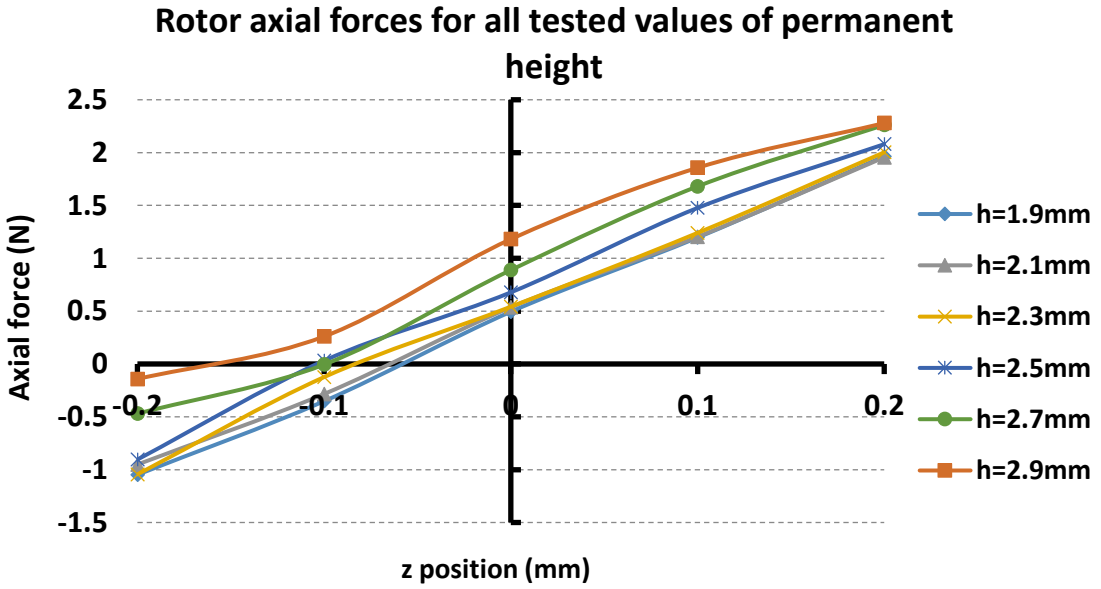

Figure 3.47 Axial forces versus axial displacement for all cases of the seventh version

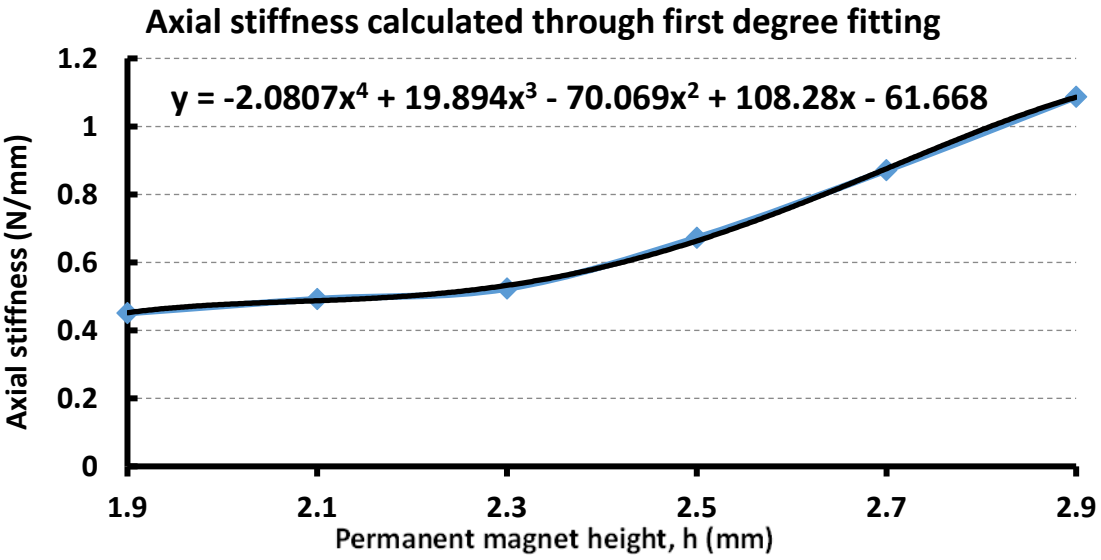

Figure 3.48 Axial force offset values for all attempted heights of central rotor permanent magnet

3.7.4. Unstable rotor torques

Torque values around the *x*-axis were calculated for tilting angles between -1° and 1°. As seen in Figure 3.49, the tilting torques were not greatly affected by the change in the permanent magnet height. All torques calculated do not have a linear behavior. The highest torque values are -0.77mNm and 0.90mNm. The passive magnetic bearings must be designed in order to compensate the tilting torque values.

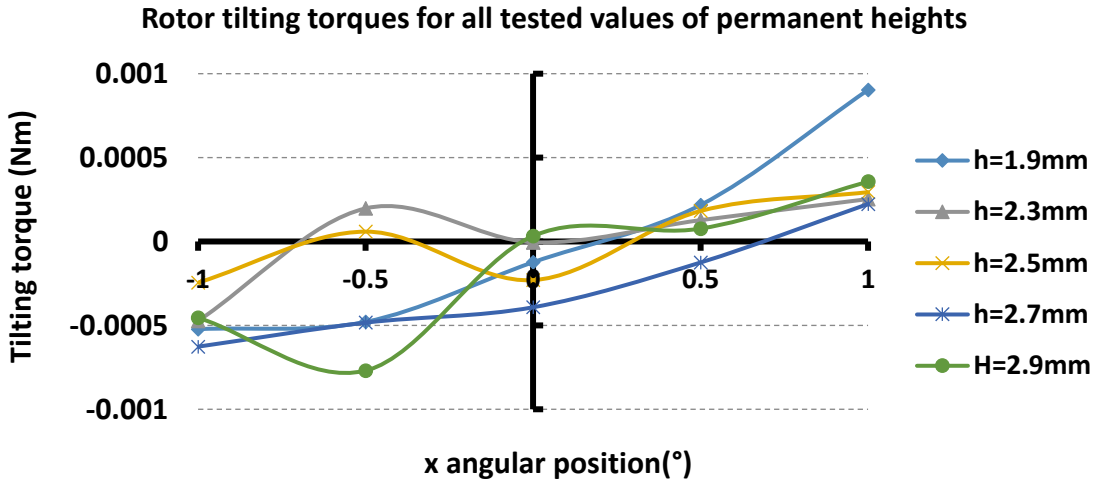

Figure 3.49 Tilting torques around x-axis

3.7.5. Force-current factor

Axial forces induced by currents were calculated by keeping the rotor in the central position while supplying currents with only I_d components. The results for heights 1.9mm and 2.9mm are shown in Figure 3.50. As expected from the results obtained for the axial stiffness analysis, the value of $K_{zi} = \frac{\partial F_z}{\partial i}$ is practically the same, but the offset on force is noticeable. It is also possible to notice a saturation region after 10A. This is caused by the bias flux from the permanent magnets. Flux density distribution for the highest evaluated current ($i_d = 20A$) is shown in Figure 3.51 and Figure 3.52. The Max and Min points shown in the section cuts actually represent points in the 3D model that didn't appear in the cuts.

Still it is not possible to estimate maximum required current for axial stabilization, because passive bearings were not yet designed.

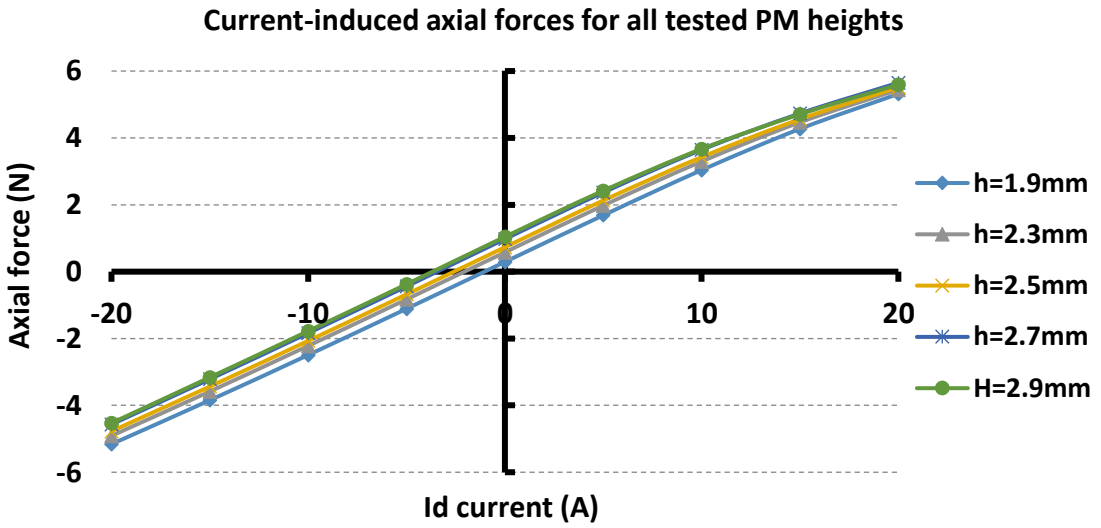

Figure 3.50 Current-induced forces on the seventh version

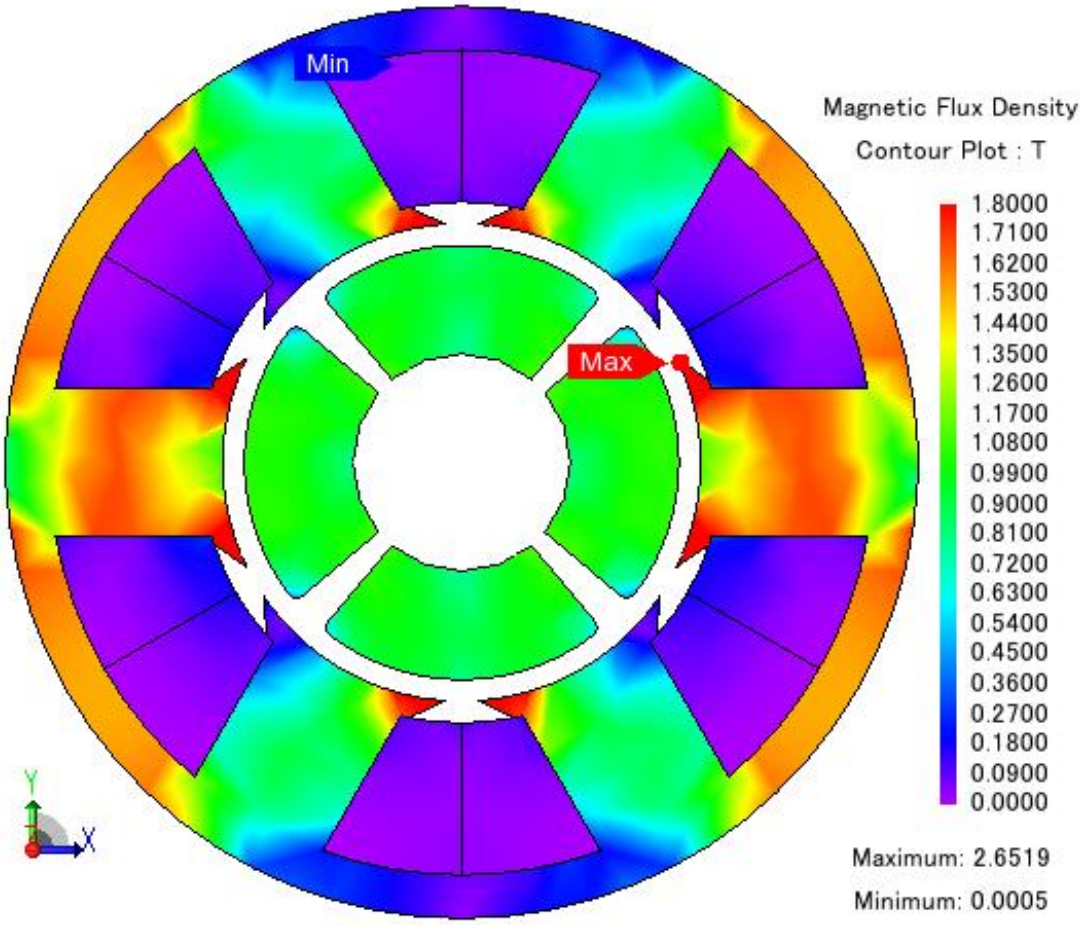

Figure 3.51 Flux density distribution in the xy cross-section for the highest current evaluated in the force-current calculation ($i_d = 20A$)

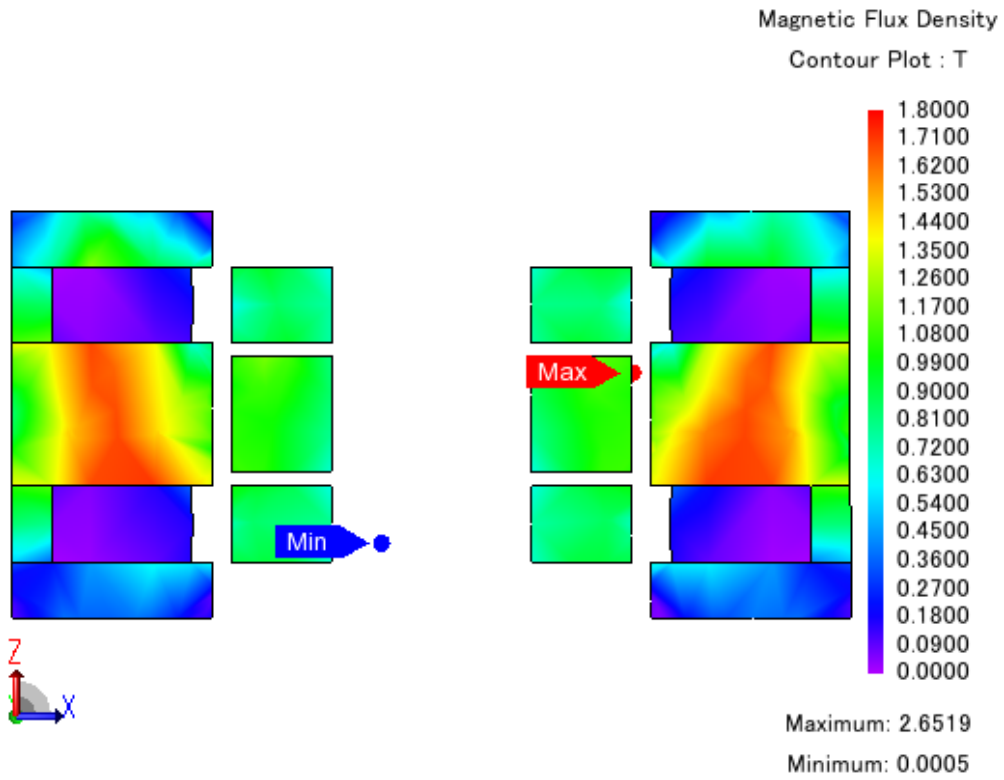

Figure 3.52 Flux density distribution in the xz cross-section for the highest current evaluated in the force-current calculation ($i_d = 20A$)

3.8. Improvements achieved

The seventh version achieved 2mNm average torque at 1A RMS, higher than the 1.39mNm value from the second version. It also became more compact, allowing space for placing radial bearings inside the 17mm height specification. Further development of the model is tied to the dimensioning of the passive bearings. In the fourth chapter, some proposals of radial bearings are analyzed.

4.Passive bearing dimensioning

It is possible to further improve the torque density of the model. By changing the height of the vertical *XZ* section slot area it is possible to adjust the number of coils while respecting the 40% maximum slot fill factor. On the other hand, an increase in the axial length means that there will be less space available for the passive bearings. Since unstable forces on the rotor were investigated in the seventh version, it is possible to devise options of passive radial bearings. In this chapter some passive bearing structures are presented. After taking them into consideration, the final version of the motor can be modeled.

To achieve radial stabilization, the passive magnetic bearing must have radial stiffness high enough for compensating the unstable radial attraction forces between rotor and stator. Figure 4.1 exhibits one of the proposals of passive magnetic bearing structure. It is composed by two rings. The inner one is stuck to the rotor shaft, while the outer one is fixed to the stator frame. The motor model with passive magnetic bearings attached becomes a stack like shown in Figure 4.2. It is desirable that at least a clearance of 0.5mm be kept between the rings and the stator structure to ensure that attraction forces between the bearing and stator will not affect balance.

The repulsive magnetic forces between the inner and the outer parts depends majorly on the shape of the bearings. Repulsive forces become stronger when the air gap area is increased or the air gap length is reduced.

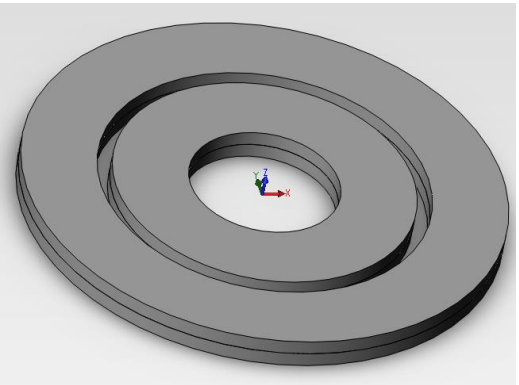

Figure 4.1 Passive magnetic bearing

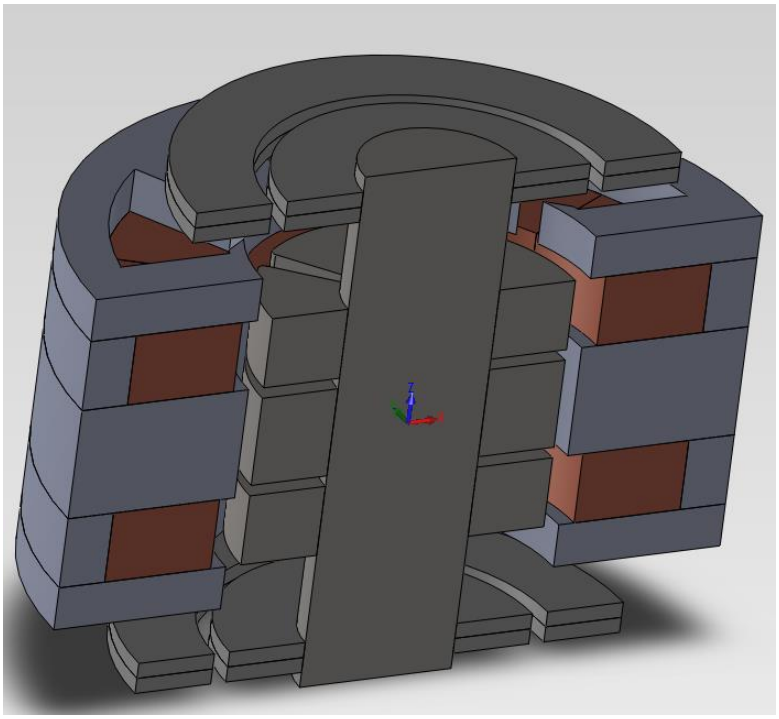

Figure 4.2 Motor model with passive bearings

4.1. Radial forces calculation

Stable radial forces can be adjusted by increasing or decreasing the airgap area and length. A certain minimum radial stiffness may be required for minimizing radial oscillations, but it is constrained by space limitations. Also, big stable radial forces imply even bigger unstable axial forces and bigger currents required for axial stabilization. In case the force-current factor, $\frac{d_z}{d_y}$, is not big enough, the axial position may become uncontrollable. This presents a limitation for radial passive bearings effectiveness.

Different models were designed by adjusting the ring diameters and heights while keeping a constant air gap of 0.5mm, same as the motor. Through FEA it is possible to estimate their respective radial stiffness characteristics. The ring attached to the rotor is displaced along the *x*-axis from position *x*=-0.2mm to *x*=0.2mm in steps of 0.1mm, in a procedure similar to the one used for calculating the rotor radial forces. Maximum displacements are shown in Figure 4.3. Since the only displacement occurs in the *x*-axis, we can say that these are the radial forces.

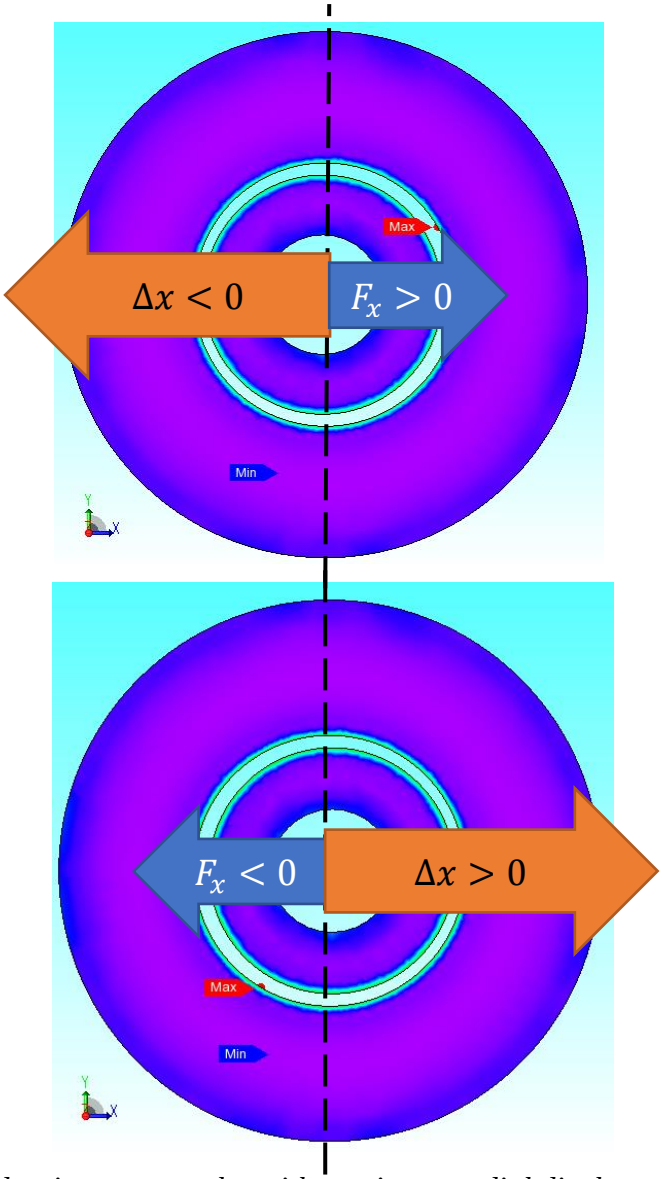

Figure 4.3 Flux density contour plot with maximum radial displacement on a passive bearing.

4.2. Axial forces calculation

The axial forces are calculated in a similar way to the one from the radial forces. The ring attached to the rotor is displaced along the *z*-axis from position *z*=-0.2mm to *z*=0.2mm in steps of 0.1mm, like shown in Figure 4.4. Forces in the *z*-axis are calculated as outputs of the FEA for each step, generating five points in total.

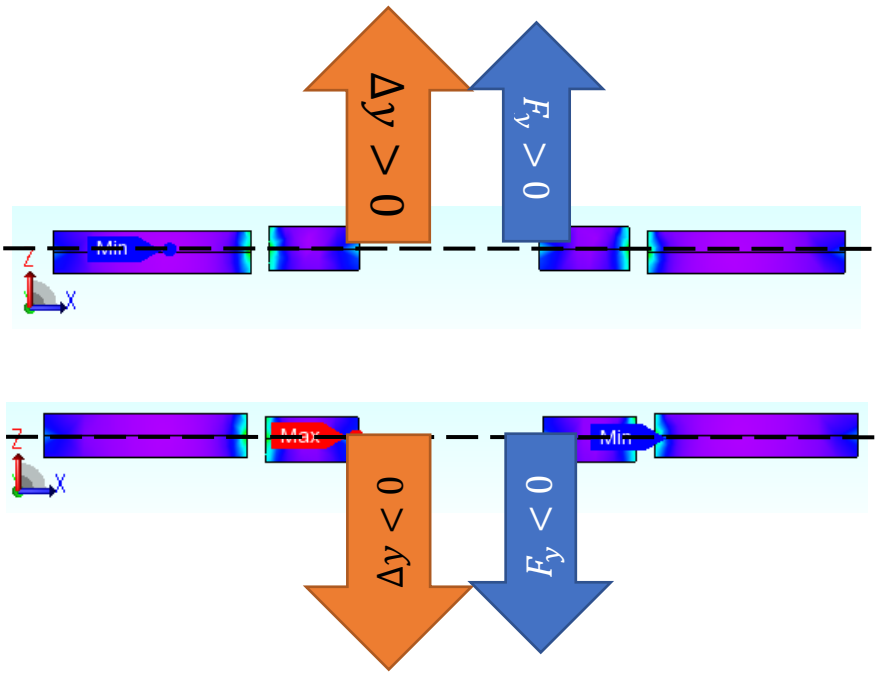

Figure 4.4 Flux density contour plot with maximum axial displacement on a passive bearing

4.3. Tilting torques

The diagram in Figure 4.5 shows a radial passive bearing, its repulsive magnetic forces and distance vectors from point O in the mass center to the force contact points P_1, P_2, P_3 and P_4. This figure supposes a very small tilting in the counterclockwise direction around the *x*-axis. The total torque in *x*-axis is given by:

$$\overrightarrow{T_x} = \overrightarrow{d_1} \times \overrightarrow{F_1} + \overrightarrow{d_2} \times \overrightarrow{F_2} + \overrightarrow{d_3} \times \overrightarrow{F_3} + \overrightarrow{d_4} \times \overrightarrow{F_4},$$

being the result of a counterclockwise rotation, a positive $\overrightarrow{T_x}$ on *x*-axis will be an unstable torque.

Analyzing the tilting torque stability is difficult when using the diagram from Figure 4.5. So, all the force vectors $\overrightarrow{F_n}$ are decomposed in radial and axial components, $\overrightarrow{F_{yn}}$ and $\overrightarrow{F_{zn}}$, respectively.

Figure 4.6 shows a diagram of the components from forces $\overrightarrow{F_n}$ shown in Figure 4.5. Distances d_y and d_z are the sizes of the lever arms along *y*-axis and *z*-axis.

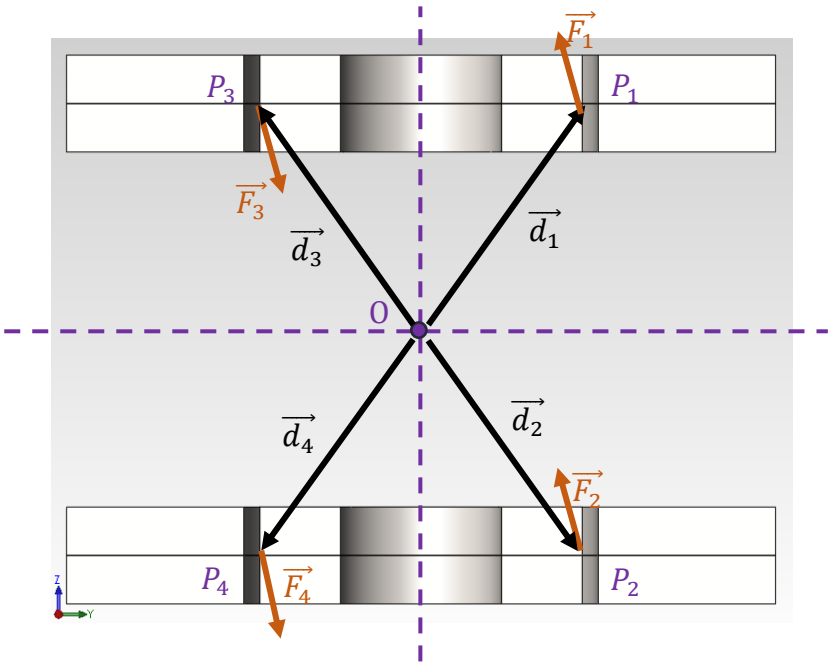

Figure 4.5 Repulsive forces over the passive bearing ring for a small counterclockwise rotation

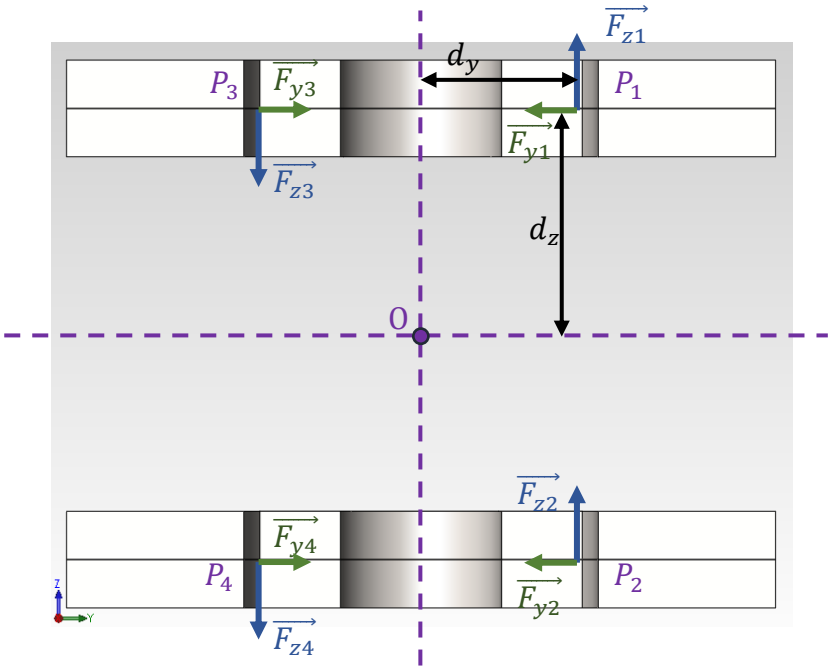

Figure 4.6 Force components over the passive bearing ring for a small counterclockwise rotation

Torque contributions from the radial forces are given by:

$$T_{radial} = d_z\left(F_{y1} - F_{y2} - F_{y3} + F_{y4}\right),$$

where a positive torque is directed towards the counterclockwise direction and a negative torque is directed in the clockwise direction.

It is important to notice that the sign of T_{radial} is given by the term $F_{y1} - F_{y2} - F_{y3} + F_{y4}$. If a tilting in the counterclockwise direction occurs, points P_2 and P_3 approach the outer ring and radial repulsion forces F_{y2} and F_{y3} become stronger than in the central position. Simultaneously, P_1 and P_4 move away from the outer ring, weakening forces F_{y1} and F_{y4}. Consequently, both the term $F_{y1} - F_{y2} - F_{y3} + F_{y4}$ and T_{radial} are negative. If a tilting occurs in the clockwise direction, force variations are reversed and T_{radial} becomes positive. Considering that the torque signal always opposes the angular tilting, torque T_{radial} is stable for small displacements.

Torque contributions from axial components are given by:

$$T_{axial} = d_y(F_{z1} + F_{z2} + F_{z3} + F_{z4}),$$

if the ring is rotated in the counterclockwise direction, all F_{zn} forces generate positive torques, thus unstable. If the ring is rotated in the clockwise direction, F_{zn} values become negative, generating negative torques, also unstable. Therefore, T_{axial} is always unstable.

Total tilting torque T_{res} is equal to:

$$T_{res} = T_{radial} + T_{axial}\,.$$

It is not possible to stabilize the tilting torques actively, controlling just the axial position. Also, increasing the radial forces will not solve the issue, since an increase in radial forces implies an even bigger increase in the axial forces. The only solution is designing the bearing structure to be inherently stable, so for counterclockwise displacements:

$$T_{res} = d_y(F_{z1} + F_{z2} + F_{z3} + F_{z4}) + d_z\left(F_{y1} - F_{y2} - F_{y3} + F_{y4}\right) < 0\,.$$

Stability is ensured by constraining d_z and d_y. Considering that T_{radial} and T_{axial} always have opposite signs:

$$T_{res} < 0 \Leftrightarrow \left|d_z\left(F_{y1} - F_{y2} - F_{y3} + F_{y4}\right)\right| > \left|d_y(F_{z1} + F_{z2} + F_{z3} + F_{z4})\right|$$

$$\frac{d_z}{d_y} > \left|\frac{F_{z1} + F_{z2} + F_{z3} + F_{z4}}{F_{y1} - F_{y2} - F_{y3} + F_{y4}}\right|.$$

The $\frac{d_z}{d_y}$ condition implies that a minimum ratio from d_z to d_y must be kept to ensure tilting stability in the radial bearings.

4.4. Model I - Radial bearing with small inner ring

Figure 4.7 shows one of the proposals for the radial passive magnetic bearings. In this version, the ring diameters are small. Air gap length is 0.5mm, same as the motor. The inner bearing ring is aligned with the rotor permanent magnets, keeping a high $\frac{d_z}{d_y}$ ratio. Radial, axial and tilting stiffness will be evaluated for different values of height *h*.

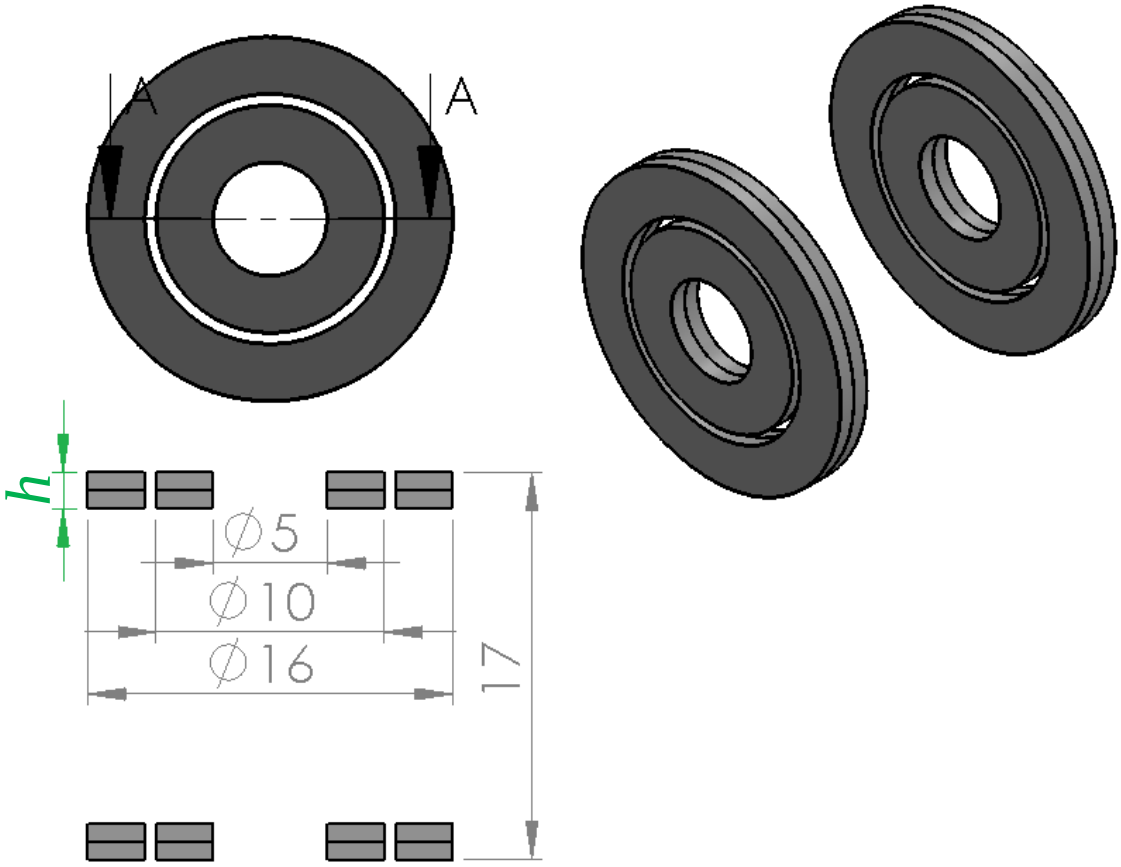

Figure 4.7 Passive bearing with narrow rings

4.4.1. Model I - Radial stiffness

Four different versions of model I were modeled by varying height h from 1.6mm to 2.8mm. Figure 4.8 and Figure 4.9 show respectively the radial forces caused by displacement along the *x*-axis and radial stiffness for each height of PB model I. When the passive bearing height is increased, also increase the stable repulsive forces.

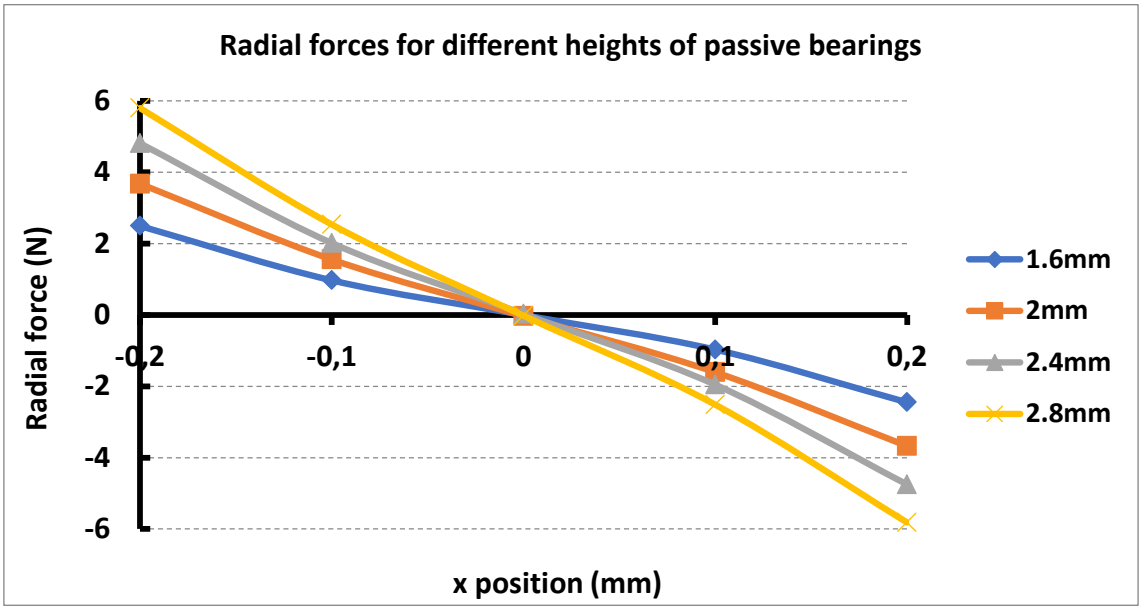

Figure 4.8 Radial forces over the inner ring of the passive bearing for displacements between x=-0.2mm and x=0.2mm

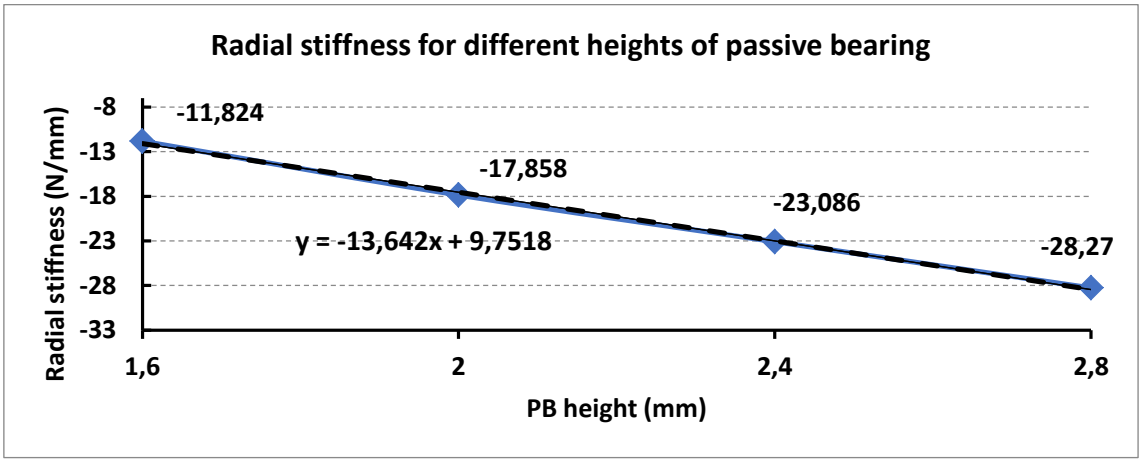

Figure 4.9 Radial stiffness results for model I. Heights ranging from 1.6mm to 2.8mm

4.4.2. Model I - Axial stiffness

Figure 4.10 and Figure 4.11 show, respectively, axial forces due to displacement of the inner ring of the passive bearing and axial stiffness for each height of passive bearing tested. When the passive bearing height is increased, unstable axial forces also increase and axial force variation is approximately twice the increase of stable radial forces.

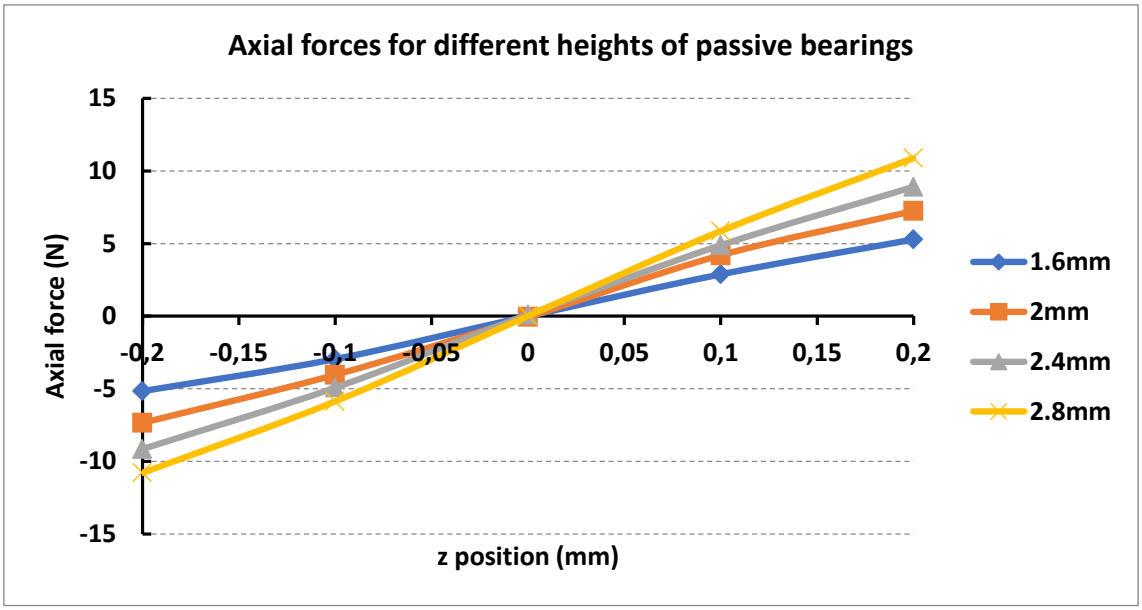

Figure 4.10 Axial forces over the inner ring of the passive bearing for displacements between z=-0.2mm and z=0.2mm

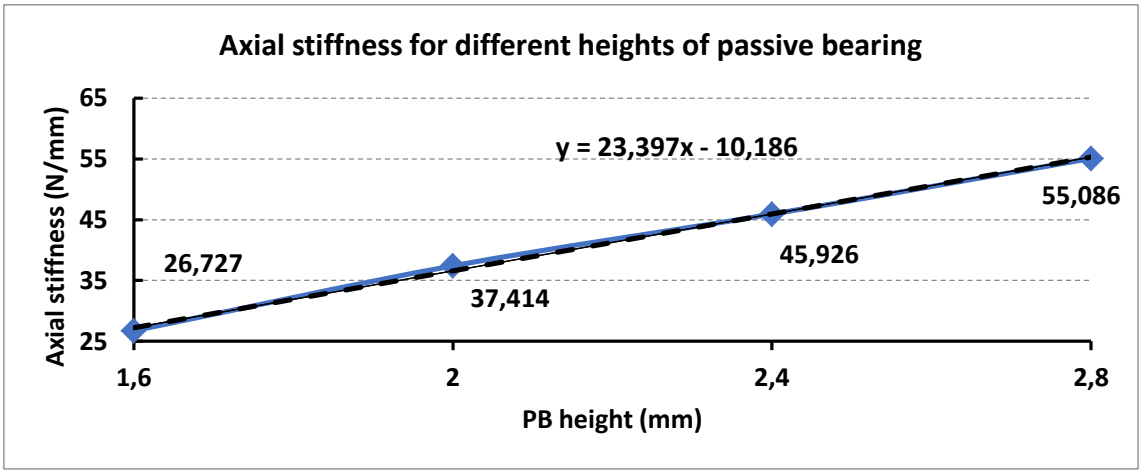

Figure 4.11 Axial stiffness results for model I. Heights ranging from 1.6mm to 2.8mm

4.4.3. Model I - Tilting stiffness

Tilting torques around *x* axis are always stable in the displacement range considered for this model. Tilting torques and tilting stiffness are shown in Figure 4.12 and Figure 4.13. The tilting torque variation when changing the height of passive bearings can be approximated by a second-degree function.

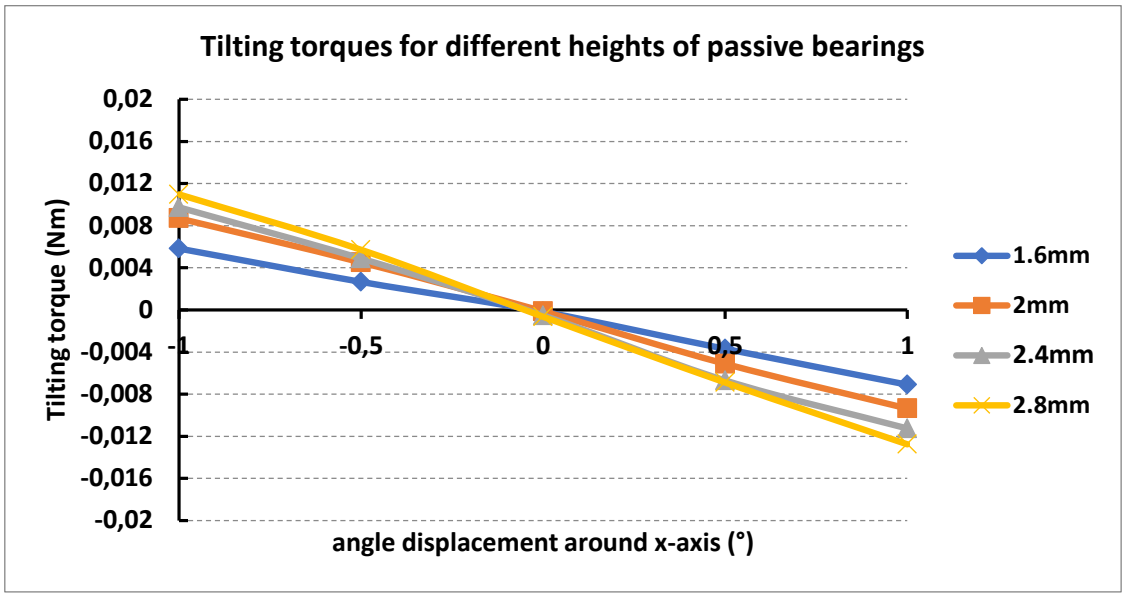

Figure 4.12 Tilting torques over the inner ring of the passive bearing for angular displacements between -1° and 1°

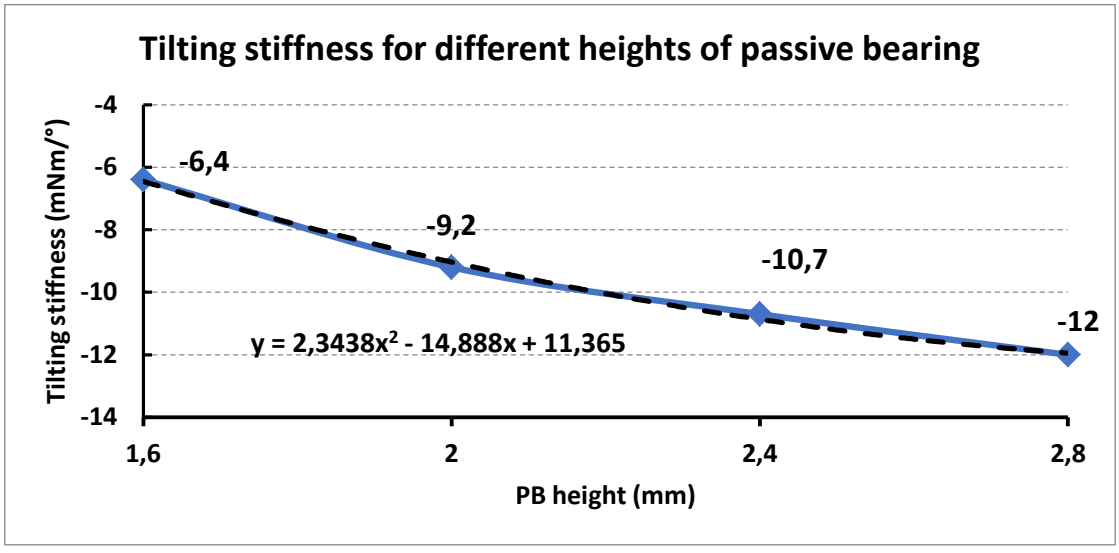

Figure 4.13 Tilting stiffness results for model I. Heights ranging from 1.6mm to 2.8mm

4.5. Model II - Radial bearing with medium inner ring

Model II was adapted from model I. The diameter of the inner ring is bigger than that of model I. Air gap length is 0.5mm, same as model I. It is expected that overall higher radial and axial stiffness may be obtained at the expense of a decrease in the $\frac{d_z}{d_y}$ ratio and consequently less tilting stability. Figure 4.14 shows the 3D model for the proposed model II.

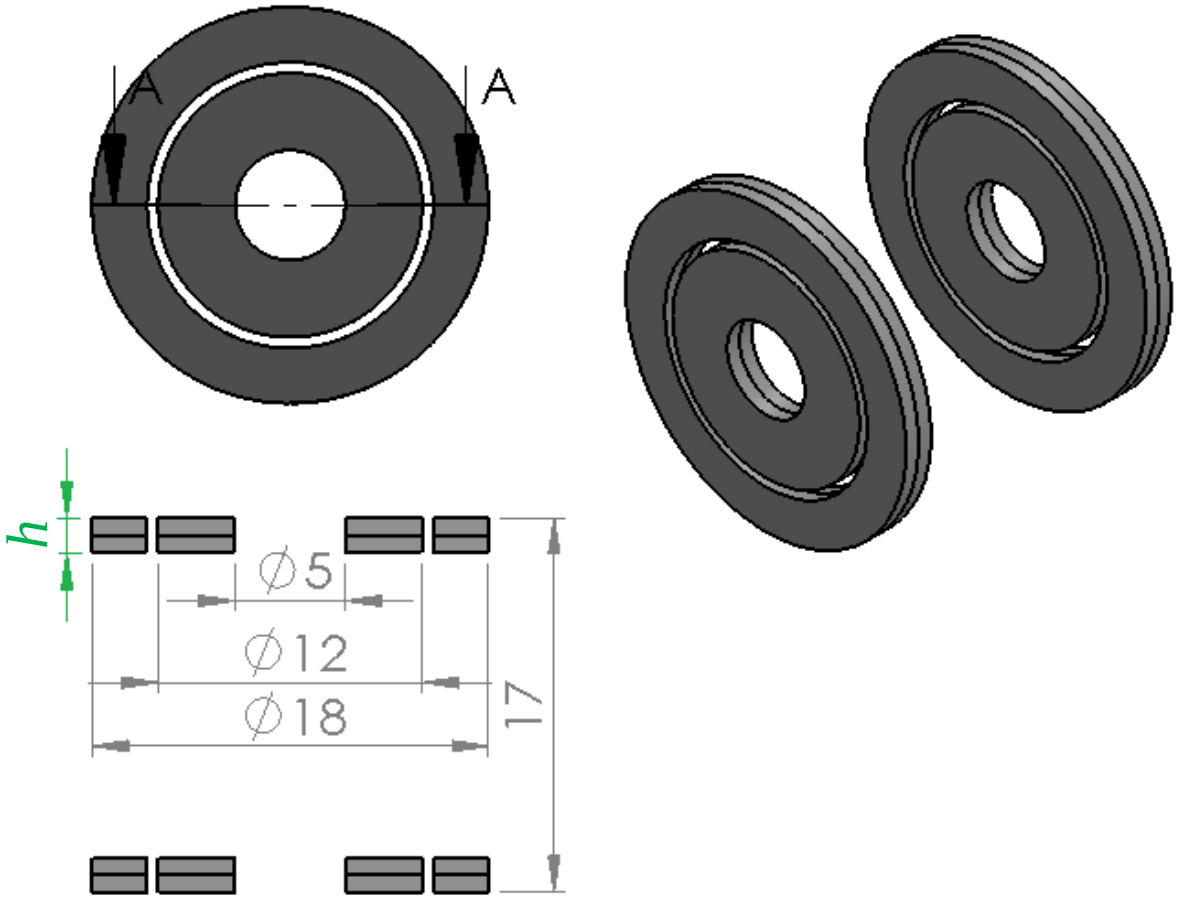

Figure 4.14 – Passive bearing model II

4.5.1. Model II - Radial stiffness

Radial forces and radial stiffness values are shown in Figure 4.15 and Figure 4.16. As expected there was an increase in radial forces, since air gap area was increased.

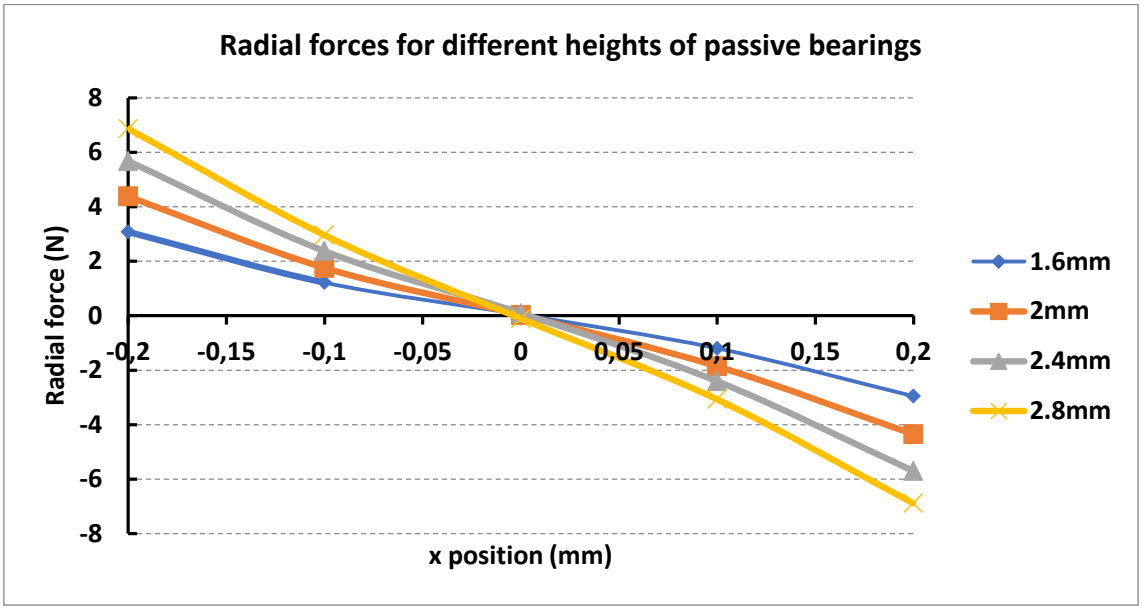

Figure 4.15 Radial forces over the inner ring of the passive bearing for displacements between x=-0.2mm and x=0.2mm

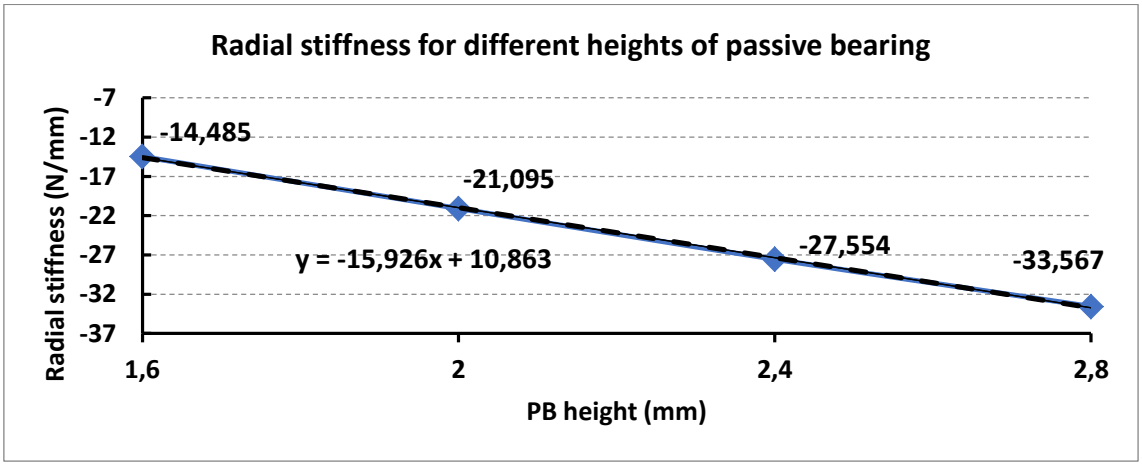

Figure 4.16 Radial stiffness results for model II. Heights ranging from 1.6mm to 2.8mm

4.5.2. Model II - Axial stiffness

Axial stiffness was also considerably increased. Variation in axial forces are also twice the variation of radial forces. Calculated axial values and stiffness are shown in Figure 4.17 and Figure 4.18.

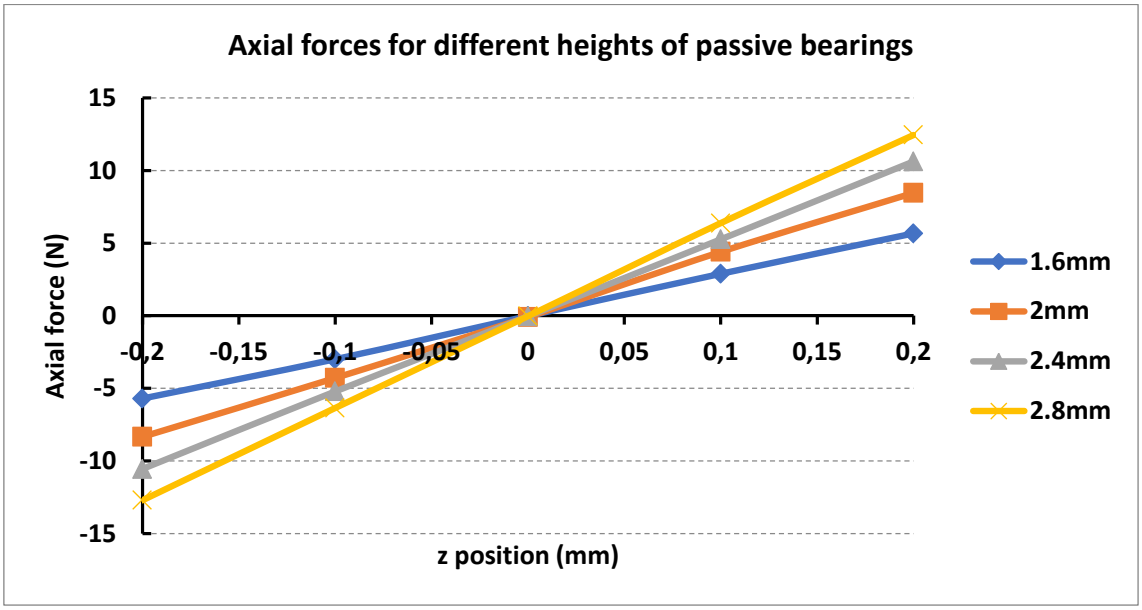

Figure 4.17 Axial forces over the inner ring of the passive bearing for displacements between z=-0.2mm and z=0.2mm

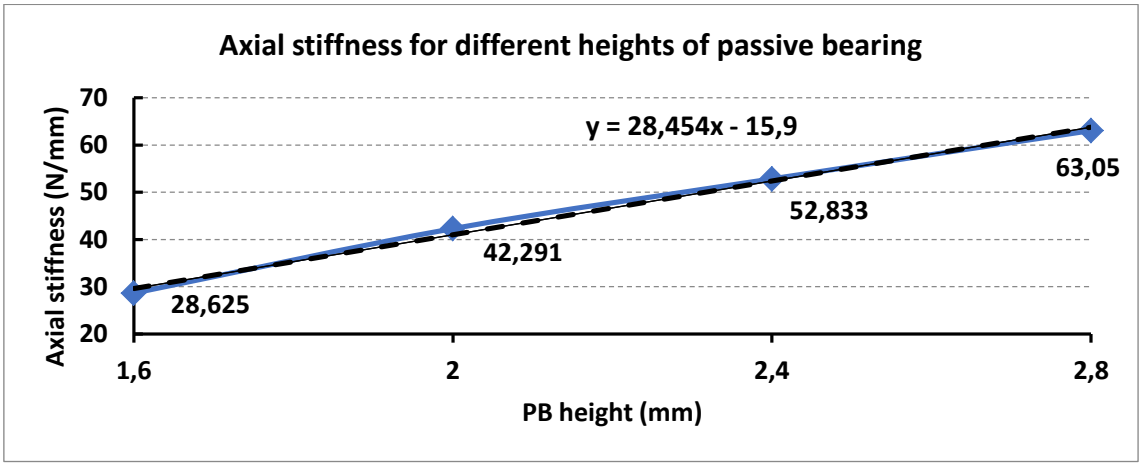

Figure 4.18 Axial stiffness results for model II. Heights ranging from 1.6mm to 2.8mm

4.5.3. Model II - Tilting stiffness

Figure 4.19 and Figure 4.20 show respectively, tilting torques and tilting stiffness. Model II has less stable torques than model I. The most stable torques are achieved at *h*=2.4mm.

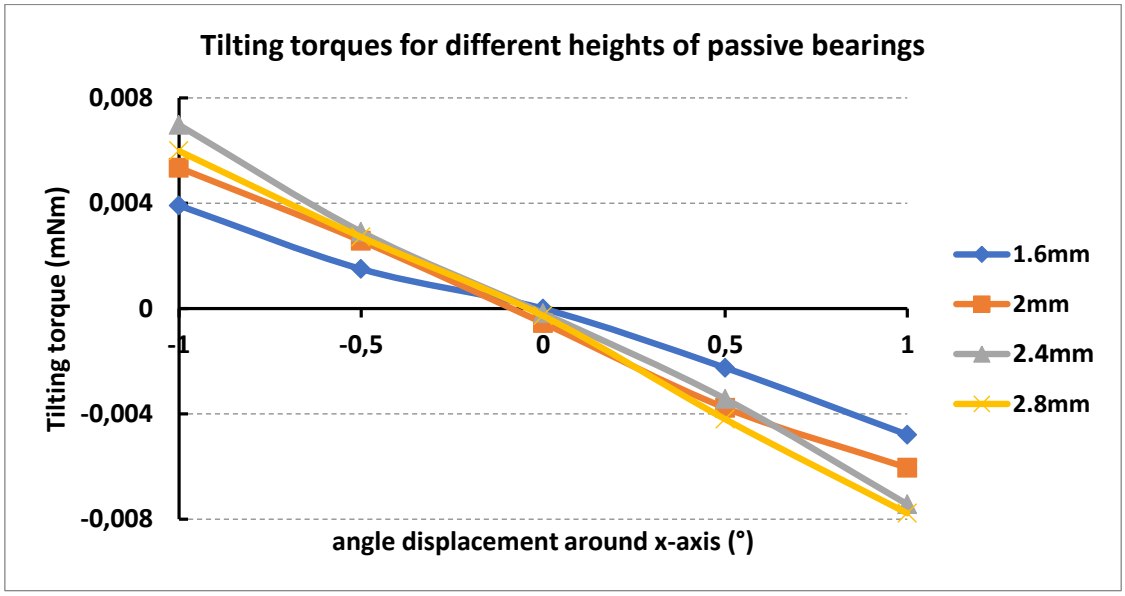

Figure 4.19 Tilting torques over the inner ring of the passive bearing for angular displacements between -1° and 1°

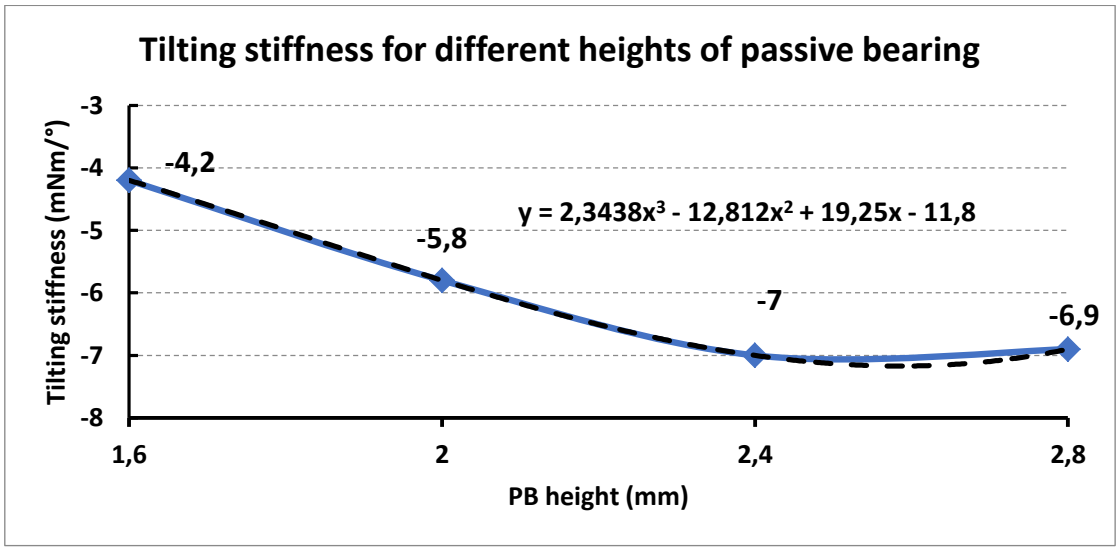

Figure 4.20 Tilting stiffness results for model II. Heights ranging from 1.6mm to 2.8mm

4.6. Model III - Radial bearing with large inner ring

Model III has larger air gap diameter. Following the results from Model II, it is expected that radial stiffness will be higher and tilting torques will be less stable. The 3D model is shown in Figure 4.21.

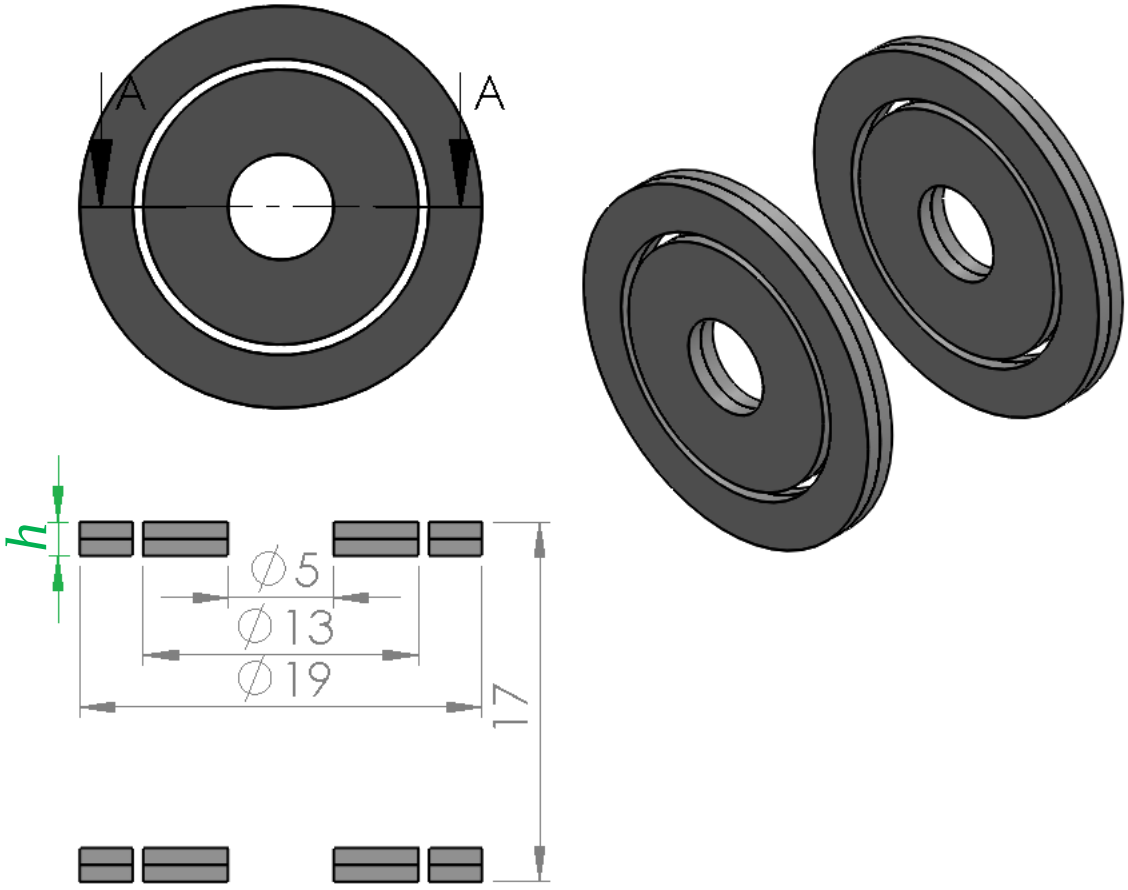

Figure 4.21 Passive bearings model III

4.6.1. Model III - Radial stiffness

Radial stiffness was increased if compared to models A and B. Calculated radial forces and radial stiffness are shown in Figure 4.22 and Figure 4.23.

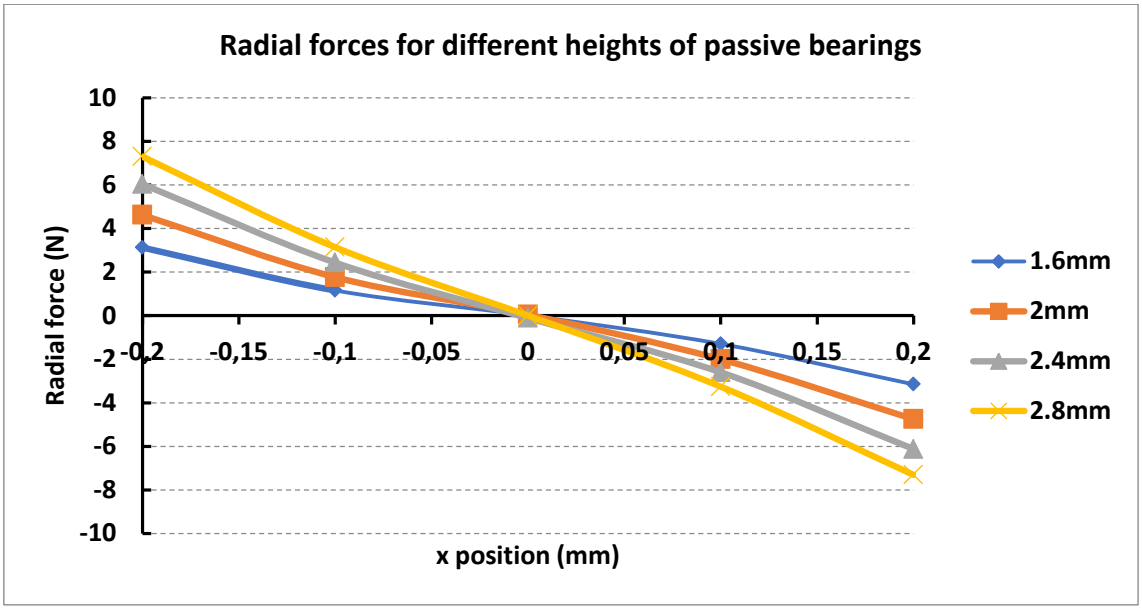

Figure 4.22 Radial forces over the inner ring of the passive bearing for displacements between x=-0.2mm and x=0.2mm

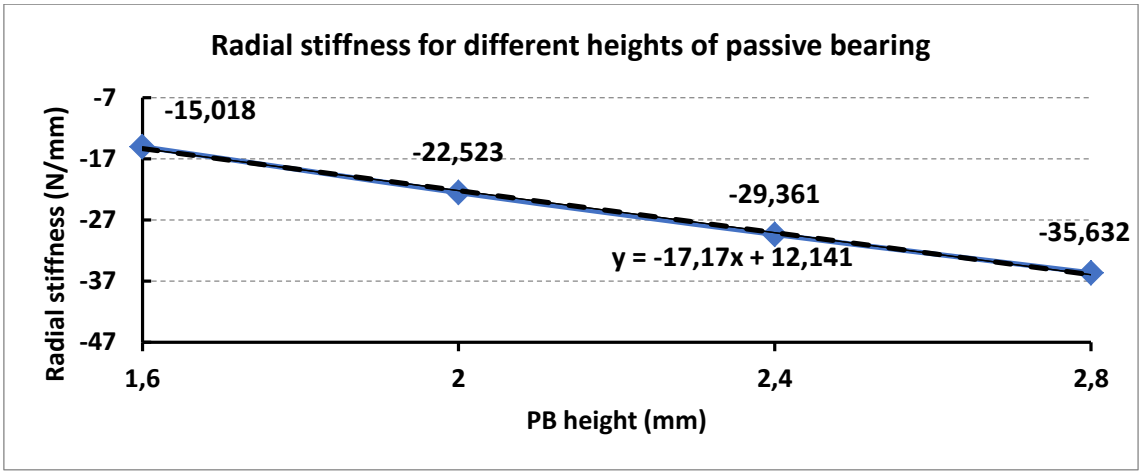

Figure 4.23 Radial stiffness results for model III. Heights ranging from 1.6mm to 2.8mm

4.6.2. Model III - Axial stiffness

Figure 4.24 and Figure 4.25 show calculated axial forces and axial stiffness, respectively, for model III passive bearing.

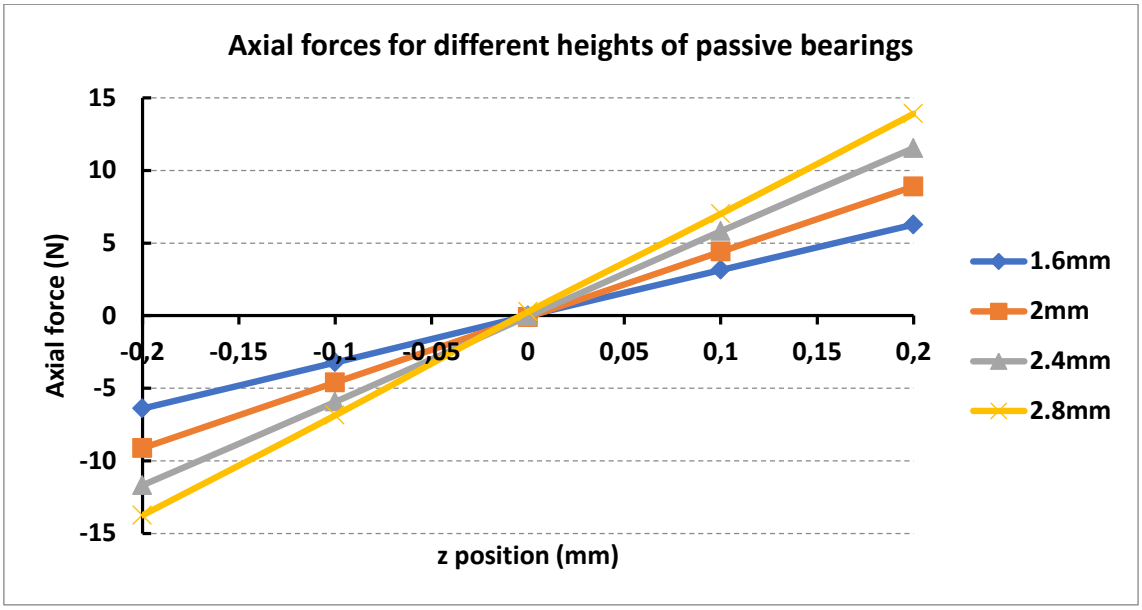

Figure 4.24 Axial forces over the inner ring of the passive bearing for displacements between z=-0.2mm and z=0.2mm

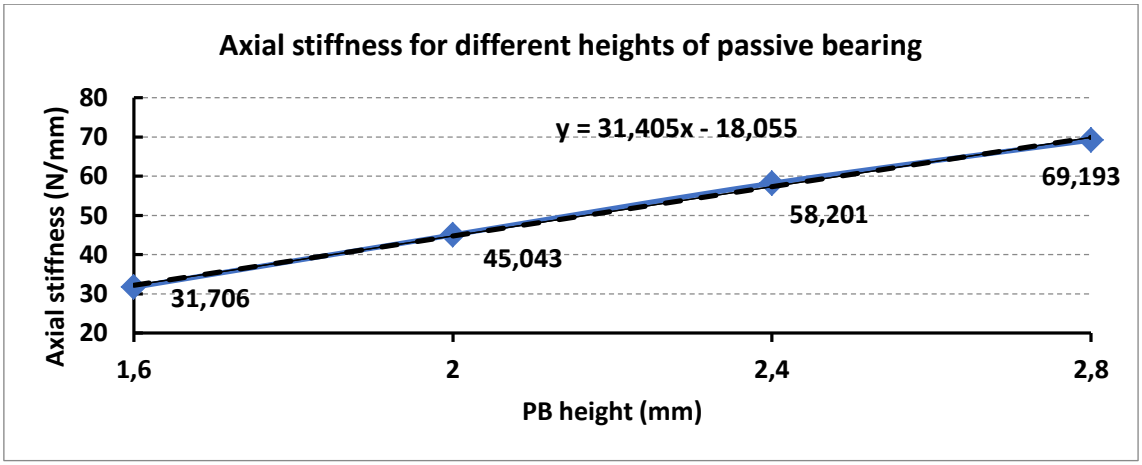

Figure 4.25 Axial stiffness results for model III. Heights ranging from 1.6mm to 2.8mm

4.6.3. Model III - Tilting stiffness

Figure 4.26 and Figure 4.27 show torque values and tilting stiffness for passive bearings of model III with different heights. In Figure 4.26 we see that calculated torque characteristics do not have a symmetrical behavior. This may result in displacement of the motor's rotation axis, but since the bearing is completely symmetric, it is also highly likely that this was caused by numerical deviation when it gets near to instability.

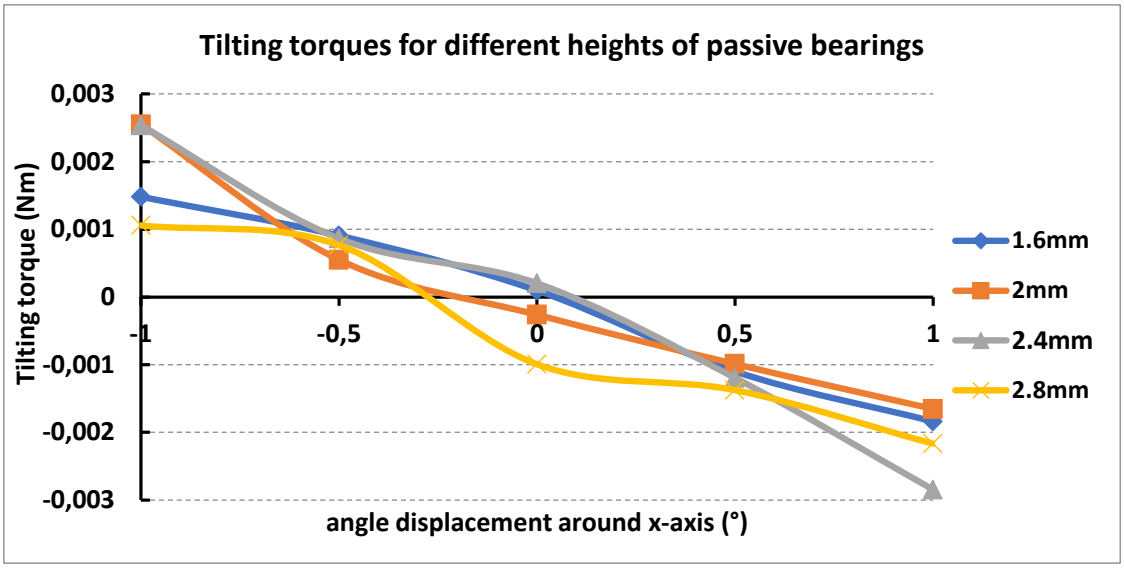

Figure 4.26 Tilting torques over the inner ring of the passive bearing for angular displacements between -1° and 1°

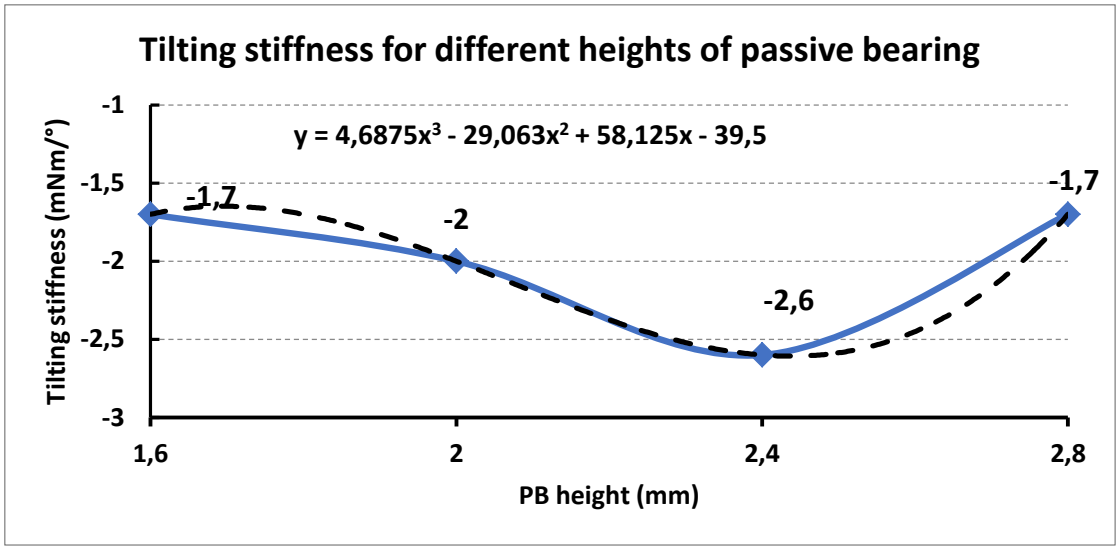

Figure 4.27 Tilting stiffness results for model III. Heights ranging from 1.6mm to 2.8mm

4.7. Comparison between passive bearing proposals

This section provides a comparison between the three proposed passive bearing structures. Figure 4.28, Figure 4.29 and Figure 4.30 show respectively the radial stiffness, the axial stiffness and the tilting stiffness for all models. The passive bearing's axial stiffness is always approximately twice the radial stiffness.

Model III has the highest value of radial stiffness, but its tilting stiffness is not reliable. The highest radial stiffness achievable using the models proposed are those from model III. Axial stiffness follows the same tendency as the radial stiffness.

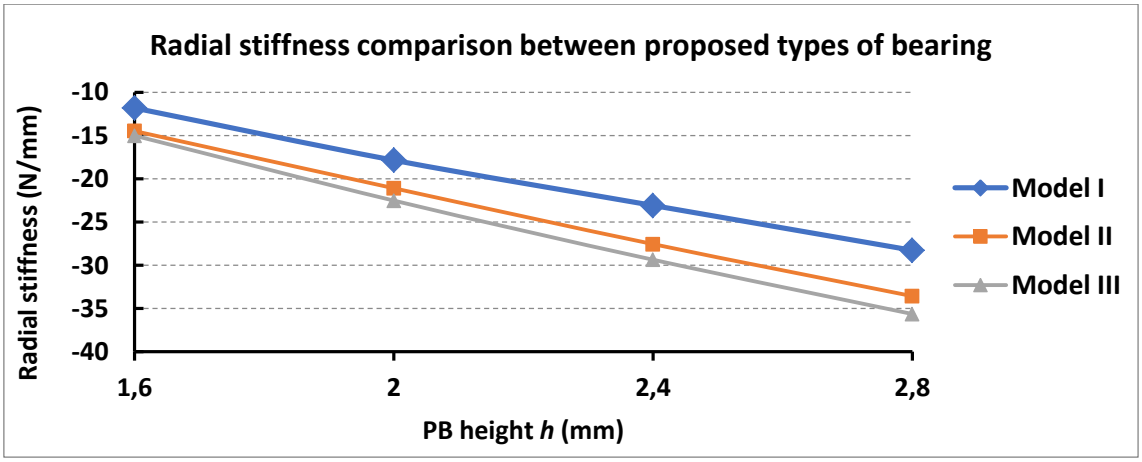

Figure 4.28 Radial stiffness comparison between the three proposed models

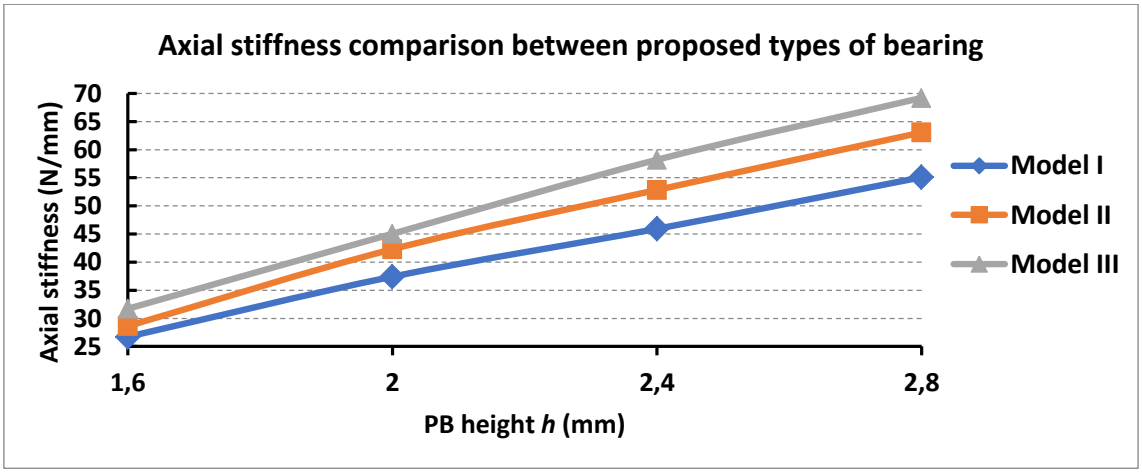

Figure 4.29 Axial stiffness comparison between the three proposed models

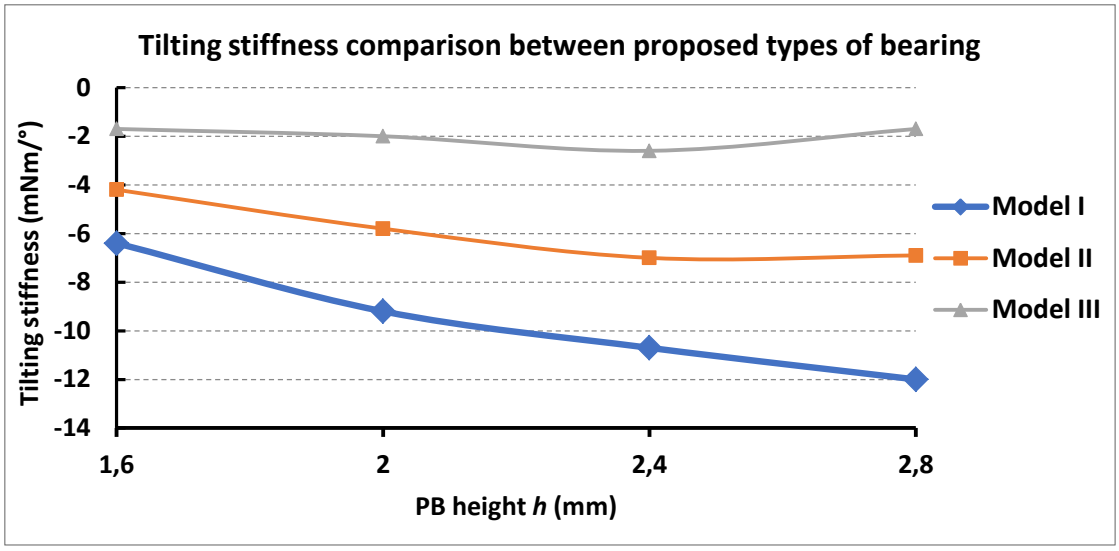

Figure 4.30 Tilting stiffness comparison for the three proposed models

Considering that Model III has lower tilting stiffness than the other two, it is better to choose Model II when aiming at high radial stability without compromising tilting stability.

5.Final version of the proposed model

This chapter describes the final models proposed for the single drive axially controlled bearingless motor. The final version of the model was adapted from the seventh version by increasing the vertical section of stator slot area for accommodating coils with a higher number of turns to increase torque value. The upper and lower stator layers were reduced to optimize flux density distribution and the middle layer was increased to reduce saturation when high currents are required for regulating the axial position. The number of turns per coil was increased from 20 to 25 and stator height rose to 11mm. A comparison between the seventh version and the final version are shown in Figure 5.1.

The stack length, considering passive bearings, is set as a design specification. The stator size imposes a limitation on the bearing size, reducing the options for radial stabilization. It is necessary to find a balance between stable radial stiffness and adjustment of motor parameters.

As a safety measure, a clearance should be provided between the stator and the passive bearings to avoid interference in the tilting torques by attraction forces between the stator and the permanent magnets. Setting a clearance of 0.5mm, and an addition margin of 0.1mm for axial touchdown position, the passive bearing height becomes limited to 2.4mm.

Keeping the stator exactly the same, two different types of rotor were proposed, like shown in Figure 5.2. The first one, type A, has segmented magnets with parallel polarization. The second one, type B, has ring-shaped magnets with polar anisotropic polarization. Type B is easier to assemble than type A, since it does not require a rotor case like the one shown in Figure 2.4, but it is not easily fabricated like type A.

This chapter makes comparisons between models with the two rotor types, by analyzing their torque performance and magnetic forces.

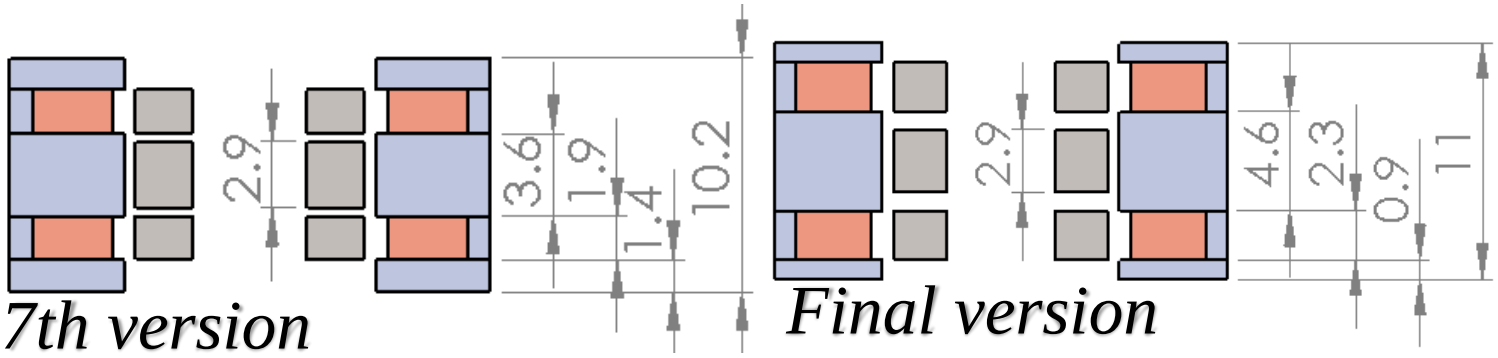

Figure 5.1 Comparison between the seventh version and the final version

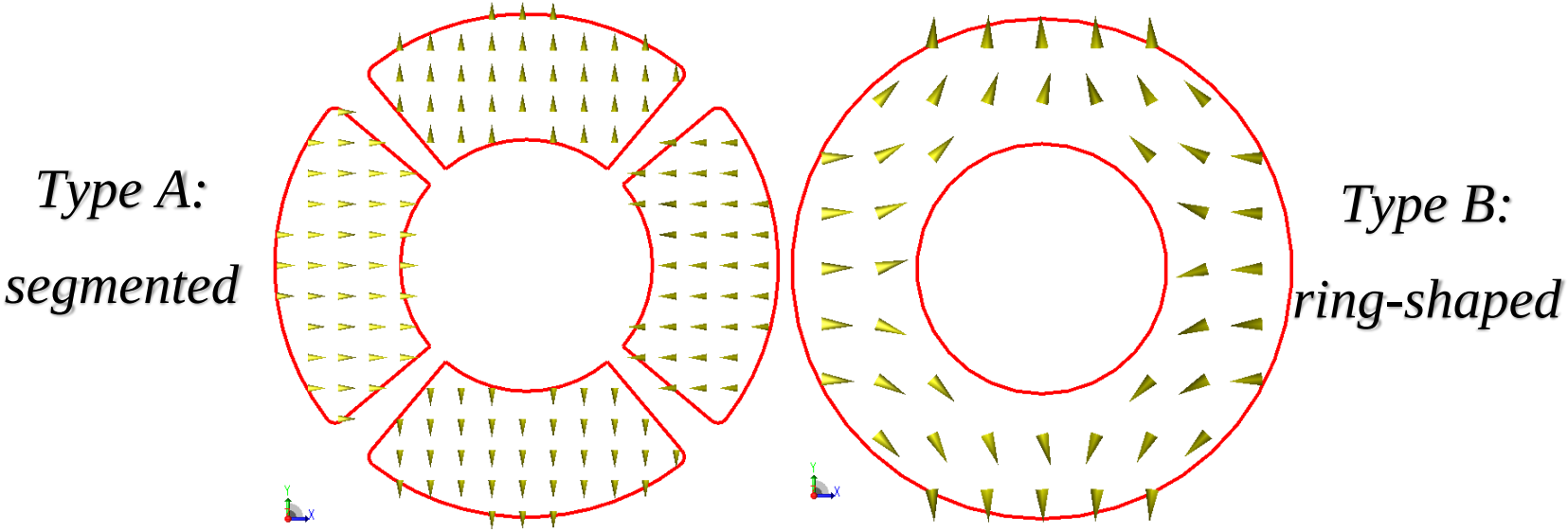

Figure 5.2 To the left: rotor layers type A, segmented magnet. To the right: rotor layers type B, ring shaped.

5.1. Torque analysis

Figure 5.3 show torque results for the FEA of the final model for types A and B. Torques were calculated using a 0.3mm limit for face element size. The stator coils were fed by a three phase AC current source with 1A RMS, keeping the 8A/mm² current density. Average torque and ripple are described in Table 5.1.

Table 5.1 Torque results for the final model

	Type A	Type B
Average torque	2.44mNm	2.96mNm
Torque ripple	40.8%	36.8%
Torque density	0.414Nm/ℓ	0.503Nm/ℓ

As seen in Table 5.1, substituting the segmented rotor (type A) for a ring-shaped rotor (type B) with same size increases the average torque. Considering average torque value or torque density, type B is the best option.

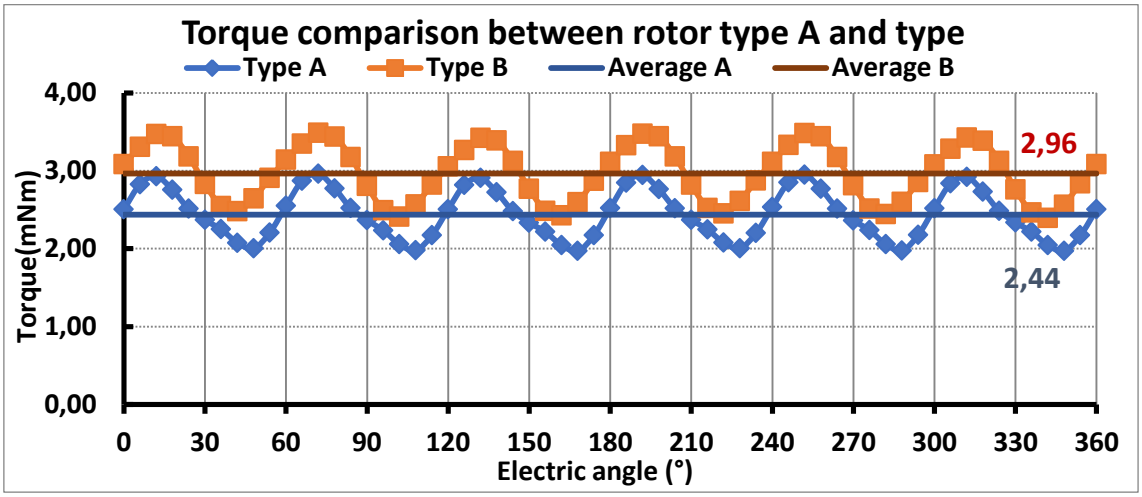

Figure 5.3 Torque results obtained through FEA for the less detailed face mesh

5.2. Efficiency analysis

Figure 5.4 shows results as calculated by the FEA for output power, iron losses, copper losses and efficiency for type A and type B, for both kinds of meshes.

Efficiency calculated for type A is 77.74% and for type B is 79.36% at 18000rpm. SUGIMOTO et al.[14] made a comparison between a bearingless motor and a motor with ball bearings. Both achieved efficiency close to 84% at 7200rpm, higher values than the ones obtained in this work.

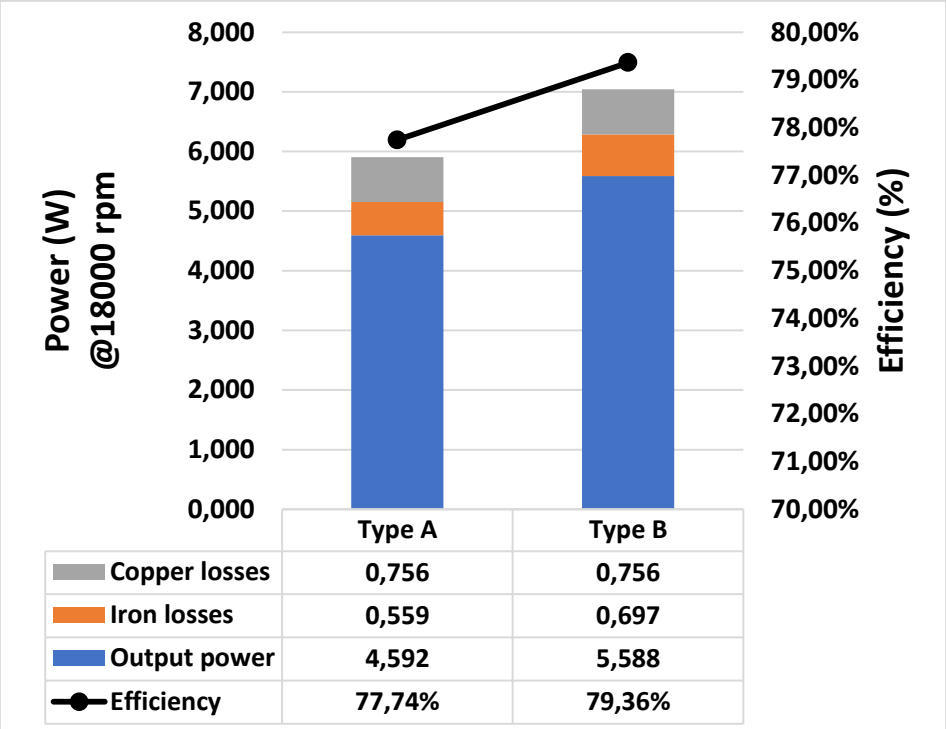

Figure 5.4 Power and losses calculated by FEA

5.3. Back-electromotive force (Back-EMF) analysis

Setting the source current to 0A, back-electromotive force at 18000rpm was calculated by FEA. Back-EMF values are shown in Figure 5.5 for rotor type A and in Figure 5.6 for rotor type B. The Fast Fourier Transform of back-EMF is shown in Figure 5.7 for type A and in Figure 5.8 for type B.

Maximum peak back-EMF values are around 2.5V. The influence of harmonic components is visible in Figure 5.5, due to a flattening near the peak values. As shown in Figure 5.7, this effect is caused by fifth and seventh order harmonics. Since the magnitude of both components are around 0.03V, it is difficult to see them in the plot. On the other hand, the fifth order harmonic in type B is approximately ten times larger than the one in type A, while the seventh order harmonic has twice the magnitude of type A.

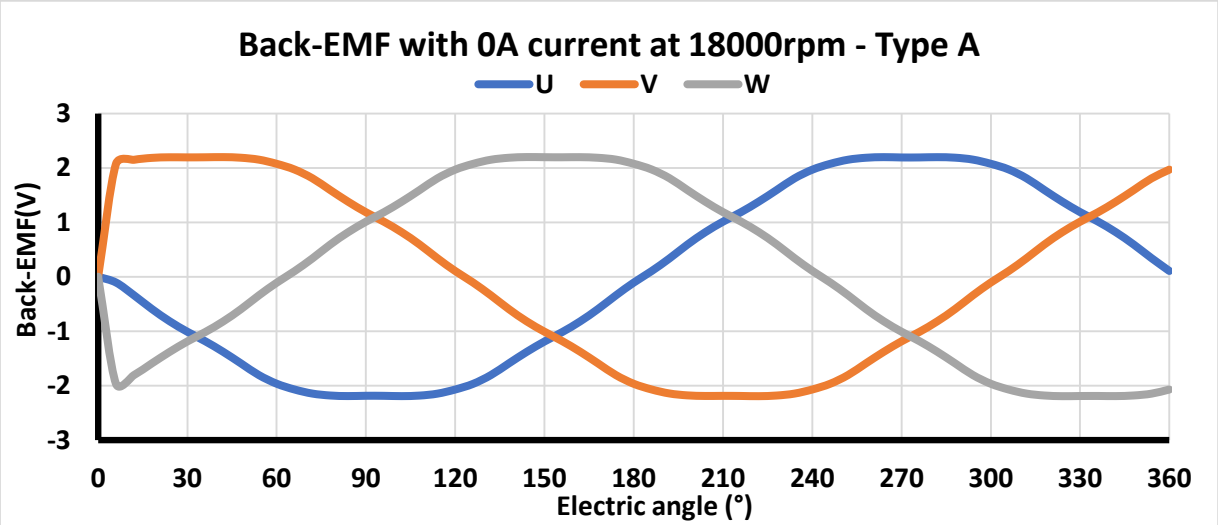

Figure 5.5 Back-EMF values for type A

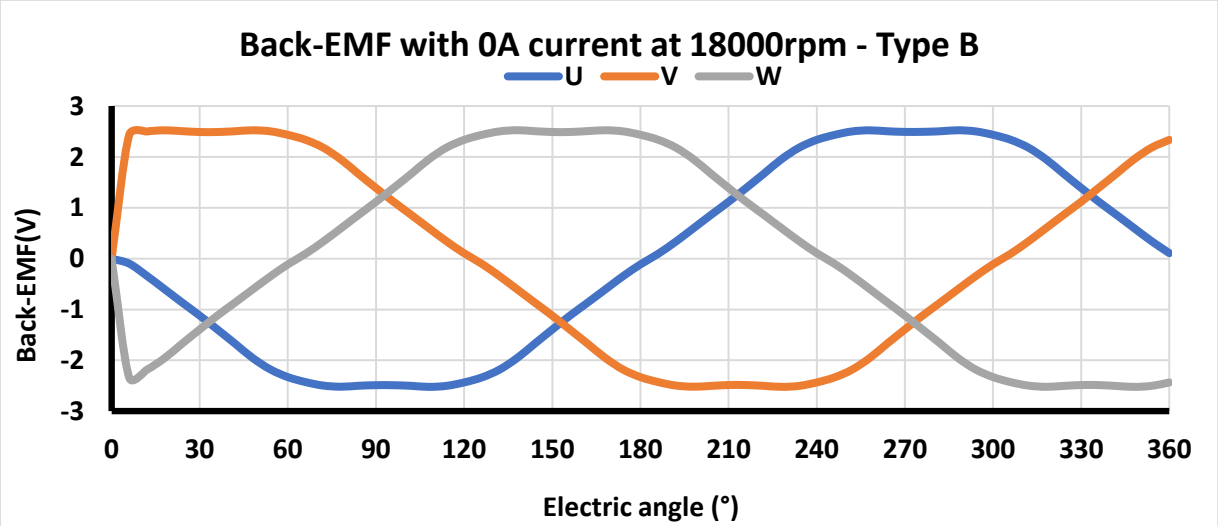

Figure 5.6 Back-EMF values for type B

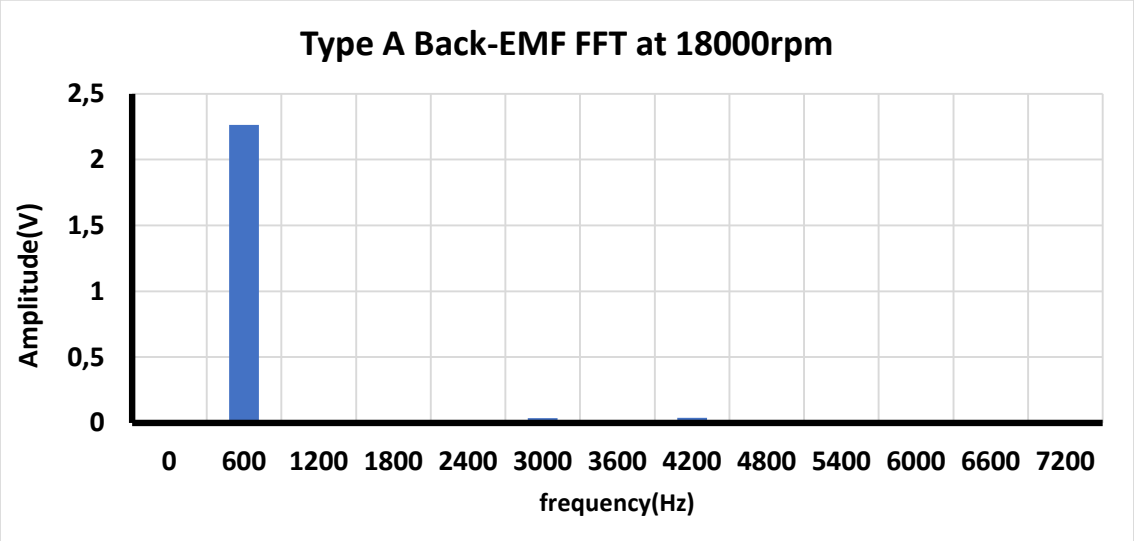

Figure 5.7 FFT of back-EMF signal for type A

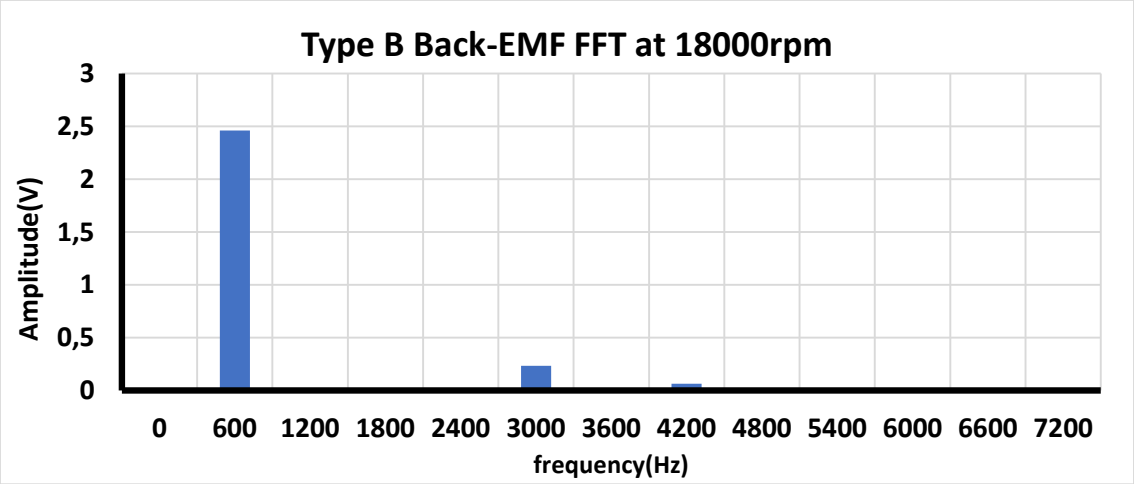

Figure 5.8 FFT of back-EMF signal for type B

5.4. Unstable forces and passive bearings dimensioning

This section presents an analysis of radial forces in the motor for types A and B. It shows calculations for the radial stiffness, centering index, unstable axial forces and current required for lifting the rotor from axial touchdown position.

5.4.1. Rotor radial stiffness

Figure 5.9 shows the magnitude of radial force acting on the rotor for displacements between -0.2mm and 0.2mm. By first degree fitting, we find the rotor radial stiffness, K_{rr}, 12.70N/mm for type A and 16.25N/mm for type B. Radial stiffness on type B is slightly higher.

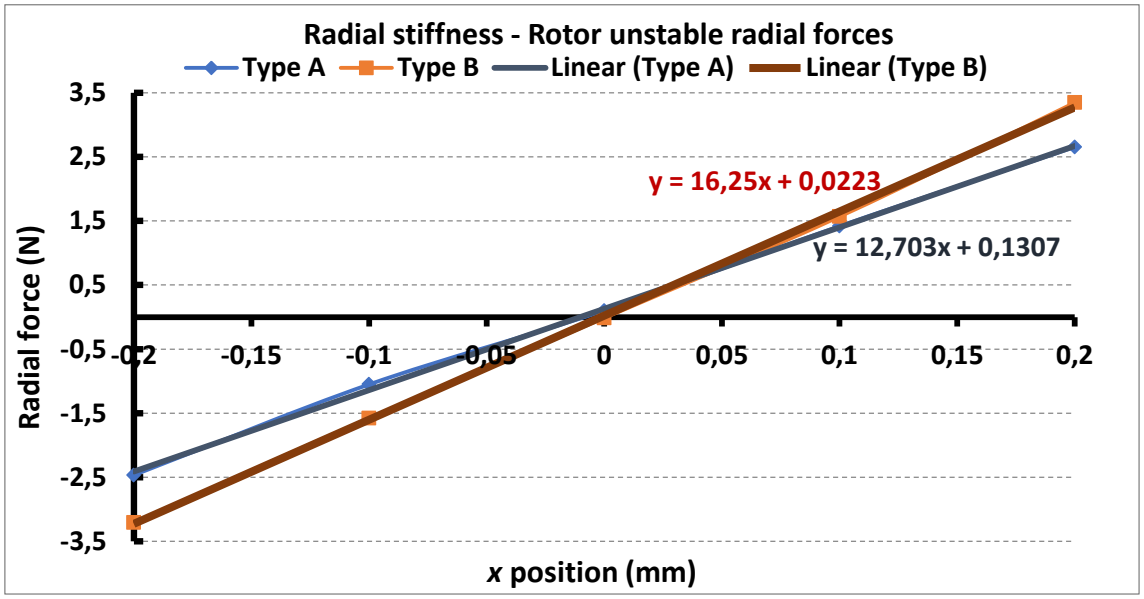

Figure 5.9 Unstable radial forces for both rotor types

5.4.2. Centering index calculation

In Chapter 4, repulsive forces on passive bearings were analyzed. Now it is possible to estimate resultant radial stiffness and centering index for the motor. Using a 3D modeling software, we estimate the rotor mass will be less than 16g. A limit height of 2.4mm was set to the passive bearings, so we set a height *h*=2.4mm, because it has the maximum possible radial stiffness.

Passive bearing model III was discarded due to its poor performance on tilting stabilization. Resultant radial stiffness and centering index are calculated by combining rotor types A and B with radial bearings I and II. Results are shown in Table 5.2:

Table 5.2 Maximum and minimum resultant radial stiffness and centering index

	Type A		Type B	
	Bearing I	Bearing II	Bearing I	Bearing II
Radial stiffness	-10.38N/mm	-14.85N/mm	-6.84N/mm	-11.30N/mm
Centering index	33.08	47.31	21.78	36.01

Both resultant radial stiffness and centering index depend on the chosen passive bearing. As said before, increasing the radial stiffness implies the need for higher currents to compensate unstable axial forces, so not necessarily the highest centering index is the best solution. It depends on operational limitations. There is also a tradeoff between torque density and centering index in this case. Type A has the highest radial stability while type B has the lowest radial stability.

5.4.3. Tilting analysis

Tilting torques for angular rotor displacements ranging from -1° to 1° are shown in Figure 5.10. The resultant tilting torque is given by the sum of rotor tilting torques and passive bearing tilting torques. Resultant tilting torques for the considered options of magnetic bearing are shown in Figure 5.11 and Figure 5.12.

The type of rotor does not affect greatly the tilting torques, since stable torques are in a higher order.

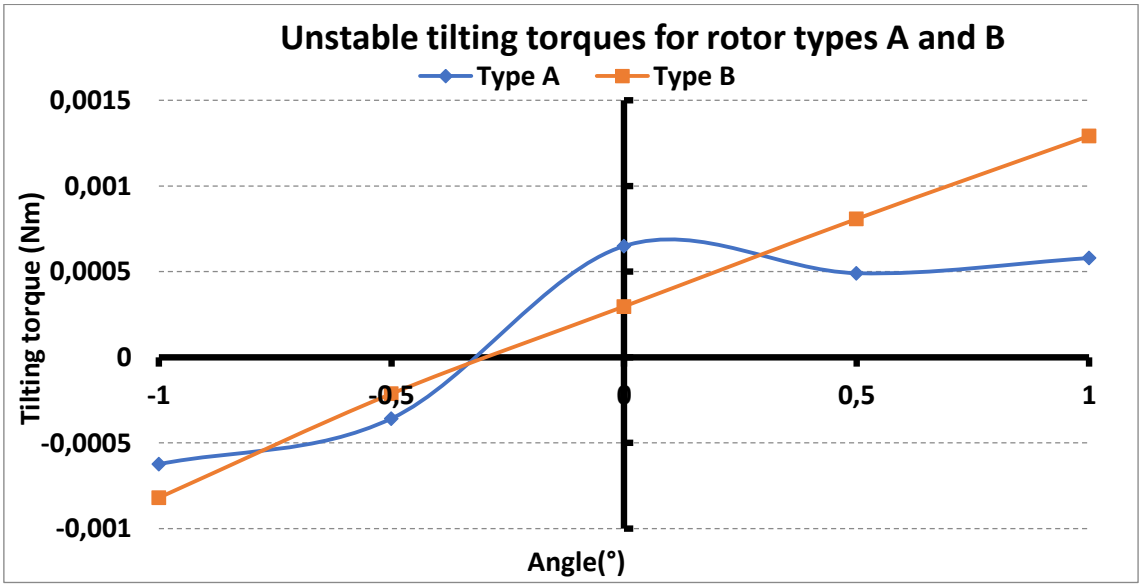

Figure 5.10 Rotor tilting torques around x-axis

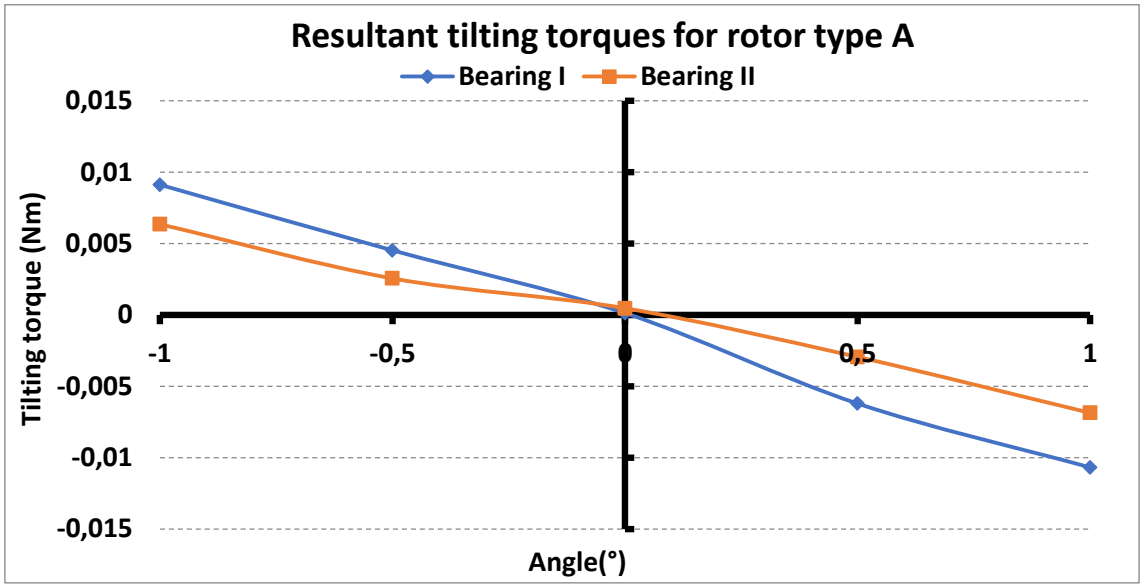

Figure 5.11 Resultant torques for rotor type A combined with both bearing types

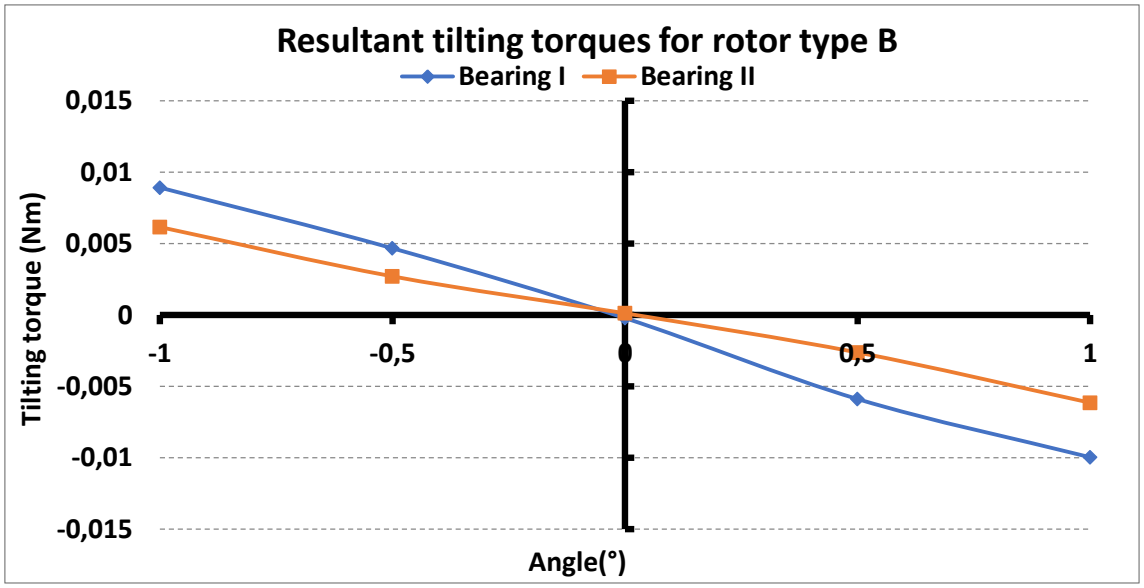

Figure 5.12 - Resultant torques for rotor type B combined with both bearing types

5.4.4. Unstable axial forces

This section explains the calculations of the unstable axial forces.

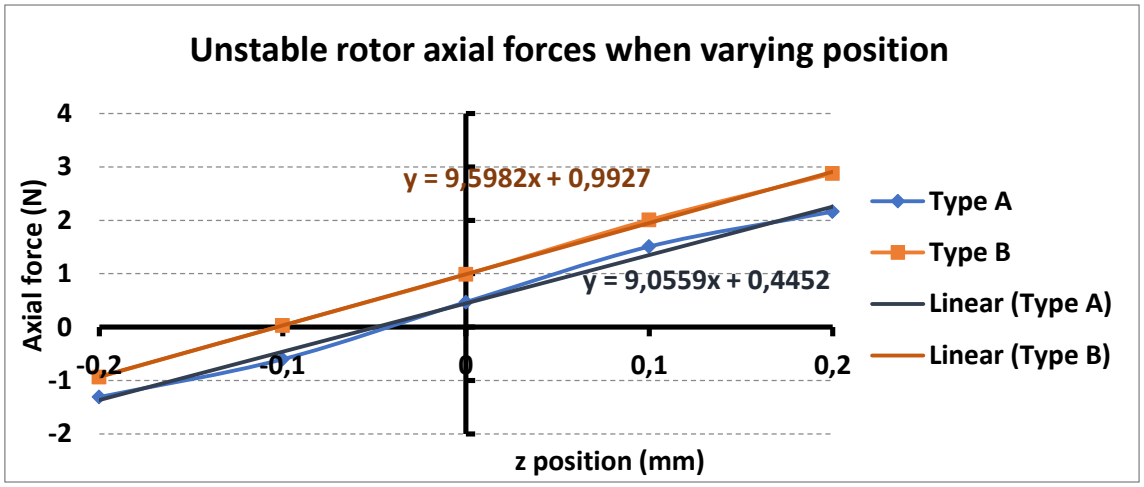

Figure 5.13 shows forces on rotor types A and B when displacing the rotor along the *z*-axis from position *z*=-0.2mm to *z*=0.2mm. At position *z*=0, offset axial forces are 0.67N for rotor type A and 0.45N for rotor type B. By slightly adjusting the passive bearings axial position, also considering the rotor weight, it is possible to adjust the axial force at central position to 0N, removing the force offset.

Figure 5.14 and Figure 5.15 show resultant axial forces (with offset force compensated) when rotor types are combined with both passive bearings.

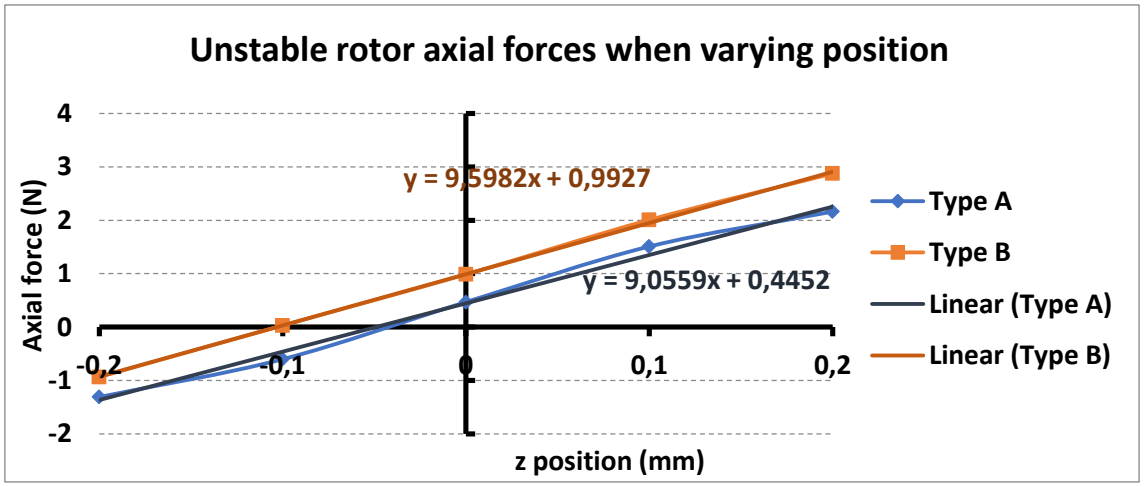

Figure 5.13 Axial forces due to displacement of the rotor in the final version

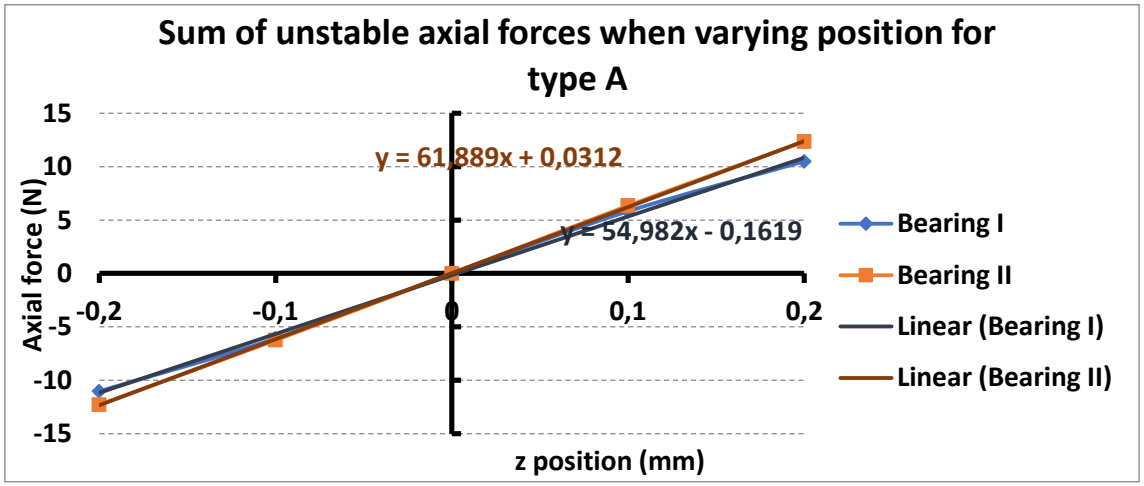

Figure 5.14 Resultant axial forces for rotor type A combined with both bearing models. Bearing height is 2.4mm

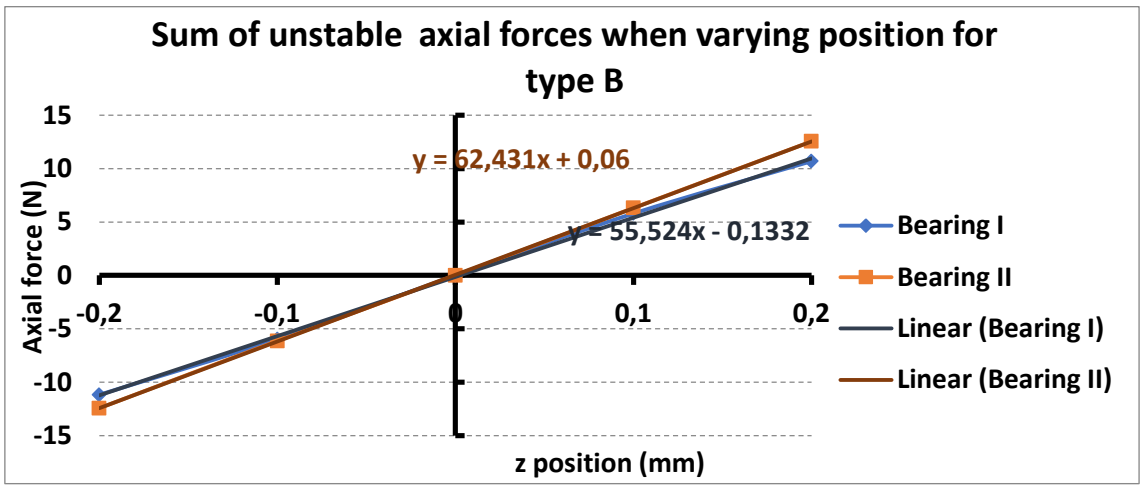

Figure 5.15 Resultant axial forces for rotor type B combined with all bearing models. Bearing height is 2.4mm

5.4.5. Active compensation of unstable axial forces

Unstable axial forces are actively compensated by I_d current components, like explained in item 2.5. Stabilizing axial force is limited by two factors: current conduction capacity and stator core saturation.

Figure 5.16 shows axial force on the rotor with I_d current components ranging from -25A to 25A, while keeping the rotor in the central position. There is a clear asymmetry in the rotor axial forces in the central position due to the intrinsic offset

force generated by the rotor permanent magnets. By subtracting the force offset, we obtain the actual current-induced forces like seen in Figure 5.17.

It is important to notice that for currents above 15A the core starts to saturate and the force-current factor decreases, while for lowest currents, no saturation occurs. This asymmetry in the force-current curve is caused by the interaction of the permanent magnets. Figure 5.18, Figure 5.19, Figure 5.20 and Figure 5.21 show flux density analysis for the extreme conditions of $I_d = 25\text{A}$ and $I_d = -25A$.

From the current-induced force results we see that, for 0.2mm axial displacements, active control cannot be realized since unstable forces rise above force values at core saturation point. Therefore, we limit mechanically the axial displacement touchdown position to 0.1mm. Precision is critical during the construction of the motor, since even 0.1mm variations may cause huge force changes.

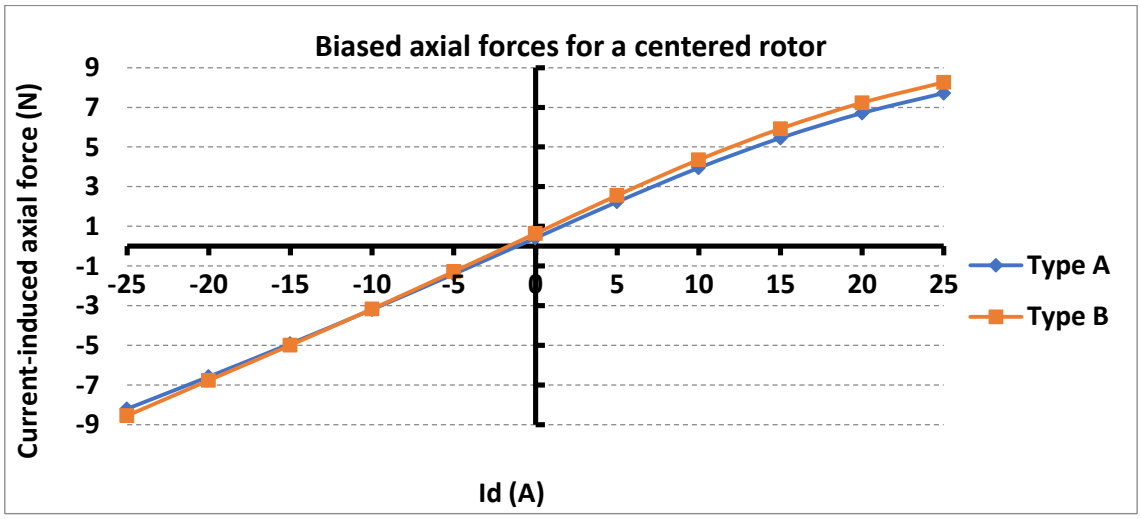

Figure 5.16 Total axial forces when currents are supplied and the rotor is centered

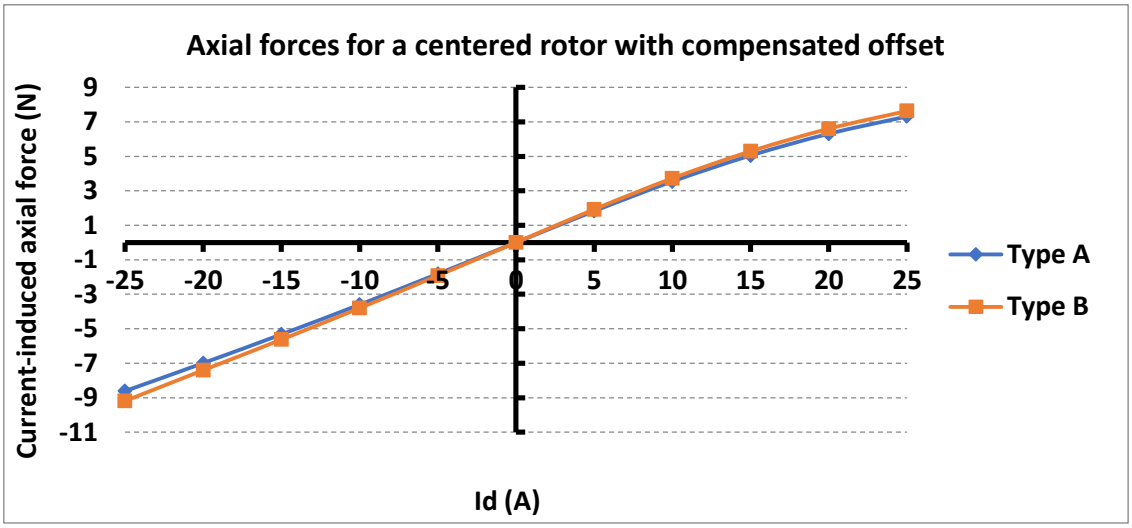

Figure 5.17 Current-induced forces over the rotor

Comparing data from current-induced forces and displacement induced axial forces, we see that for stabilizing the maximum axial forces, 20A currents may be required. This is close to 14 times the rated peak current. Table 5.3 shows the tradeoff between the required stabilizing current and the centering index. Using passive bearings that increase radial stiffness, and consequently the centering index, but increases the required current for lifting the rotor, since unstable axial forces also become bigger.

Table 5.3 Relation between axial forces, required currents for active compensation and centering index (CI)

	Type A				
	z=-0.1mm		z=0.1mm		
	Axial force	I_d current	Axial force	I_d current	CI
Bearing I	-6.10N	19A	5.66N	-17A	33.08
Bearing II	-6.25N	19A	6.62N	-20A	47.31
	Type B				
	z=-0.1mm		z=0.1mm		
	Axial force	I_d current	Axial force	I_d current	CI
Bearing I	-5.98N	18A	5.80N	-18A	21.78
Bearing II	-6.13N	19A	6.32N	-19A	36.01

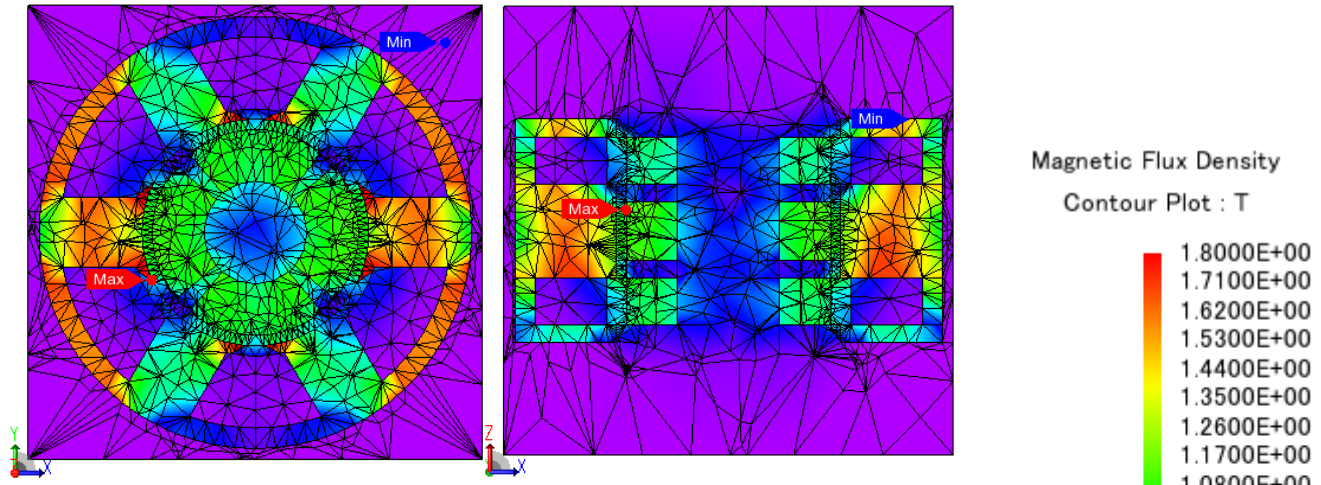

Figure 5.18 Flux density for $I_d = 25A$ on type A

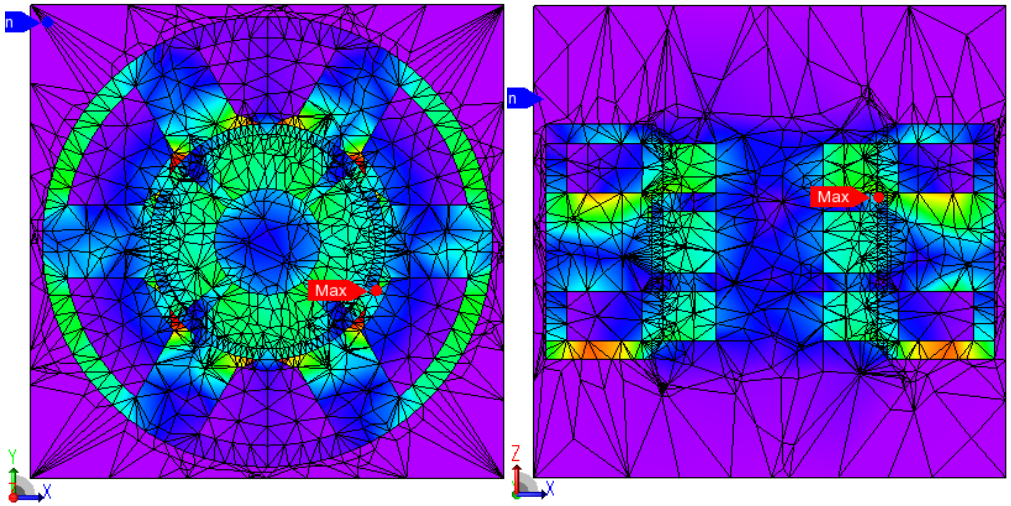

Figure 5.19 Flux density for $I_d = -25A$ on type

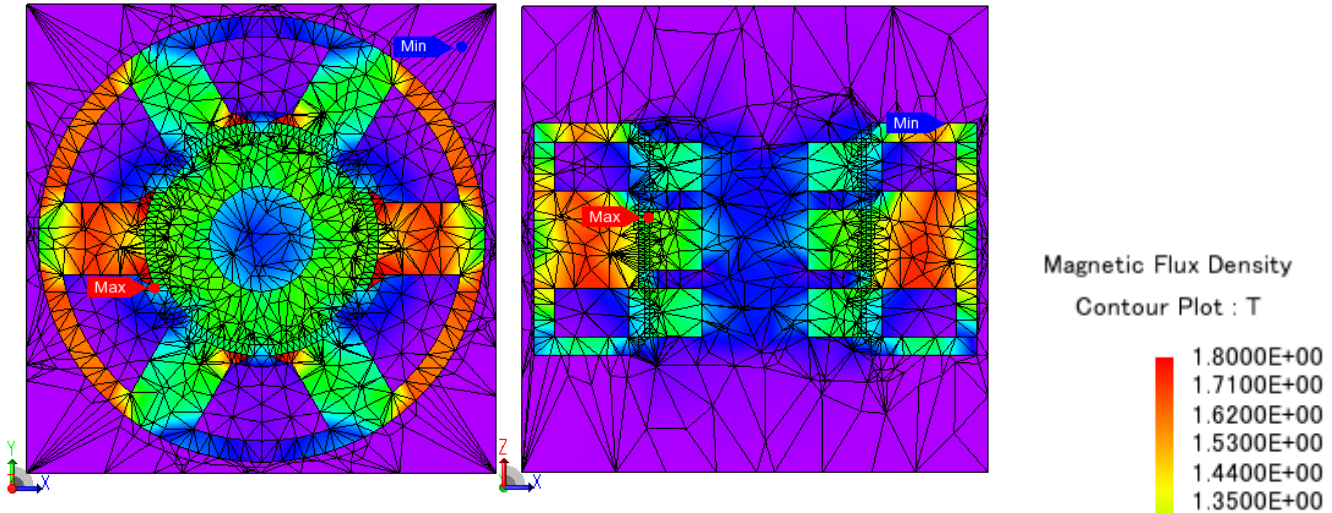

Figure 5.20 Flux density for $I_d = 25A$ on type B

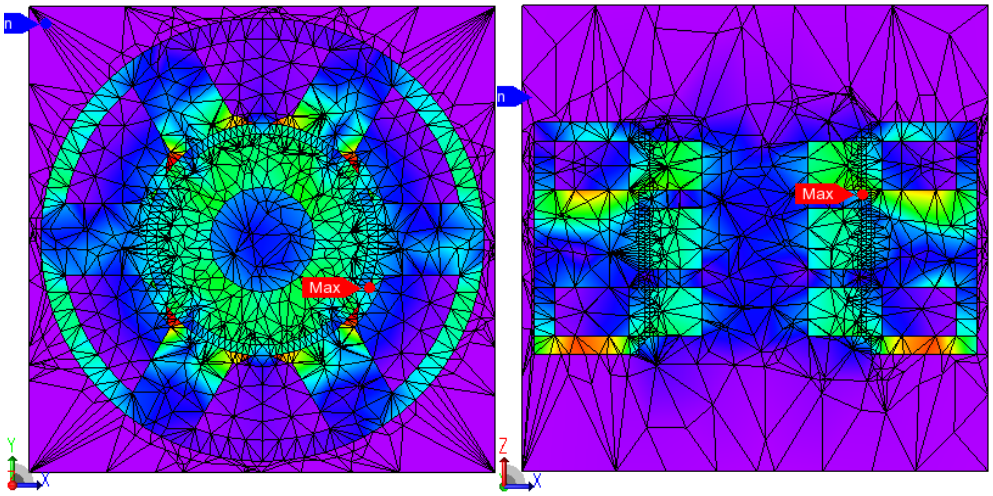

Figure 5.21 Flux density for $I_d = -25A$ on type B

5.4.6. Critical frequencies

This section shows calculations of critical speeds for the passively stabilized axes. There is a direct relation between stiffness and critical speed. Critical speed value varies with the squared root of the respective stiffness. The critical mechanical speed for radial oscillations, ω_r, is given by:

$$\omega_r = \frac{60}{2\pi}\sqrt{\frac{|K_r|}{m}},$$

where K_r is the resultant radial stiffness and m is the rotor mass. Being ω_r in rpm, K_r in N/m and m in kg.

Table 5.4 shows the relation between the radial stiffness and critical speeds. Operation near critical speeds are not desirable, since they are the speed values in which maximum oscillations occur. The minimum critical speed reached in this work was 6242rpm and the maximum value was 9200rpm. The specified speed, 18000rpm, is twice the highest critical speed, so probably critical oscillations will not present a problem during the experimental phase.

Table 5.4 Relation between radial stabilization and critical speeds

	Type A		
	Radial Stiffness	Centering Index	Critical Speed
Bearing I	-10.38N/mm	33.08	7693rpm
Bearing II	-14.85 N/mm	47.31	9200rpm
	Type B		
	Radial Stiffness	Centering Index	Critical Speed
Bearing I	-6.84 N/mm	21.78	6242rpm
Bearing II	-11.30 N/mm	36.01	8027rpm

There is also a critical speed value for tilting oscillations. The tilting critical mechanical frequency ω_θ in rpm is given by:

$$\omega_\theta = \frac{60}{2\pi}\sqrt{\frac{|K_\theta|}{J}},$$

where K_θ is the tilting stiffness in Nm/rad and J is the rotor inertia in kg m².

Inertia calculated by the 3D modeling software was around 900g mm², equal to $9\text{x}10^{-7}$kg m². Table 5.5 shows tilting stiffness and their respective critical speeds.

Table 5.5 Relation between tilting stabilization and critical speeds

	Type A	
	Tilting Stiffness	Critical Speed
Bearing I	-0.58Nm/rad	7657rpm
Bearing II	-0.37 Nm/rad	6095rpm
	Type B	
	Tilting Stiffness	Critical Speed
Bearing I	-0.56 Nm/rad	7504rpm
Bearing II	-0.34 Nm/rad	5902rpm

Critical speeds for tilting oscillations are smaller than 8000rpm. Probably this will not present a problem at the rated 18000rpm speed, because oscillations are damped in frequencies distant to the critical values.

There is not much difference in current requirement when employing Bearing I and Bearing II. Also critical speeds do not present a problem for both bearings. Bearing II is chosen for the final version of the motor, due to higher radial stability.

5.5. Summary of design modifications

Different design proposals were modeled in 3D and exported to a Finite-Element Analysis software. This session summarizes the main changes in design from the base model to the last version.

5.5.1. Number of stator teeth

Number of stator teeth was changed from 12 to 6.

5.5.2. Rotor shape

The number of rotor poles was changed from 8 to 4. Two rotor shapes were proposed as possible solutions. One that keeps the original segmented shape and another one that is composed of ring-shaped permanent magnets. The width of the permanent magnet rings was adjusted to increase average torque.

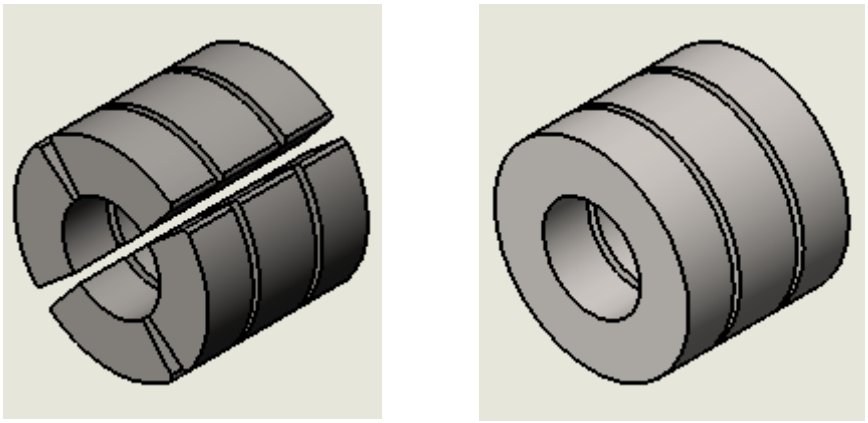

Figure 5.22 Proposed rotor types

5.5.3. Stator shape

Shoes were added to the stator teeth. They give mechanical support to the stator coils and enhance the flux linkage by capturing more flux lines from the rotor field, increasing the torque value without changing the machine size at the expense of adding to unstable radial forces.

The stator teeth were changed from an angular shape to a straight shape, increasing the area available for coil accommodation and making the flux density distribution more uniform along the teeth.

Yoke and teeth width were dimensioned according to flux density distribution, to avoid saturation while keeping considerable space for the stator coils.

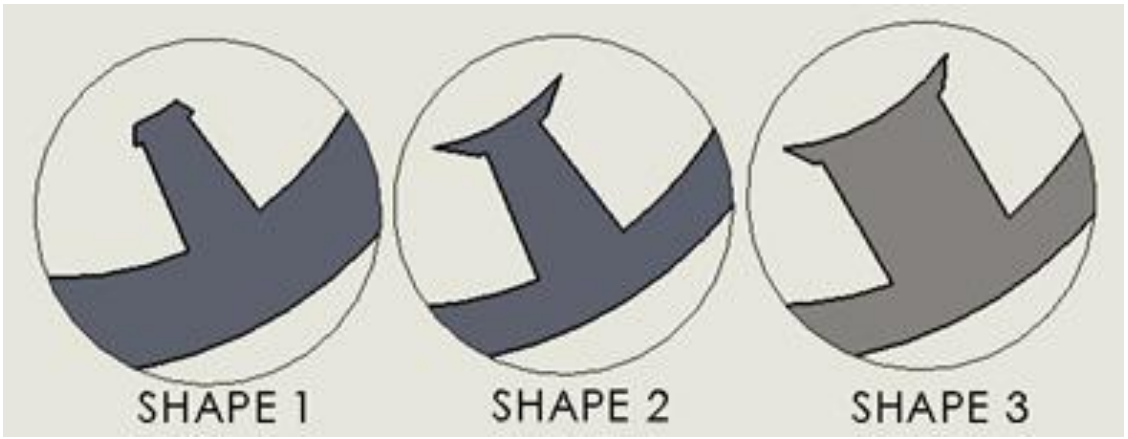

Figure 5.23 Comparison between the different stator pole shapes attempted

5.5.4. Number of turns per coil and rated current

The number of turns was decided in accordance to the slot area and to the maximum value of 40% slot fill factor. In the final design, 25 turns per coil are used.

5.5.5. Current supplied

The RMS current capacity for the 0.4mm diameter copper cable is around 1A. This results in current density of 7.96A/mm², almost equal to 8A/mm². Higher current densities imply the need for cooling systems in order to preserve isolation integrity. To simplify the system, we choose 1A RMS currents for feeding the coils.

5.5.6. Permanent magnet height

Increasing the central rotor permanent magnet height resulted in improved torque, while also implying an axial force offset and worse saturation in the central stator core. The central rotor PM was set at 2.9mm height.

5.5.7. Fine tuning of radial stiffness, tilting stiffness and active compensation.

The proposed passive bearing models were adjusted to fit the needs of this project. Passive bearings that had a marginally stable behavior were discarded, height was restricted by mechanical limitations and in the end, only model II with height equal to 2.4mm was kept.

5.5.8. Proposed solutions

Two models were designed that achieve target specifications, with rotor type A and type B. *Table 5.6* relates parameters achieved in both proposed models.

Table 5.6 Parameter comparison between models type A and B

	Type A	**Type B**
Torque	2.44mNm	2.96mNm
Torque ripple	40.8%	36.8%
Stator axial length	11mm	11mm
Total stack length	17mm	17mm
Stator outer diameter	21mm	21mm
Torque density	0.41N/L	0.50N/L
Rated speed	18000rpm	18000rpm
Output power	4.59W	5.59W
Copper losses	0.76W	0.76W
Iron Losses	0.559W	0.697W
Efficiency	77.74%	79.36%
Rated Current	1A RMS	1A RMS
Current density	7.96A/mm²	7.96A/mm²
Slot fill factor XZ plane	39%	39%
Slot fill factor XY plane	38%	38%
Centering index	47.31	36.01

6.Conclusion and future work

A new miniaturized single-drive axially-controlled bearingless motor was developed. Through many steps of modelling, simulation, result analysis and parameter optimization, a model contained in the dimensions stated as design specifications was conceived. Two rotor types with different characteristics were proposed: type A with a segmented permanent magnet and type B, with ring-shaped permanent magnet. Bearing Model II was chosen among the proposals presented.

Both motor types A and B achieved results inside the target region. The model has 17mm stack length, with passive bearings, and outer stator diameter equal to 21mm. Current density was kept below 8A/mm², not requiring cooling systems for preserving conductor isolation.

Figure 6.1 adds the proposed models to the data provided by [11] . It shows a comparison between torque density and centering index between models of axially-controlled 1DOF bearingless motors and motors with magnetic bearings, including motors type A and type B presented in this work.

The model that uses rotor type B has higher average torque, but smaller centering index that the one that uses rotor type A. The most suitable model depends on the application requirements. If torque density is the priority, type B is the most suitable, if stability should be the highest possible, type A is the most suitable.

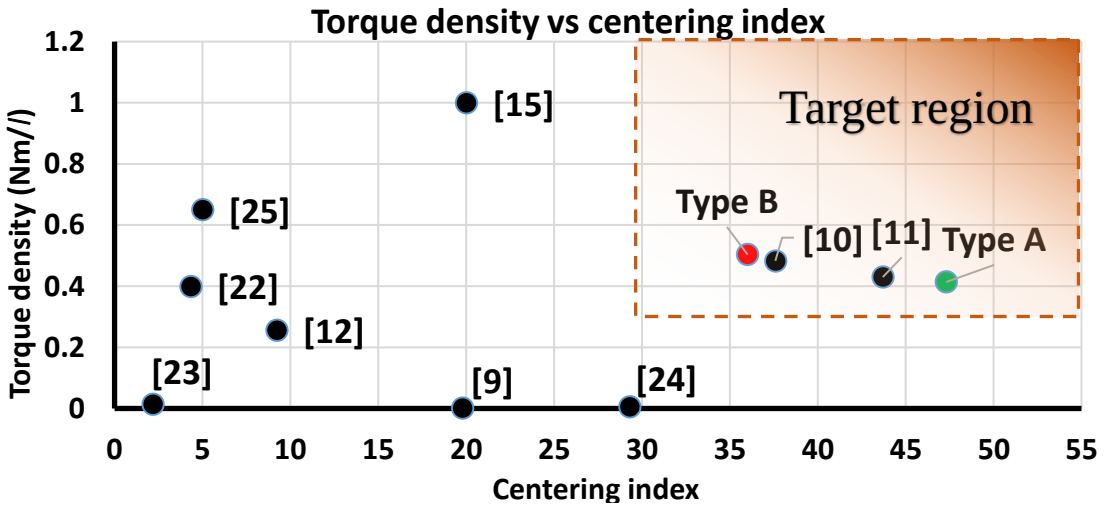

Figure 6.1 Torque density vs centering index for 1DOF axially controlled motors[11]

This motor still has room for improvement. Maximum currents for axial position control are too high. In the next version of the motor, a better relation between suspension currents and torque density will be sought.

Calculated critical speeds do not present a limiting factor for operation at 18000rpm. Even higher speeds may be achieved, being limited only by its back-EMF and mechanical losses due to air friction. The low calculated peak back-EMF (2.5V) indicates that it may be possible to drive the motor at higher speeds.

In this stage it is not possible to say if the radial stability is suitable or exaggerated. During the prototype phase, bearing models I and III will also be tested. If a satisfactory oscillation is achieved by reducing the radial stiffness, it will be possible to achieve higher torque densities, by reducing the height of the passive bearings and increasing the stator slot and number of turns per coil. In case the current radial stability is not enough, radial stiffness may be prioritized by increasing the height of the passive bearings and reducing the stator slot area or by employing bearing model III and increasing the stack length to 18mm, making the tilting stiffness more stable.

By comparing the results with the blood pump designed by OSA et al.[3], we see that it may be possible to modify and optimize this model for application on blood pumps. The lowest critical speed (8067rpm) is above the range of operating speeds of the reference (3000-5000rpm)[3] torque density was 0.41Nm/ℓ[4] and the motor has similar dimensions[3],[4].

The design process described in this document still does not include the mechanical design of the fan and mechanical structure. Current density was limited to 8A/mm² as a safety measure, but if a prototype is built with good heat dispersion, it may be possible to increase the current density up to 12A/mm² (1.5A RMS) and torque density to 0.76Nm/ℓ for type B and 0.63Nm/ℓ for type A, like shown in Figure 6.2.

The next step is designing the mechanical structure and assembling the first prototype. A PID controller will be implemented. Combinations of radial bearings and rotors will be analyzed.

In the future, different topologies may be studied, like one with outer rotor and a Halbach permanent magnet configuration.

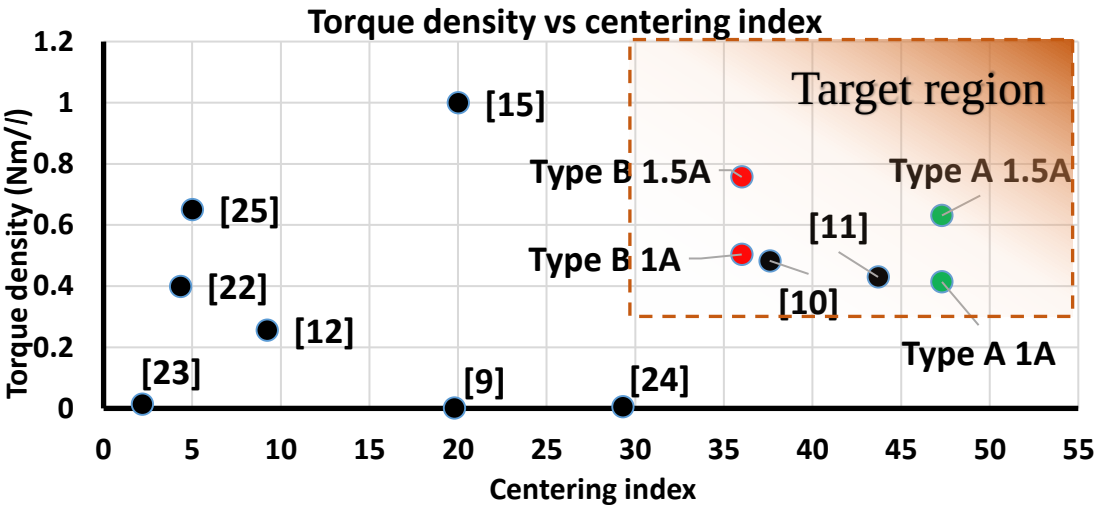

Figure 6.2 Torque density vs centering index for 1DOF axially controlled motors[11], possible enhancement

References

[1] A. Chiba et al., “Magnetic Bearings and Bearingless Drives,”. Elsevier, Newnes, MA, Burlington, 2005.

[2] S. Earnshaw, “On the nature of molecular forces which regulate the constitution of the luminiferous ether,” *Trans. Camb. Phil. Soc.*, vol. 7, pp. 97–112, 1842.

[3] M. Osa, T. Masuzawa, R. Orihara and E. Tatsumi, "Compact maglev motor with full DOF active control for miniaturized rotary blood pumps," *2017 11th International Symposium on Linear Drives for Industry Applications (LDIA)*, Osaka, Japan, 2017, pp. 1-6. doi: 10.23919/LDIA.2017.8097234

[4] M. Osa, T. Masuzawa, T. Saito, E. Tatsumi, “Magnetic levitation performance of miniaturized magnetically levitated motor with 5-DOF active control, Mechanical Engineering Journal,” in *JSME Mechanical Engineering Journal*, vol. 4, no. 5, Released October 15, 2017, [Advance publication] Released August 10, 2017, Online ISSN 2187-9745, Print ISSN , https://doi.org/10.1299/mej.17-00007

[5] N. Kurita, T. Ishikawa and H. Kamata, "Magnetically levitated motor with five actively controlled degrees of freedom," *2016 19th International Conference on Electrical Machines and Systems (ICEMS)*, Chiba, 2016, pp. 1-4.

[6] J. Asama, R. Natsume, H. Fukuhara, T. Oiwa and A. Chiba, "Optimal Suspension Winding Configuration in a Homo-Polar Bearingless Motor," in *IEEE Transactions on Magnetics*, vol. 48, no. 11, pp. 2973-2976, Nov. 2012.

[7] M. Ooshima and C. Takeuchi, "Magnetic Suspension Performance of a Bearingless Brushless DC Motor for Small Liquid Pumps," in *IEEE Transactions on Industry Applications*, vol. 47, no. 1, pp. 72-78, Jan.-Feb. 2011.

[8] M. Schuck, A. Da Silva Fernandes, D. Steinert and J. W. Kolar, "A high speed millimeter-scale slotless bearingless slice motor," *2017 IEEE International Electric Machines and Drives Conference (IEMDC)*, Miami, FL, 2017, pp. 1-7.

[9] J. Kuroki, T. Shinshi, L. Li, and A. Shimokohbe, “Miniaturization of a one-axis-controlled magnetic bearing,” Precis. Eng., vol. 29, no. 2, pp. 208–218, Apr. 2005.

[10] H. Sugimoto, I. Shimura and A. Chiba, "Design of SPM and IPM rotors in novel one-axis actively positioned single-drive bearingless motor," *2014 IEEE Energy Conversion Congress and Exposition (ECCE)*, Pittsburgh, PA, 2014, pp. 5858-5863.

[11] H. Sugimoto, I. Shimura and A. Chiba, "A Novel Stator Structure for Active Axial Force Improvement in a One-Axis Actively Positioned Single-Drive Bearingless Motor," in *IEEE Transactions on Industry Applications*, vol. PP, no. 99, pp. 1-1.

[12] W. Bauer, P. Freudenthaler, and W. Amrhein, “Experimental Characterization of a Bearingless Rotating Field Axial-Force/Torque Motor,” in Proc. 14th International Symposium on Magnetic Bearings (ISMB14), Linz, Austria, pp. 132-137, 2014.

[13] J. Asama, K. Takahashi, T. Oiwa and A. Chiba, "Reduction in torque and suspension force ripples of an axial-gap single-drive bearingless motor," *2016 IEEE Energy Conversion Congress and Exposition (ECCE)*, Milwaukee, WI, 2016, pp. 1-7.

[14] H. Sugimoto, I. Shimura and A. Chiba, "Experimental verification of energy-saving effect of a single-drive bearingless motor," *2016 19th International Conference on Electrical Machines and Systems (ICEMS)*, Chiba, 2016, pp. 1-6.

[15] H. Sugimoto, T. Srichiangsa and A. Chiba, "Design of a high-speed single-drive bearingless motor," *2017 IEEE International Electric Machines and Drives Conference (IEMDC)*, Miami, FL, 2017, pp. 1-6.

[16] T. Yamada *et al.*, "Outer Rotor Consequent-Pole Bearingless Motor With Improved Start-Up Characteristics," in *IEEE Transactions on Magnetics*, vol. 44, no. 11, pp. 4273-4276, Nov. 2008.

[17] M. Takemoto, "Basic characteristic of a two-unit outer rotor type bearingless motor with consequent pole permanent magnet structure," *2014 International Power Electronics Conference (IPEC-Hiroshima 2014 - ECCE ASIA)*, Hiroshima, 2014, pp. 1000-1005.

[18] T. Reichert, T. Nussbaumer, J. W. Kolar, "Bearingless 300-W PMSM for Bioreactor Mixing", *IEEE Tran. on Industrial Electronics*, vol. 59, no. 3, pp. 1376-1388, Mar. 2012.

[19] T. Reichert, T. Nussbaumer, J. W. Kolar, "Investigation of Exterior Rotor Bearingless Motor Topologies for High-Quality Mixing Applications", *IEEE Tran. on Industry Applications*, vol. 48, no. 6, pp. 2206-2216, Nov./Dec. 2012.

[20] T. Reichert, J. W. Kolar, T. Nussbaumer, "Stator Tooth Design Study for Bearingless Exterior Rotor PMSM", *IEEE Tran. on Industry Applications*, vol. 49, no. 4, pp. 1515-1522, July/Aug. 2013.

[21] W. Bauer and W. Amrhein, “Electrical Design Considerations for a Bearingless Axial-Force/Torque Motor,” *IEEE Trans. Ind. Appl.*, vol. 50, no. 4, pp. 2512–2522, July/August 2014.

[22] J. Asama, D. Watanabe, T. Oiwa, and A. Chiba, “Development of a One-Axis Actively Regulated Bearingless Motor with a Repulsive Type Passive Magnetic Bearing,” in Proc. International Power Electronics Conference (IPEC-Hiroshima2014-ECCE-ASIA), pp. 988-993, 2014.

[23] J. Asama, Y. Hamasaki, T. Oiwa, and A. Chiba, “Proposal and Analysis of a Single-Drive Bearingless Motor,” *IEEE Trans. Industrial Electronics*, vol. 60, no. 1, pp. 129-138, Jan. 2013.

[24] H. Sugimoto, S. Tanaka, A. Chiba, and J. Asama, “Principle of a Novel Single-Drive Bearingless Motor with Cylindrical Radial Gap,” *IEEE Trans. Ind. Appl.*, vol. 51, no. 5, pp. 3696-3709 , Sep./Oct., 2015.

[25] W. Bauer and W. Amrhein, “Electrical Design Considerations for a Bearingless Axial-Force/Torque Motor,” *IEEE Trans. Ind. Appl.*, vol. 50, no. 4, pp. 2512–2522, July/August 2014.

[26] H. Hoshi, T. Shinshi, and S. Takatani, “Third-generation Blood Pumps With Mechanical Noncontact Magnetic Bearings,” Artificial Organs, vol. 30, no. 5, pp. 324-338, 2006.

[27] C. Zwyssig, J. Kolar, and S. Round, “Megaspeed drive systems: Pushing beyond 1 million r/min,” IEEE/ASME Trans. Mechatronics, vol. 14, no. 5, pp. 564–574, 2009.